VNIVERSITAT DE VALÈNCIA

TESIS DOCTORAL

Tomography of the SN 1987A ejecta and AGN core-shifts with high-precision astrometry

Francisco Jesús Abellán de Paco

Octubre 2017

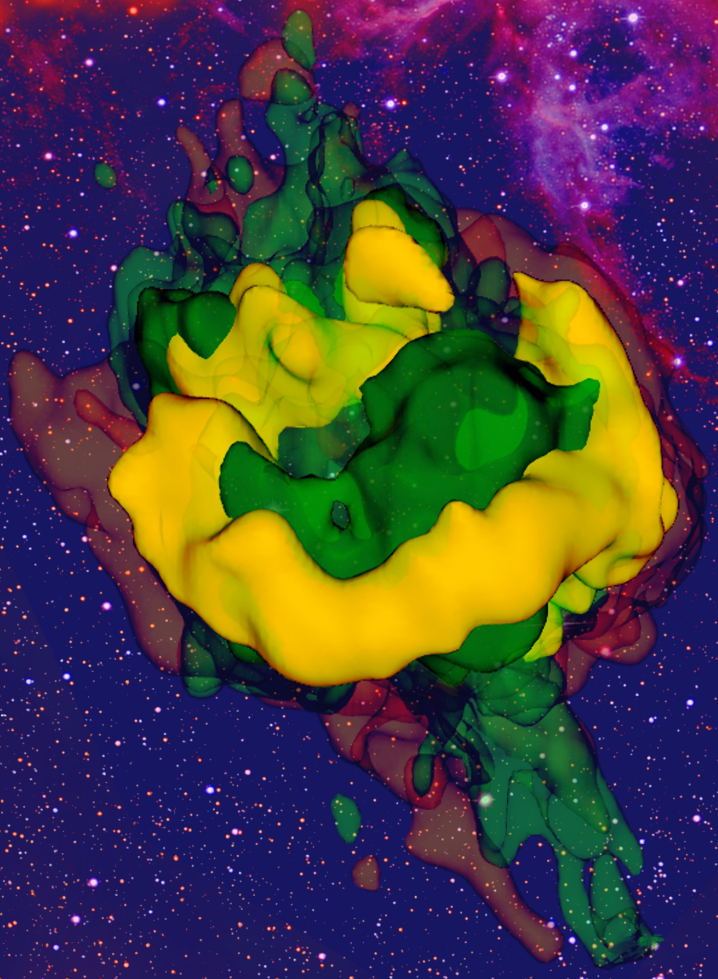

Departament d'Astronomia i Astrofísica

VNIVERSITAT DE VALÈNCIA

Tomography of the SN 1987A ejecta and AGN core-shifts with high-precision astrometry

Memoria presentada para optar al título de Doctor en Física

Francisco Jesús Abellán de Paco

Dirigida por el Doctor

Juan María Marcaide Osoro

y co-dirigida por el Doctor

Iván Martí Vidal

Departamento de Astronomía y Astrofísica
Universidad de Valencia

Valencia, Octubre 2017

JUAN MARÍA MARCAIDE OSORO, Catedrático de Astronomía y Astrofísica de la Universidad de Valencia, e IVÁN MARTÍ VIDAL, Astrónomo de plantilla y miembro del European ALMA Regional Center, Onsala Space Observatory, Chalmers University of Technology de Suecia

CERTIFICAN:

Que la presente memoria, titulada **Tomography of the SN 1987A ejecta and AGN core-shifts with high-precision astrometry**, ha sido realizada en el Departamento de Astronomía y Astrofísica de la Universidad de Valencia por Francisco Jesús Abellán de Paco bajo su dirección, y constituye su Tesis Doctoral para optar al grado de Doctor en Ciencias Fısicas.

Valencia, 24 de octubre de 2017

Fdo. Juan María Marcaide Osoro

Fdo. Iván Martí Vidal

A mi familia

Agradecimientos

De gente bien nacida es agradecer los beneficios que recibe.

Don Quijote de la Mancha
Miguel de Cervantes

En efecto, tal y como predicaba el ingenioso hidalgo Don Quijote de la Mancha, uno debería de agradecer por todo aquello que recibe. Y ese es precisamente el propósito que persigo en las siguientes líneas. Más de cuatro años han pasado desde que me mudase a Valencia y empezase la aventura de la Tesis Doctoral. Y ahora que concluye, es mucha la gente a la que debo estar agradecido.

En primer lugar, me gustaría dar las gracias al director de esta tesis, Jon Marcaide, por darme la oportunidad de trabajar en el grupo de investigación que él mismo impulsase a crear hace ya más de 20 años. Desde el momento en que empecé a trabajar con Jon supe que sería su último estudiante de doctorado. Y conociendo la brillantez científica de los estudiantes que ha formado a lo largo de su carrera, he de admitir que me siento orgulloso de formar parte de esa lista. Gracias a ello he podido trabajar haciendo ciencia de primer nivel, como la que se pueda hacer en los mejores centros de investigación del mundo. Y aunque el camino no ha sido fácil, debo agradecer a Jon su confianza ciega en que todo el esfuerzo valdría la pena. Sus críticas, sugerencias, y consejos, todos ellos desde el punto de vista de la experiencia, han ayudado a que esta tesis haya llegado finalmente a buen puerto.

Gracias también a Iván Martí Vidal, co-director de esta tesis, por su inestimable ayuda en la consecución de la misma. Son muchísimas las cosas que he aprendido de él a lo largo de estos cuatro años, y no solo en el campo meramente científico. Juntos hemos "sufrido" las innumerables *trampas* que esconde la astrometría diferencial. Pero después de más de tres años de trabajo en ese campo, de incontables e-mails, videoconferencias, y algún que otro altibajo, ¡lo conseguimos!

También me gustaría agradecer especialmente a Remy Indebetouw. Sin su ayuda y colaboración, esta tesis sencillamente no se habría podido realizar. Entre otras cosas, por haberme dado la oportunidad de trabajar con unas excelentes observaciones de la supernova SN 1987A en el marco de un proyecto fascinante. Mis estancias de investigación con Remy en uno de esos centros de investigación "top" a nivel mundial, el National Radio Astronomy Observatory (NRAO) de Virginia (USA), me han enriquecido muchísimo tanto a nivel personal como científico.

Por supuesto, cuatro años de doctorado dan para mucho, y hay unas cuantas personas a las que también me gustaría agradecer. A José Carlos Guirado, tanto por su ayuda con la astrometría, como por todos los consejos que me ha dado en este tiempo. A Markus Wittkowski, por contar conmigo en todo lo referente al proyecto de interferometría infrarroja que él mismo lidera y que tan interesante se prevee en el futuro. A todos los miembros del equipo internacional que estudia la supernova SN 1987A con ALMA. En particular, a Michael Gabler y su equipo, por compartir sus modelos hidrodinámicos; y a Claes Fransson, Richard McCray, y Jason Spyromilio por su inestimable ayuda en el análisis e interpretación de los resultados que presento en esta tesis. A Antxon Alberdi, por la amabilidad y afecto que siempre ha tenido para conmigo, y por ser el primero en enseñarme a calibrar datos con AIPS cuando apenas empezaba mi andadura en esto del doctorado. A Belén Arroyo, por toda la ayuda que me dio también en esos primeros días. Al Departamento de Astronomía y Astrofísica de la Universidad de Valencia, con especial mención a Feli y Manel, por su ayuda con todos los temas burocráticos.

También me gustaría agradecer a todas las instituciones que de una u otra manera han ayudado a la elaboración de esta tesis. En particular a todos aquellos centros en los que he podido realizar distintas estancias de investigación: Instituto de Astrofísica de Andalucía (Granada), Onsala Space Observatory (Suecia), University of Virginia/NRAO (USA), y European Southern Observatory (Alemania). Gracias también al Ministerio de Economía y Competitividad por su ayuda económica con la beca de Formación de Personal Investigador (FPI).

Y para concluir, dedico mis últimas líneas a las personas más especiales en mi vida. A mis amigos, los que me han animado a seguir adelante y que sé que siempre estarán ahí. A Miriam, por su cariño, por su paciencia, y por su confianza plena en mí que muchas veces me ha servido como “chute” de motivación para acabar esta tesis. Por último, gracias infinitas a mi familia. Todo lo que soy se lo debo a ellos. Gracias a mis abuelos maternos por todo el amor que me dieron, y que tristemente he perdido en el último año. Gracias a mi hermana, de la que siendo solo un niño pude aprender el verdadero significado de “luchar por algo”. Esa lección la recordaré para siempre. Y por supuesto, gracias a mis padres, por su sacrificio, por su lucha día a día, y por todos los valores que me han enseñado y transmitido a lo largo de toda mi vida. El mayor regalo que me han podido hacer.

List of publications

This thesis is based on the work presented in the following publications:

I. *Core-shifts and proper-motion constraints in the S5 polar cap sample at the 15 and 43 GHz bands*
F. J. Abellán, I. Martí-Vidal, J. M. Marcaide, J. C. Guirado.
Submitted to Astronomy & Astrophysics.

II. *Very Deep inside the SN 1987A Core Ejecta: Molecular Structures Seen in 3D*
F. J. Abellán, R. Indebetouw, J. M. Marcaide, M. Gabler, C. Fransson, J. Spyromilio, D. N. Burrows, R. Chevalier, P. Cigan, B. M. Gaensler, H. L. Gomez, H.-Th. Janka, R. Kirshner, J. Larsson, P. Lundqvist, M. Matsuura, R. McCray, C.-Y. Ng, S. Park, P. Roche, L. Staveley-Smith, J. Th. van Loon, J. C. Wheeler, S. E. Woosley.
The Astrophysical Journal Letters, 842, L24 (2017).

III. *Absolute kinematics of radio-source components in the complete S5 polar cap sample - IV. Proper motions of the radio cores over a decade and spectral properties*
I. Martí-Vidal, **F. J. Abellán**, J. M. Marcaide, J. C. Guirado, M. A. Pérez-Torres, E. Ros.
Astronomy & Astrophysics, 596, A27 (2016).

The work carried out during this thesis also contributed to the following refereed publications, not discussed in this manuscript:

IV. *Multi-epoch VLTI-PIONIER imaging of the supergiant V766 Cen. Direct detection of the close companion in front of the primary*
M. Wittkowski, **F. J. Abellán**, B. Arroyo-Torres, A. Chiavassa, J. C. Guirado, J. M. Marcaide, A. Alberdi, W. J. de Wit, K.-H. Hofmann, A. Meilland, F. Millour, S. Mohamed, J. Sanchez-Bermudez.
Astronomy & Astrophysics, 606, L1 (2017).

V. *ALMA spectral survey of Supernova 1987A - molecular inventory, chemistry, dynamics and explosive nucleosynthesis*
M. Matsuura, R. Indebetouw, S. Woosley, V. Bujarrabal, **F. J. Abellán**, R. McCray, J. Kamenetzky, C. Fransson, M. J. Barlow, H. L. Gomez, P. Cigan, I. De Looze, J. Spyromilio, L. Staveley-Smith, G. Zanardo, P. Roche, J. Larsson, S. Viti, J. Th. van Loon, J. C. Wheeler, M. Baes, R. Chevalier, P. Lundqvist, J. M. Marcaide, E. Dwek, M. Meixner, C.-Y. Ng, G. Sonneborn, J. Yates.
Monthly Notices of the Royal Astronomical Society, 469, 3347 (2017).

VI. *VLTI/AMBER spectro-interferometry of the late-type supergiants V766 Cen (=HR 5171 A), σ Oph, BM Sco, and HD 206859*
M. Wittkowski, B. Arroyo-Torres, J. M. Marcaide, **F. J. Abellán**, A. Chiavassa, J. C. Guirado.
Astronomy & Astrophysics, 597, A9 (2017).

VII. *What causes the large extensions of red supergiant atmospheres? Comparisons of interferometric observations with 1D hydrostatic, 3D convection, and 1D pulsating model atmospheres*
B. Arroyo-Torres, M. Wittkowski, A. Chiavassa, M. Scholz, B. Freytag, J. M. Marcaide, P. H. Hauschildt, P. R. Wood, **F. J. Abellán**.
Astronomy & Astrophysics, 575, A50 (2015).

List of acronyms

AAO	Australian Astronomical Observatory
AAVSO	American Association of Variable Star Observers
ACA	Atacama Compact Array
AGN	Active Galactic Nuclei
AIPS	Astronomical Image Processing System
ALMA	The Atacama Large Millimeter/submillimeter Array
BLR	Broad line region
BSG	Blue supergiant
CASA	Common Astronomy Software Application
CCO	Constant clock offset
CCSNe	Core-collapse supernovae
CO	Carbon monoxide
ER	Equatorial ring
ESA	European Space Agency
ESO	European Southern Observatory
FFS	Fast frequency switching
FFT	Fast Fourier Transform
FIR	Far-infrared
FWHM	Full width at half maximum
FWZI	Full width at zero intensity
GBT	Green Bank Telescope
GFF	Global Fringe Fitting
GHz	Gigahertz
GMVA	Global mm-VLBI Array
HST	Hubble Space Telescope
IAU	International Astronomical Union
ICRF	International Celestial Reference Frame
IF	Intermediate frequency

IFDPD	Inter-frequency differential phase-delay
ISM	Interstellar medium
KVN	Korean VLBI Network
LCP	Left circular-hand polarization
LMC	Large Magellanic Cloud
LTE	Local Thermodynamic Equilibrium
MAS	Milliarcsecond
MEM	Maximum Entropy Method
MHz	Megahertz
NASA	National Aeronautics and Space Agency
NIR	Near-infrared
NLR	Narrow line region
NRAO	National Radio Astronomy Observatory
NS	Neutron star
PSF	Point spread function
QSO	Quasi-stellar object
RMS	Root Mean Square
RSG	Red supergiant
S/N	Signal-to-noise ratio
SASI	Standing accretion shock instability
SFPR	Source-frequency phase referencing
SINFONI	Spectrograph for INtegral Field Observations in the Near Infrared
SiO	Silicon monoxide
SMBH	Supermassive black hole
SN	Supernova
SNe	Supernovae
SNR	Supernova remnant
SSA	Synchrotron self-absorption
SSO	Siding Spring Observatory
TECU	Total Electron Content Unit
UT	Universal Time
UV	Ultraviolet
UVPAP	University-of-Valencia Precision Astrometry Package
VERA	VLBI Exploration of Radio Astrometry
VLA	The Very Large Array
VLBA	The Very Long Baseline Array
VLBI	Very Long Baseline Interferometry
VLT	Very Large Telescope

Resumen

Esta tesis trata dos temas muy distintos: (1) el estudio de las estructuras y movimientos propios de los chorros de los núcleos activos de galaxias (AGN) que componen la muestra S5 del casquete polar, por medio de astrometría global de alta precisión con la técnica de interferometría de muy larga base (VLBI); y (2) la reconstrucción tomográfica (i.e., 3D) de la emisión molecular de la parte interna de la supernova SN 1987A y su comparación con modelos de explosión de supernovas.

En la primera parte, presentamos el análisis astrométrico diferencial llevado a cabo para todas las fuentes de la muestra S5 del casquete polar. Se consigue aplicar por primera vez a 43 GHz la técnica de astrometría de alta precisión con VLBI, haciendo uso del observable *retraso de fase*. Estos resultados astrométricos se comparan con los obtenidos a 15 GHz durante la misma época de observación (año 2010), y también a los obtenidos a 15 GHz en una época anterior (año 2000). Las diferencias en las separaciones entre fuentes de los pares de fuentes observados en común en las dos épocas son compatibles a nivel de 1σ entre las bandas U (15 GHz) y Q (43 GHz).

El intervalo de tiempo entre las distintas observaciones nos permite estudiar los movimientos propios de los núcleos (*"cores"*) de las fuentes con precisiones de unos pocos microsegundos de arco por año (μas yr^{-1}). Estudiamos la estabilidad de la posición de las fuentes analizando los cambios en las posiciones relativas de los *cores* de los chorros a lo largo de una década. Encontramos desplazamientos del orden de $0.1-0.9$ milisegundos de arco en fuentes cercanas entre sí entre las dos épocas, lo que se traduce en unos movimientos propios asociados a los *cores* de aproximadamente unas decenas de μas yr^{-1}. Estos resultados tienen implicaciones en el modelo estandar de chorros de AGN (según el cual las posiciones de los *cores* son constantes en el tiempo).

Gracias a un análisis quasi-simultáneo de las observaciones de 2010 en banda U y Q, hacemos mapas de índice espectral y estudiamos los efectos cromáticos (i.e., *core-shift*) que se producen en el núcleo de las radiofuentes utilizando tres métodos independientes. Las magnitudes de los *core-shifts* obtenidos con los tres métodos son del mismo orden.

Sin embargo, existen algunas discrepancias en las orientaciones de los *core-shifts* determinadas con cada método. En algunos casos, estas discrepancias se deben a deficiencias del método. En otros casos, las discrepancias reflejan supuestos del método en sí y podrían ser atribuídas a curvaturas en los chorros y/o a que dichos chorros no sean cónicos.

En la segunda parte de la tesis, presentamos los resultados de la tomografía de SN 1987A con líneas de monóxido de carbono (CO) y monóxido de silicio (SiO) para determinar la morfología de la emisión molecular en las zonas más internas del remanente de la supernova. Las estrellas más masivas finalizan su vida en explosiones de supernova que se producen cuando su núcleo colapsa gravitatoriamente, enriqueciendo el medio interestelar con nuevos elementos sintetizados durante la explosión. Después del colapso del núcleo, se producen inestabilidades en la explosión a medida que el choque se propaga hacia afuera a través de la estrella progenitora. Observaciones de la composición y la estructura de las regiones más internas de este tipo de supernovas por medio de su emisión radiativa proporcionan una prueba directa de las inestabilidades y de los nuevos productos sintetizados en la explosión.

SN 1987A, en la Gran Nube de Magallanes, es la única supernova en la cual la parte interna puede ser resuelta antes de verse afectada por la interacción con el medio circundante. Nuestras observaciones de SN 1987A con el Atacama Large Millimeter/submillimeter Array (ALMA) son las de mayor resolución hasta la fecha y revelan en detalle la morfología de la emisión del gas molecular frío en las regiones más internas del remanente.

Las distribuciones 3D de la emisión de CO y de SiO son distintas, pero en ambos casos se encuentra un déficit de emisión en la parte central con una forma de emisión que recuerda a una distribución de tipo toroidal. Esta distribución puede ser debida al calentamiento radiactivo que se produjo en las primeras semanas tras la explosión (“nickel heating”). Asimismo, se encuentra que la distribución de la emisión de ambas moléculas presenta un aspecto “grumoso”. Las escalas de tamaño de dicha distribución se comparan cuantitativamente con los más sofisticados modelos hidrodinámicos, estableciendo de esta manera límites en la física relacionada con la explosión de la supernova y con la estrella progenitora.

Abstract

This thesis has two very different parts: (1) the study of structures and proper motions in the AGN radio jets of the S5 polar cap sample, by means of VLBI high-precision multi-frequency phase-delay astrometry; and (2) the tomography (i.e., 3D) reconstruction of the molecular emission and kinematics in the inner ejecta of supernova SN 1987A.

In the first part, we report on a differential astrometry analysis for all sources in the S5 polar cap sample. The technique of VLBI high-precision phase-delay astrometry is successfully applied, for the first time, at the frequency of 43 GHz. These astrometric results are compared to those obtained at 15 GHz during the same epoch of observations (year 2010), and also to 15 GHz data collected in a previous epoch (year 2000). The differences in source separations among all the source pairs observed in common at the two epochs are compatible at the 1σ level between U and Q bands.

The time interval between observations enables us to achieve precisions in the proper motions of the source cores of a few $\mu\mathrm{as\,yr}^{-1}$. We study the source-position stability by analyzing the changes in the relative positions of fiducial source points (the jet cores) over a decade. We find motions of $0.1-0.9$ mas among close-by sources between the two epochs, which imply drifts in the jet cores of approximately a few tens of $\mu\mathrm{as\,yr}^{-1}$. These results have implications for the standard AGN jet model (where the core locations are supposed to be stable in time).

With the benefit of quasi-simultaneous U/Q band observations in 2010, we make spectral-index maps and study chromatic effects (i.e., *core-shift*) at the radio source cores using three independent methods. The magnitudes of the core-shifts are of the same order for all methods. However, some discrepancies arise among the methods in the determination of the core-shift orientations. In some cases, these discrepancies are due to insufficient information for the corresponding method to be successfully applied. In others, the discrepancies reflect assumptions of the methods and could be explained by curvatures in the jets and/or departures from conical jets.

In the second part of the thesis, we present the result of a tomography of SN 1987A aimed to determine the morphology of the molecular emission in the innermost regions of remnant. Most massive stars end their lives in core-collapse supernova explosions and enrich the interstellar medium with explosively nucleosynthesized elements. Following core collapse, the explosion is subject to instabilities as the shock propagates outwards through the progenitor star. Observations of the composition and structure of the innermost regions of a core-collapse supernova provide a direct probe of the instabilities and nucleosynthetic products.

SN 1987A in the Large Magellanic Cloud (LMC) is the only supernova for which the inner ejecta can be spatially resolved before it is strongly affected by interaction with the surroundings. Our observations of SN 1987A with the Atacama Large Millimeter/submillimeter Array (ALMA) are of the highest resolution to date and reveal the detailed morphology of the emission of cold molecular gas in the innermost regions of the remnant. The 3D distributions of carbon and silicon monoxide (CO and SiO) emission differ, but both have a central deficit, or torus-like distribution, possibly a result of radioactive heating during the first weeks ("nickel heating"). The size scales of the clumpy distribution are compared quantitatively to models, demonstrating how progenitor and explosion physics can be constrained.

Contents

List of Figures

List of Tables

Chapter 1

Introduction

From the moment I picked up your book
until I laid it down, I was convulsed with
laughter. Some day I intend reading it.

Groucho Marx

1.1 Thesis motivation

This thesis covers two very different topics, both of them making use of radio interferometry as the observational technique. The first part of the thesis is focused on a high-precision astrometric analysis of the sources of the complete S5 polar cap sample. The second part of the thesis is devoted to the study of the 3D distribution of the molecular emission in the SN 1987A ejecta.

The aim of the first part is to perform a global high-precision astrometric analysis of a complete radio sample, where the term *global* should be understood as many sources spread across a big patch of the sky. In order to achieve this goal, we make use of the observable *phase delay*, which is more precise than the observable used in many geodetic and astrometric observations, the *group delay*, by up to two orders of magnitude. The target of the astrometric analysis is the complete S5 polar cap sample, which consists of 13 radio sources (quasars and BL-Lac objects) from the S5 survey (Kühr et al., 1981). All sources studied are spread around the celestial northern polar cap and have AGN jets with flat spectra and high flux densities.

The work presented in this part of the thesis belongs to a large VLBI astrometry campaign, in which the S5 polar cap sample was observed over the last two decades in phase-referencing mode. The main goals of this campaign were the study of the frequency dependence and time stability of the positions of the cores

of the jet structures, as well as the characterization of the absolute kinematics of the optically-thin jet components of all sources of the sample. This kind of analysis enables us to compare our results with the predictions of the standard jet model.

Furthermore, the objective of this thesis is also to perform global differenced phase-delay astrometry at 43 GHz, the highest frequency ever attempted in this kind of analysis. This is an ambitious goal because at this high frequency, the correct determination of the phase delay ambiguities is particularly difficult. However, this work needs to be done in order to determine the core-shifts of the sources by comparing to the source positions derived from the astrometric analysis performed at a lower frequency. The comparison of our astrometric results with those obtained previously at 15 GHz (Martí-Vidal et al., 2008), enables us to study the proper motions and the change in the angular separation between pairs of sources over a decade.

The goal of the second part of the thesis is to determine the morphology of the molecular emission in the innermost regions of SN 1987A. It is known that most massive stars, such as the progenitor of SN 1987A, end their lives in core-collapse supernova explosions and enrich the interstellar medium with explosively nucleosynthesized elements. Following core collapse, the explosion is subject to instabilities as the shock propagates outward through the progenitor star. Hydrodynamic simulations of the explosion of SN 1987A (e.g., Hammer et al., 2010; Utrobin et al., 2015; Wongwathanarat et al., 2015) and analyses of its nebular spectrum (McCray, 1993) indicate that nucleosynthetic products retain their chemical identity but are mixed macroscopically by those instabilities during and shortly after the explosion. Thus, observations of the composition and structure of the innermost regions of a core-collapse supernova provide a direct probe of the instabilities and nucleosynthetic products.

SN 1987A in the Large Magellanic Cloud is the only known supernova for which the inner ejecta can be spatially resolved before it has interacted with the surroundings. Modest angular resolution (~ 500 mas) ALMA (Kamenetzky et al., 2013) data revealed the presence of bright rotational emission from cold (< 150 K) relatively slow moving (~ 2000 km s^{-1}) carbon monoxide CO and silicon monoxide SiO.

In this thesis, we make use of the extraordinary capabilities of ALMA to create unique 3D maps of CO and SiO molecular emission from the inner ejecta of SN 1987A *via Doppler tomography*. These observations are of the highest resolution ever achieved for SN 1987A and enable us to create and compare the first 3D maps of molecular emission from deep inside of the remnant with the predictions of state-of-the-art explosion models.

Finally, along the doctoral work there was also a third objective: a detailed study of a sample of red supergiant stars (RSGs) via infrared interferometry. This project was mostly aimed at characterizing fundamental parameters and atmospheric extensions of RSGs, to determine their location in the Hertzsprung-Russell (HR) diagram, and to study the structure and morphology of the close circumstellar environment and wind regions, including the atmospheric molecular layers and dusty envelopes. However, even though there were (minor) contributions made to this project, they will not be discussed in this thesis.

1.2 Thesis outline

All the observations used in this thesis were taken at radio wavelengths and utilized some of the most sensitive radio interferometers available. For this reason, Chapter 2 is dedicated to introducing the fundamental concepts of radio interferometry. It explains the basic workings of an interferometer and introduces essential radio interferometric terminology including the "complex visibility" and its relation to the sky brightness distribution. The technique of aperture synthesis imaging, widely used in radio interferometry, along with the radio facilities used in this thesis are presented. The chapter ends by describing the main concepts and characteristics of the astrometry performed with the VLBI technique.

Chapter 3 gives a description of Active Galactic Nuclei (AGN), the objects studied with high-precision astrometry in this thesis. It summarizes the properties and structure of AGN, in particular those of the structure and radio emission of the relativistic jets that emerge from the AGN cores. The most important absorption mechanism that takes place in the jets, synchrotron self-absorption, is described. The core-shift effect, as well as its importance and the most common methods used to determine it, is also presented.

Chapter 4 is based on articles already published or submitted, where we present the results of the global high-precision differential astrometry performed at 14.4 and 43.1 GHz.

Chapter 5 introduces supernova SN 1987A. The light curve and the evolution of the supernova remnant is described. The most important emission zones, as well as the emission of dust and molecules from the innermost regions of the remnant are presented. The chapter also reviews some state-of-the-art hydrodynamical models tailored to represent the observations of supernova explosions and supernova remnants.

Chapter 6 is based on the article published in The Astrophysical Journal Letters, 842, L24 (2017). The results obtained from a tomography of SN 1987A are presented.

Chapter 7 summarizes the main research conclusions and highlights future work which could complement and build on the findings presented in this thesis.

Chapter 2

Radio interferometry

The saddest aspect of life right now is that
science gathers knowledge faster than
society gathers wisdom.

Isaac Asimov

This thesis is focused on the study of the radio emission from AGN and supernova explosions making use of interferometry as the observational technique. In this chapter, we make a brief introduction of the main aspects of radio interferometry, such as the two-element interferometer, the complex visibility, and the basics of synthesis imaging. Then, we detail the radio facilities used in this thesis. Finally, we end the chapter by describing the main concepts and properties of VLBI astrometry.

For a more detailed description of the radio interferometry technique, we refer the reader to one of the following textbooks: Thompson, Moran & Swenson (2001), Burke & Graham-Smith (2009), Wilson, Rohlfs & Hüttemeister (2009), and references therein.

2.1 The diffraction limit

The angular resolution, $\Delta\theta$, of a radio antenna is the minimum angular separation which two point sources can have in order to be recognized as separate objects. The Rayleigh criterion is the operational defined angular resolution of a filled circular aperture of diameter, D, at the observational wavelength λ and is given as

$$\Delta\theta = 1.22\left(\frac{\lambda}{D}\right) \tag{2.1}$$

The Rayleigh criterion states that two objects are resolved when the first null of the diffraction pattern of one object coincides with the maximum of the diffraction pattern of the other. An immediate consequence of Equation 2.1 is that at long wavelengths, the angular resolution becomes low unless the diameter of the aperture can be increased substantially. In order to achieve modest angular resolution at radio wavelengths with a single radio antenna, the diameter becomes impractically large. Radio interferometry is the technique used in radio astronomy to overcome this problem of low angular resolution at long wavelengths.

2.2 The two-element interferometer

The basic interferometer is a pair of radio telescopes whose voltage outputs are correlated (multiplied and averaged). Even the most elaborate interferometers with $N >> 2$ elements can be treated as $N(N-1)/2$ independent two-element interferometers. Hence, studying the two-element interferometer allows us to understand multi-element interferometric arrays in a natural way. In this chapter, we discuss the main concepts and observables related to the two-element interferometer.

Figure 2.1 shows an example of a two-element interferometer, consisting of two identical dishes separated by a baseline vector, $\vec{b}$, of length b. Both dishes are pointing in the direction specified by the unit vector $\hat{s}$. Plane waves from a distant point source in this direction must travel an extra distance $\vec{b}\cdot\hat{s} = b\cos\theta$ to reach antenna 1, so the output of antenna 1 is the same as that of antenna 2, but it lags by the *geometric delay*

$$\tau_g = \frac{\vec{b}\cdot\hat{s}}{c} = \frac{b\cos\theta}{c} \tag{2.2}$$

where c is the speed of light. For simplicity, we first consider a quasi-monochromatic interferometer, one that responds only to radiation in a very narrow band centered

on frequency $\nu = \omega/2\pi$. Then, the output voltages of antennas 1 and 2 can be written as

$$V_1(t) = V_1^0 \cos[\omega(t - t_g)] \qquad \text{and} \qquad V_2(t) = V_2^0 \cos(\omega t) \tag{2.3}$$

where t is time. The voltages $V_1^0 = G_1 V$ and $V_2^0 = G_2 V$ registered at each antenna depend on the antenna gains G_1 and G_2, respectively. In the following we will consider $G_1 = G_2$. The correlator first multiplies these two voltages to yield the product

$$V_1(t)V_2(t) = \frac{V^2}{2}[\cos(2\omega t - \omega\tau_g) + \cos(\omega\tau_g)] \tag{2.4}$$

and then takes a time average long enough $\Delta t >> 1/2\omega$ to remove the high-frequency term $\cos(2\omega t - \omega\tau_g)$ from the final output R:

$$R = \langle V_1(t)V_2(t)\rangle = \frac{V^2}{2}\cos(\omega\tau_g) \equiv Re(t) \tag{2.5}$$

The amplitudes V_1 and V_2 are proportional to the electric field produced by the source multiplied by the the voltage gains of antennas 1 and 2. Thus the output amplitude $V^2/2$ is proportional to the point-source flux density S multiplied by $(A_1A_2)^{1/2}$, where A_1 and A_2 are the effective collecting areas of the two antennas. The effective collecting area of the antenna i, A_i, is obtained from the physical aperture of the antenna, A_i^{phys} ($= \pi r_i^2$), and the antenna gain, G_i, of the antenna i, by $A_i = G_i A_i^{phys}$. Uncorrelated noise from the receivers and the atmosphere over the two telescopes does not appear in the correlator output, so fluctuations in receiver gain or atmospheric emission are much less significant than for a total-power observation with a single dish.

If the antennas in an interferometric array are isotropic, then the point-source response of the interferometer would be a sinusoid spanning the entire sky, and the interferometer would be only sensitive to one Fourier component of the sky brightness distribution, having angular period $\lambda/\sin\theta$. The response of a two-element interferometer R with non-isotropic antennas is this sinusoid, multiplied by the product of the voltage patterns of the individual antennas. If the antennas are identical then this product is the power pattern of the individual antennas called the primary beam.

The primary beam is usually a Gaussian that is much wider than the fringe period, as $D << b\sin\theta$ (where D is the antenna diameter). The result is that an interferometer with directive antennas responds to a finite range of angular frequencies centered on $b\sin\theta/\lambda$. The instantaneous point source response of an interferometer is known as the synthesized beam and is the point source response obtained by averaging the outputs of all antenna pairs.

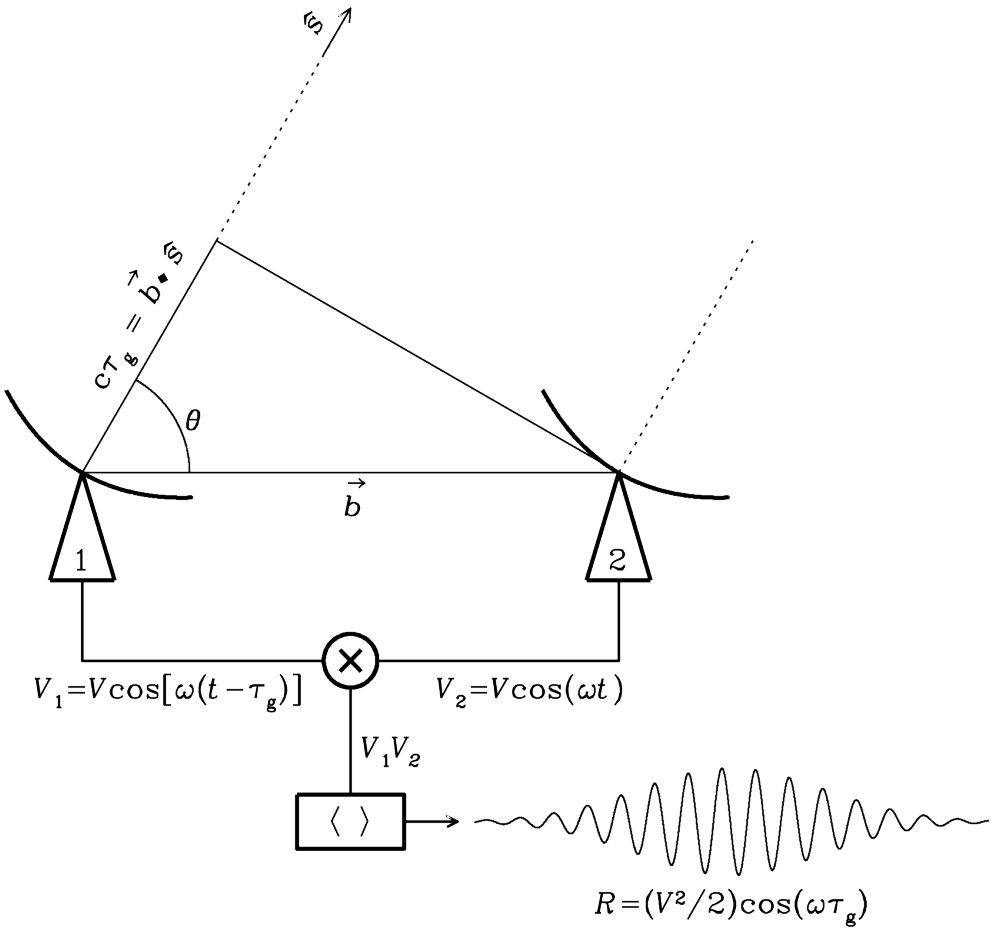

Figure 2.1: The two-element interferometer observing a point source in a very narrow frequency range centered on $\nu = \omega/2\pi$. The correlator multiplies and averages the voltage outputs V_1 and V_2 of the two dishes. The output voltage V_1 of antenna 1 is the same as the output voltage V_2 of antenna 2, but it is retarded by the geometric delay $\tau_g = \vec{b} \cdot \hat{s}/c$. These voltages are multiplied and time averaged by the correlator to yield an output response whose amplitude R is proportional to the point-source flux density and whose phase depends on the delay and the frequency. The quasi-sinusoidal output fringe shown occurs if the source direction in the interferometer frame is changing at a constant rate $d\theta/dt$. Credit: NRAO.

The synthesized beam of an interferometer is an important quantity as it defines the maximum angular resolution of the instrument. The synthesized beams produced by an interferometer with a various number of antennas arranged in 1-D is shown in Figure 2.2.

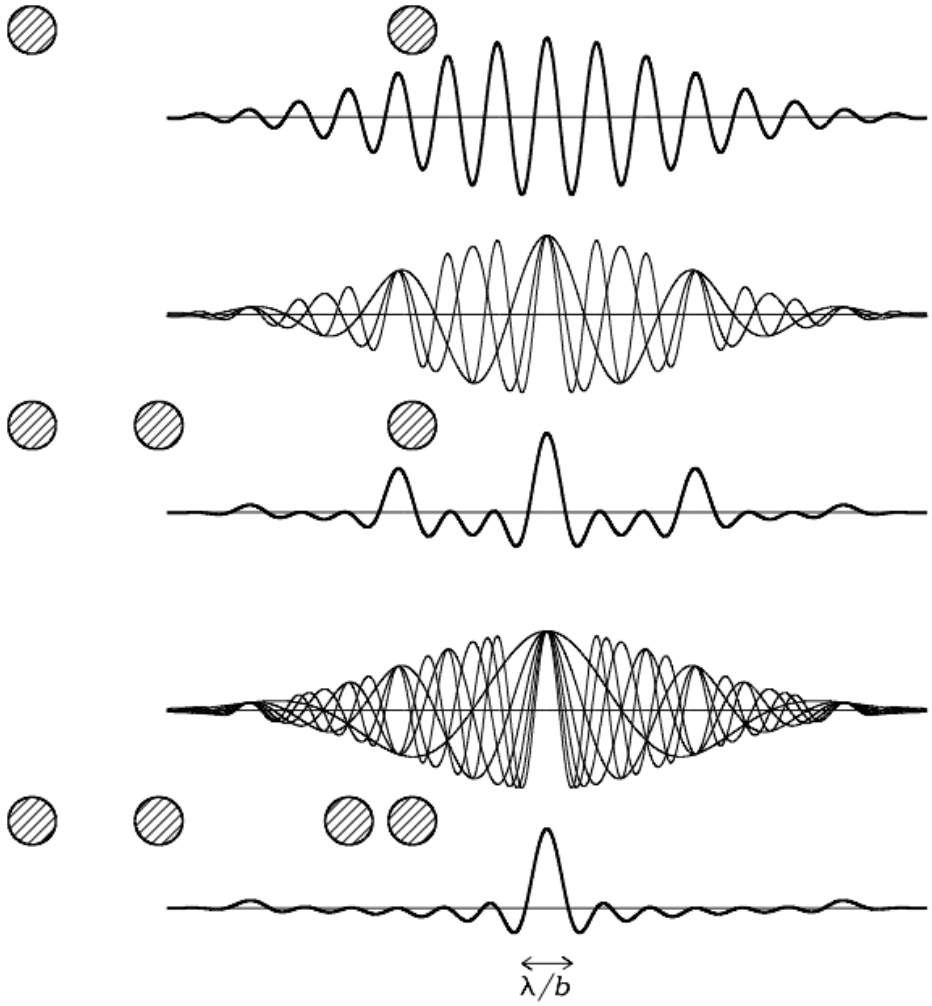

Figure 2.2: The instantaneous responses of an interferometer with two, three and four elements is indicated by the thick curves. The individual responses of the three pairs of two-element interferometers of the three-element interferometer and the six pairs of two-element interferometers of the four-element interferometer are plotted as thin curves. The main beam of the four-element interferometer is nearly Gaussian and has a width of $\sim \lambda/b$. This is known as the instantaneous synthesized beam of the interferometer or point spread function (PSF). Credit: NRAO.

2.3 The complex visibility

From Equation 2.4 we notice that the even cosine function in this response is sensitive only to the even (inversion-symmetric) part of an arbitrary source brightness distribution I. To detect the odd part of I we need a "sine" correlator whose output is odd,

$$R = \frac{V^2}{2}\sin(\omega\tau_g) \equiv Im(t) \tag{2.6}$$

This is implemented by a second correlator that follows a 90 phase delay inserted into the output of one antenna. Combining Equations 2.4 and 2.5, we can define the *complex visibility*:

$$V = Re(t) - iIm(t) = \frac{V^2}{2}e^{-i\omega\tau_g} \tag{2.7}$$

Thus, for a simple two-element interferometer, the components $Re(t)$ and $Im(t)$ are generated simultaneously to construct the *complex visibility function*.

2.4 Response to an extended source and the *u-v* plane

For an extended source, the response of the interferometer can be considered as the addition of the visibilities corresponding to a set of point-like sources. From Equation 2.7:

$$V = \frac{1}{2}\int I(\hat{s})e^{-i\omega\tau_g}d\Omega = \frac{1}{2}\int I(\hat{s})e^{-i\frac{2\pi}{\lambda}\vec{b}\cdot\hat{s}}d\Omega \tag{2.8}$$

where $d\Omega$ is the differential solid angle subtended by the source. In order to recover the intensity distribution $I(\hat{s})$ from the visibility V, and to simplify the calculations, we assume a reference point of the extensive source such that the vector pointing to that point (defined as $\hat{s}_0$) is orthogonal to the baseline vector $\vec{b}$.

We can define a coordinate system $(\vec{U},\vec{V},\vec{W})$, where the axes $(\vec{U},\vec{V})$ are in the plane orthogonal to $\hat{s}_0$, and the axis $\vec{W}$ is, thus, proportional to $\hat{s}_0$ (see Figure 2.3). If (x,y,z) are the coordinates of the vector $\hat{s}$ in the base $(\vec{U},\vec{V},\vec{W})$, with x and y being parallel to the right ascension and declination, respectively, in the field around the source, then $(u,v,0)$ are the coordinates of $\vec{b}$ and the scalar product

$$\vec{b}\cdot\hat{s} = ux + vy \tag{2.9}$$

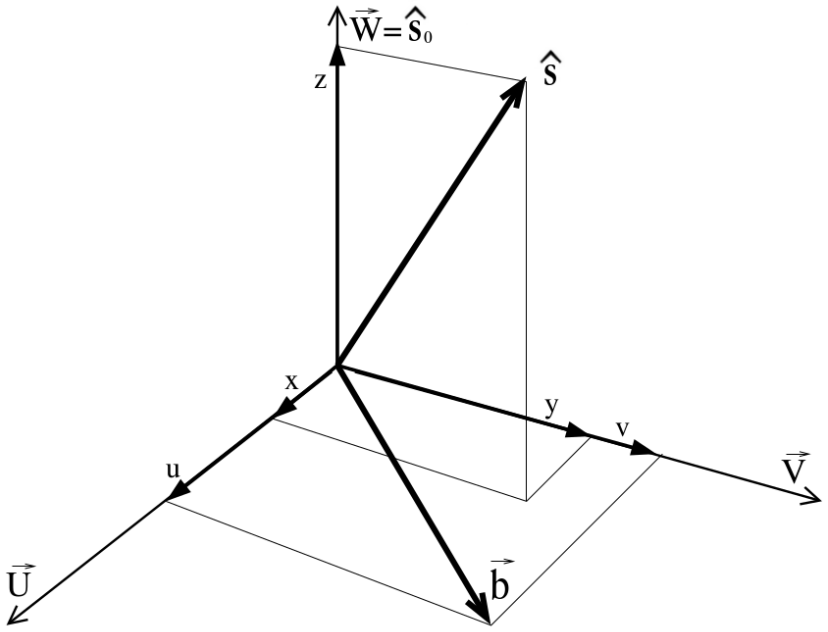

Figure 2.3: Definition of the coordinate system $(\vec{U},\vec{V},\vec{W})$.

Furthermore, the solid angle $d\Omega$ can be written as

$$d\Omega = \frac{dxdy}{\sqrt{1-x^2-y^2}} \tag{2.10}$$

so that

$$V(u,v) = \frac{1}{2}\int I(\hat{s})e^{-i\frac{2\pi}{\lambda}(ux+vy)}\frac{dxdy}{\sqrt{1-x^2-y^2}} \tag{2.11}$$

If we also consider that the source is compact $(x << 1, y << 1)$, the visibility function can be expressed as

$$V(u,v) = \frac{1}{2}\int_{-\infty}^{\infty}\int_{-\infty}^{\infty} I(x,y)e^{-i\frac{2\pi}{\lambda}(ux+vy)}dxdy \tag{2.12}$$

Thus, the complex visibility $V(u,v)$ is the 2D Fourier transform of the brightness distribution $I(x,y)$ on the sky. This result, related to the *van Cittert-Zernike theorem*, is the base of the synthesis imaging technique.

Since $I(x,y)$ is real, $V(u,v)$ is Hermitian, i.e., $V(-u,-v) = V^*(u,v)$, and so one measurement of the sky brightness gives two measurements of the complex visibility. The set of (u,v) pairs, which corresponds to the coordinates of the baseline vector, determine what is known as *uv coverage*.

2.5 Aperture synthesis and imaging

The number of visibilities that we have in the *uv* plane is finite. The more visibility measurements we have, the more reliable will be the reconstructed intensity distribution $I(x,y)$ of the radio source. To improve the sampling of the *uv* plane we can, of course, increase the number of antennas involved in the observation, but above all, take advantage of the rotation of the Earth.

From Figure 2.1, we notice that the rotation of the Earth causes that the length and the angle of the vector $\vec{b}$ change over time, sampling then different points of the *uv* plane. The trajectories that define the (u,v) points of each baseline according to the rotation of the Earth are known as *uv*-tracks. This is the base of the technique known as *Earth-rotation aperture synthesis*, designed by Martin Ryle and Anthony Hewish at Cambridge University in the mid-twentieth century, and for which they received the Nobel Prize in Physics in 1974.

An array of antennas will only measure the visibility function $V(u,v)$ at a certain set of values. The measured set is called the *sampling function* $S(u,v)$:

$$S(u,v) = \sum_k \delta(u-u_k, v-v_k) \tag{2.13}$$

This function is zero where no data have been taken and the actual data provided by the array is known as the sampled visibility function, $S(u,v)V(u,v)$. Taking the inverse Fourier transform of the sampled visibility function:

$$I^D(x,y) = FT^{-1}\left\{S(u,v) \times V(u,v)\right\} \tag{2.14}$$

Applying the convolution theorem:

$$I^D(x,y) = b(x,y) \otimes I(x,y) \tag{2.15}$$

where $b(x,y) = FT^{-1}\left\{S(u,v)\right\}$ is the *point spread function* (PSF), or *synthesized beam*, or *dirty beam* (i.e., the inverse Fourier transform of the sampling function $S(u,v)$). Equation 2.14 means that the the Fourier transform of the sampled visibilities yields the true sky brightness convolved with the point spread function. In other words, the "dirty image" is the true image convolved with the "dirty beam".

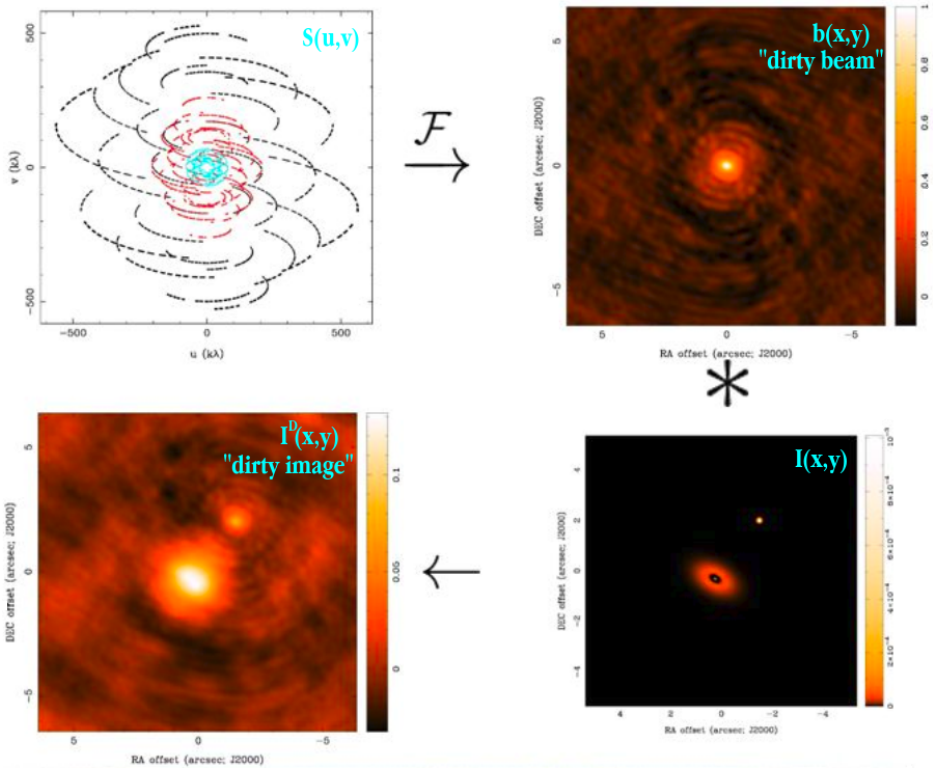

Figure 2.4: Top: a real example of a sampling function $S(u,v)$ and its corresponding dirty beam $b(x,y)$. Bottom: the dirty image $I^D(x,y)$ obtained after convolving the source intensity distribution $I(x,y)$ with the dirty beam. Credit: NRAO synthesis imaging workshop lectures.[1]

A real example of the different functions is shown in Figure 2.4. Before the dirty image is computed, a weighting function $W(u,v)$ is often applied to the visibilities to change the shape of the dirty beam, so that $S(u,v) \rightarrow S(u,v)W(u,v)$. The three most common types of weighting functions used are:

- **Natural weighting:** $W(u,v) = 1/\sigma^2_{u,v}$ in occupied (u,v) cells, where $\sigma^2_{u,v}$ is the noise variance, and $W(u,v) = 0$ everywhere else. This function maximizes point source sensitivity and generally gives more weight to short baselines (low spatial frequencies). Hence, angular resolution is degraded but provides the lowest rms in the image.

[1] https://science.nrao.edu/science/meetings/2014/14th-synthesis-imaging-workshop/lectures

- **Uniform weighting:** $W(u,v) = 1/\rho(u,v)$, where $\rho(u,v)$ is the local density of (u,v) points. This function fills the *uv* plane weights more uniformly and gives more weight to long baselines (high spatial frequencies), so angular resolution is enhanced. The dirty beam sidelobes are lower and some data are downweighted, so point source sensitivity is degraded.

- **Robust (Briggs) weighting:** This is a variant that avoids giving too much weight to (u,v) cells with low natural weight. It allows continuous variation between optimal resolution (uniform weighting) and optimal noise properties (natural weighting).

Since the sampling of visibilities in the *uv* plane is incomplete (especially for VLBI, where small numbers of antennnas often mean extremely sparse sampling), the use of non-linear techniques to interpolate/extrapolate samples of $V(u,v)$ into unsampled regions of the *uv* plane is needed. Thus, to obtain the true sky brightness distribution, it is necessary to "deconvolve" the effects of limited visibility sampling.

Several algorithms have been developed to make use of *a priori* information to find a global solution for the true sky brightness, which is complicated by the fact the the measured visibilities are corrupted by noise. Popular examples of imaging algorithms include CLEAN (Högbom, 1974), least squares model fitting (e.g., Martí-Vidal et al., 2014), maximum entropy (MEM, Ables, 1974) and various derivatives and combinations of the above. In this thesis, both CLEAN and model fitting were used.

2.5.1 Deconvolution: the CLEAN algorithm

The CLEAN algorithm (Högbom, 1974) is the most widely used technique in radio interferometry to deconvolve the true sky intensity from the dirty beam. It assumes that the radio source can be represented by a number of point sources in an otherwise empty field and a simple iterative process is used to find the strengths and positions of these point sources.

The final CLEAN image (i.e., the deconvolved image) is the sum of these point sources convolved with a CLEAN beam, which is usually the elliptical Gaussian that best fits the main lobe of the dirty beam.

The CLEAN algorithm obeys the following steps:

1. Find the strength and position of the brightest point in the dirty image. It may also be desirable to search for peaks in specified areas of the image, called CLEAN windows, regions or masks.
2. At this position in the dirty image, subtract the dirty beam centered at the intensity peak multiplied by the peak strength and a damping factor g ($g \leq 1$, usually called the *loop gain*).
3. Record the position and the subtracted flux in a list of model components.
4. Iterate between (1), (2), and (3) until the peak is below some user specified level. The remainder of the dirty image is now termed *the residuals*.
5. Convolve the accumulated point source model with an idealized CLEAN beam (usually an elliptical gaussian of the same size and shape as the central lobe of the dirty beam).
6. Add *the residuals* to the image in (5) to create the final CLEAN image.

This is the basic description of the so-called "minor cycles" of the CLEAN algorithm. However, there is also another (outer) loop known as "major cycle", where the Fourier transform of the CLEAN model is subtracted from the visibilities (i.e., in Fourier space) and a new (residual) dirty image is generated. This is done to avoid gridding-related artifacts in the image plane.

A problem with CLEAN derives from the fact that it is a non-parametric algorithm, so that the final CLEANed image is somewhat dependent upon the various control parameters such as CLEAN boxes, the loop gain and the number of CLEAN subtractions. Furthermore, the output image model does not give us direct information about the source properties. These have to be further derived (i.e., fitted) from the image. In contrast, parametric methods extract the required source information (e.g., size, flux, etc.) directly from the observables. A more detailed discussion about this is presented in Sections 2.7.4 and 2.7.5.

2.5.2 Model fitting[2]

In contrast to the CLEAN algorithm, there exist parametric techniques to recover the sky intensity distributions of the sources. If the number of elements in the interferometer is large and the spatial distribution of the array is not sparse, the structure of the observed sources can be recovered with a high fidelity, using non-linear

[2]Based on Martí-Vidal et al. (2014), where they introduce the UVMULTIFIT tool used in this thesis.

image-reconstruction algorithms (e.g., CLEAN, Högbom, 1974). However, if the array is sparse as with VLBI, the image reconstruction may depend strongly on the particulars of the deconvolution algorithm. Thus, the images resulting from these reconstruction algorithms are not *direct* and *unique* representations of the data, but rather non-unique *interpretations* of the actual measurements. Any analysis based on interferometric images (especially those coming from sparse arrays) therefore needs to be understood as *fitting models to models*, in the sense that the images themselves are the result of a non-linear mapping from the Fourier domain into the sky plane. This problem can be especially important when comparing images at different frequencies, epochs, or taken with different interferometers, unless the imaging processes of the different datasets are performed self-consistently.

In the cases where the structure of the observed source is simple and/or can be parametrized using simple models, it is possible to bypass the imaging of the visibilities and work directly on the interferometric measurements, fitting a model to the visibilities instead of to the images obtained from deconvolution algorithms. In this work we make use of the UVMULTIFIT tool (Martí-Vidal et al., 2014) to recover the intensity distribution of the sources in the S5 polar cap sample (see Chapter 4).

2.6 Interferometric arrays used in this thesis

In this thesis we use data from multiple radio interferometers, i.e., arrays of radio telescopes. When the separation of the different elements (antennas) of the interferometer is so large that it is not possible to connect them physically, we talk about *Very Long Baseline Interferometry* (VLBI). An example of a VLBI array is the VLBA. In VLBI arrays, each station needs a very precise atomic clock and stable maser, and the received signals are recorded on tapes or disks for later correlation. Instead, when the different antennas of the interferometer are connected via waveguides, optical fibers or radio links, we talk about *connected interferometry*. An example of a connected array is ALMA. This section provides a brief overview of both interferometers: VLBA and ALMA.

2.6.1 VLBA

The Very Long Baseline Array (VLBA) is an interferometer consisting of 10 identical antennas on transcontinental baselines up to 8000 km, from Mauna Kea, Hawaii, to St. Croix, Virgin Islands (Figure 2.5). The VLBA is controlled remotely from the Science Operations Center in Socorro, New Mexico (USA). Each VLBA station consists of a 25-m antenna and an adjacent control building.

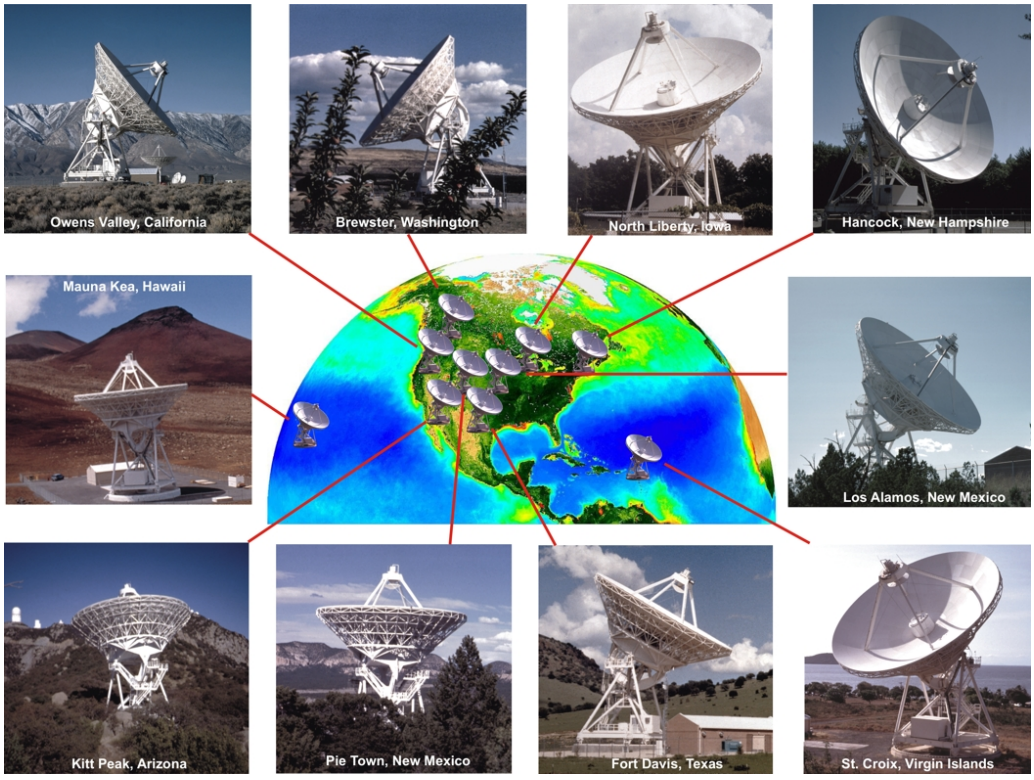

Figure 2.5: Antennas. Image courtesy of NRAO/AUI and Earth image courtesy of the SeaWiFS Project NASA/GSFC and ORBIMAGE.

The received signals are amplified, digitized, and recorded on fast, high capacity recorders. The recorded data are sent from the individual VLBA stations to the correlator in Socorro.

The VLBA observes at wavelengths ranging from 28 cm to 3 mm (1.2 GHz to 96 GHz) in eight discrete bands plus two narrow sub-gigahertz bands, including the primary spectral lines that produce high-brightness maser emission. The array can be scheduled dynamically, and its continuum sensitivity can be improved by a factor of 5 or more by adding the Green Bank Telescope (GBT) and the phased Very Large Array (VLA) to the VLBA. More information about the VLBA can be found at the NRAO webpage.[3]

[3] `https://science.nrao.edu/facilities/vlba`

Figure 2.6: Antennas of ALMA, on the Chajnantor Plateau in the Chilean Andes. The Large and Small Magellanic Clouds, two companion galaxies to our own Milky Way galaxy, can be seen as bright smudges in the night sky, in the centre of the photograph. Credit: ESO/C. Malin.

2.6.2 ALMA

The Atacama Large Millimeter/submillimeter Array (ALMA) is the world-largest ground-based facility for observations in the millimeter/submillimeter regime located on the Chajnantor plateau, at 5000 meters altitude in northern Chile (Figure 2.6). The array consists of 66 antennas in total, which can be configured to achieve baselines up to 16 km. It is equipped with state-of-the-art receivers that cover all the atmospheric windows up to 1 THz. The antennas can be placed in different locations on the plateau in order to form arrays with different distributions of baseline lengths. More extended arrays will give higher spatial resolution, while more compact arrays give better sensitivity for extended sources.

The complete set of 66 antennas is composed of fifty 12-m antennas, and the Atacama Compact Array (ACA), which consists of twelve 7-m antennas and other four 12-m antennas. ACA mostly stays in a fixed configuration and is used to image large scale structures that are not well sampled by the ALMA 12-m array. More details and up-to-date information can be found in the ALMA Science

Portal,[4] from where the following information has been extracted.

ALMA delivers data cubes with three axes: right ascension, declination, and frequency. In this sense, the final data products are very much like those of an integral field unit with up to a million spectral pixels. The main properties of ALMA are summarized in the following items:

- **Observing frequencies:** The frequency range available to ALMA is divided into different receiver bands. Data can only be taken in one band at a time. These bands range from band 3, starting at 84 GHz, to band 10, ending at 950 GHz. For comparison, a frequency of 300 GHz translates to a wavelength of approximately 1mm. Band 1 around 40 GHz is under construction, and band 2 around 80 GHz might be added in the future.

- **Field of view:** The full width at half maximum (FWHM) of the primary beam is $21''$ at 300 GHz for a 12-m antenna and a $35''$ for a 7-m antenna, and scales linearly with wavelength (diffraction limit of a single antenna, as opposed to that of the whole array). To achieve uniform sensitivity over a field larger than about a few arcsecs, or to image larger regions than the primary beam, mosaicking is required, which is a standard observing mode for ALMA.

- **Spatial resolution:** In the most compact 12-m array configurations, resolutions range from $0.5''$ at 950 GHz to $4.8''$ at 110 GHz. In the most extended 12-m array configuration, the resolutions range from 20 mas at 230 GHz to 43 mas at 110 GHz. These numbers refer to the FWHM of the synthesized beam (point spread function), which is the inverse Fourier transform of a (weighted) u-v sampling distribution.

- **Array configurations:** The ALMA 12-m array changes from its most compact configuration, with maximum baselines of ~ 150 meters, to its most extended configuration, with maximum baselines of ~ 16 kilometers. The ACA has two configurations, one of which is a north-south extension to provide a better beam shape for far-north/far-south targets.

- **Spectral resolution:** ALMA can deliver data cubes with up to 7680 frequency channels (spectral resolution elements). The width of these channels can range between 3.8 kHz and 15.6 MHz, but the total bandwidth cannot exceed 8 GHz. At an observing frequency of 110 GHz, the highest spectral resolution implies a velocity resolution of 0.01 km/s, or $R = 30,000,000$, where $R = \lambda/\Delta\lambda$ gives us a measure of the ability of ALMA to resolve different spectral features.

[4] ALMA Science Portal: `https://almascience.eso.org/`

- **Sensitivity:** For an interferometer, the noise level (in mJy) in the resulting data cubes scales roughly as $S \propto T_{sys}/(A \times N^2(N_p \times \Delta\nu \times \Delta\tau)^{1/2})$, where T_{sys} is the system temperature of the receiver at each single antenna, A is the effective collecting area of each antenna (assuming an homogeneous array), N is the number of antennas, N_p is the number of polarizations, $\Delta\nu$ is the available bandwidth and $\Delta\tau$ is the observing time. For continuum observations, $\Delta\nu = 7.5$ GHz, for spectral line observations, $\Delta\nu$ is the channel width. In practice, continuum observation will result in four spectral windows each with a width of 1.875 GHz (after discarding edge channels). These four windows can be combined to form a single image with an effective frequency width of 7.5 GHz. The ALMA Sensitivity Calculator[5] can be used to estimate noise levels or required integration times to reach a desired noise level. The sensitivity is also a strong function of the atmospheric conditions. The troposphere has an effect on the optical depth, the atmospheric emission, and on the demands for calibration. The amount of water vapor in the atmosphere is measured as the precipitable water vapour (pwv). A value of pwv=1 mm is typical for the ALMA site.

2.7 VLBI Astrometry

The technique of VLBI provides the highest accuracy in the determination of coordinates, parallaxes, and proper motions of celestial sources. In particular, VLBI astrometry can achieve position accuracies of the order of a few microarcseconds. This level of accuracy corresponds to measuring the location of a tennis ball on the Moon as seen from the Earth with a precision of a few millimeters.

The astrophysical applications of VLBI astrometry are numerous. Examples are: the establishment and stability of celestial reference frames, the dynamics and structure of the Galaxy, the astrophysical processes in the core region of active galactic nuclei (AGN), and tests of general relativity. Possible target sources include pulsars, stars with radio continuum emission, and astrophysical masers.

In this section we describe the VLBI observables for astrometry, summarize the basics of relative and differential astrometry, and present some of the most common non-parametric methods used in VLBI astrometry. Finally, we introduce the differential astrometry technique used in this thesis, which provides the most accurate measurements.

For a more detailed review of VLBI astrometry, we refer the reader to, e.g., Bartel (2003), Bartel (2012), Schuh & Behrend (2012), and Reid & Honma (2014).

[5] `https://almascience.eso.org/proposing/sensitivity-calculator`

2.7.1 Astrometric observables

Interferometric phase

The fundamental observable in VLBI is the *interferometric phase* ϕ, which is the relative phase between the signals received at the telescopes of each baseline (e.g., telescopes 1 and 2 in Figure 2.1). This phase depends on time, baseline coordinates, and source direction, and is affected by several contributions:

$$\phi = \phi_g + \phi_{struc} + \phi_{trop} + \phi_{ion} + \phi_{inst} + 2\pi n \tag{2.16}$$

where ϕ_g is the phase caused by the geometric delay τ_g between the antennas (see Figure 2.1); ϕ_{struc} is the phase due to the source structure; ϕ_{trop} and ϕ_{ion} are the phases introduced in the propagation of the signal through the troposphere and ionosphere, respectively; ϕ_{inst} is caused by the instrumentation of the antennas; and $2\pi n$ is an integer number of phase cycles.

The correlator output voltage $R = (V^2/2)\cos(\omega\tau_g)$ in Equation 2.5 varies sinusoidally with the change of source direction in the interferometer frame, i.e., as the source moves across the sky. These sinusoids are called *fringes*, and the fringe phase

$$\phi = \omega\tau_g = \frac{\omega b \cos\theta}{c} \tag{2.17}$$

is thus the phase of the sinusoidal oscillations (the fringes) of the correlator response in Equation 2.5. In the field of VLBI astrometry, three main observables are defined based on the interferometric phase: *phase delay, group delay* and *delay rate*.

Phase delay

The *phase delay* is defined as:

$$\tau_\phi = \frac{\phi}{2\pi\nu_0} \tag{2.18}$$

where ϕ is the interferometric phase and ν_0 is the observing reference frequency. The phase delay is by far the most precise observable in VLBI astrometry. However, interpretation of the fringe phase requires resolving the inherent ambiguity, i.e., determining the number of phase cycles n in Equation 2.16.

The prediction of the number of cycles requires a very accurate geometric model, so in many cases the phase delay cannot be used directly. In phase-delay parametric astrometry (see Chapter 4), this is accomplished iteratively through a *phase-connection* procedure (e.g., Shapiro et al., 1979; Martí-Vidal et al., 2008).

When all integers, n, are determined, the phase delays are no longer ambiguous and can be used to estimate, via a weighted least-squares fit, the position of the radio sources.

Group delay

The *group delay* is defined as:

$$\tau_G = \frac{1}{2\pi}\frac{\partial\phi}{\partial\nu} \tag{2.19}$$

and gives the change of the phase with frequency (slope) along the observing bandwith. Although much larger than that of the phase delay, the ambiguity of the group delay is still present. However, in practical matters, the solving of these ambiguities during the data calibration is trivial. The group-delay ambiguity is that for which the slopes between two neighboring frequency channels increases by 2π. Hence, it is dependent on the spectral resolution used in the correlation.

Delay rate

The *delay rate* is defined as:

$$\dot{\tau}_\phi = \frac{1}{2\pi\nu_0}\frac{\partial\phi}{\partial t} \tag{2.20}$$

and gives the change of the phase with time. As with the group delay, this observable is less precise than the phase delay and is ambiguous in a trivial manner, so that a rate so high that neighboring integration times differ by 2π, would be ambiguous. Again, increasing the time resolution (i.e., decreasing the integration time at the correlator) makes this ambiguity rate larger.

2.7.2 Phase calibration: fringe fitting

As shown in Equation 2.16, there are several contributions affecting the value of the measured interferometric phase. At the correlator, a model of (among other effects) earth rotation, atmosphere, source positions, and station clocks is applied to determine their contribution to the phase and remove them from the data. However, after the correlation, and due to the limited precision of the model, the phases on a target source still can exhibit high residual fringe rates and delays. Before imaging, these residuals should be removed to permit data averaging in time and, for a continuum source, in frequency. The process of finding these residuals is referred to as *fringe fitting* (Cotton, 1995).

In the fringe fitting approach, it is assumed that the time dependence of the phase gains is linear and the amplitude of the source visibility remains constant over the range of (t, ν) space covered by the observation. Then, for each baseline, the peak of the fast Fourier transform (FFT) of the visibilities is searched in the delay-rate space, and the residual phase, group delay and delay rate are determined.

The standard calibration procedure in VLBI is *Global Fringe Fitting* (GFF, Schwab & Cotton, 1983). GFF is the only calibration procedure that ensures robustness of the closure-phase observables, which in turn make aperture-synthesis imaging possible. Besides, GFF is used regardless of the S/N of the observations. This approach solves for the antenna-dependent delays and delay-rates referred to a reference antenna, for which both values are set to zero

2.7.3 Fundamentals of relative astrometry

With a radio interferometer we can measure the arrival time difference of wavefronts between antennas, i.e., the geometric delay, owing to the finite propagation speed c of electromagnetic waves. Equation 2.2 relates the geometric delay, τ_g, to the source unit vector, $\hat{s}$, and the baseline vector, $\vec{b}$.
In Figure 2.7, we show the geometry of these vectors. Note that while the source vector $\hat{s}$ has two parameters (e.g., right ascension and declination), the geometric delay is a scalar, and so multiple measurements of geometric delays are required to solve for a source position. Such measurements can be made, even with a single baseline, by utilizing the rotation of the Earth, which changes the orientation of the baseline vector with respect to a celestial frame.

From Equations 2.16 and 2.18, the delay measured with an interferometer can be considered as the sum of the geometric delay (which we would like to know) and additional terms (which need to be removed from the data):

$$\tau_\phi = \tau_g + \tau_{struc} + \tau_{trop} + \tau_{ion} + \tau_{inst} + \frac{n}{\nu_0} \tag{2.21}$$

where τ_g is the contribution from the geometry of the interferometer and the fiducial reference point in the source; τ_{struc} is the delay due to unmodeled source structure; τ_{trop} and τ_{ion} are the delays in the propagation of the signal through the troposphere and ionosphere, respectively; τ_{inst} is caused by an error in the location of the antennas, the instrumental delay in the telescope or electronics, and the thermal noise; and n is an integer number of phase cycles.

For relative astrometry, one observes two sources, the target and reference, at nearly the same time and nearly the same position in the sky, and differences the observed delays (phases) between the pair of sources. This type of observation

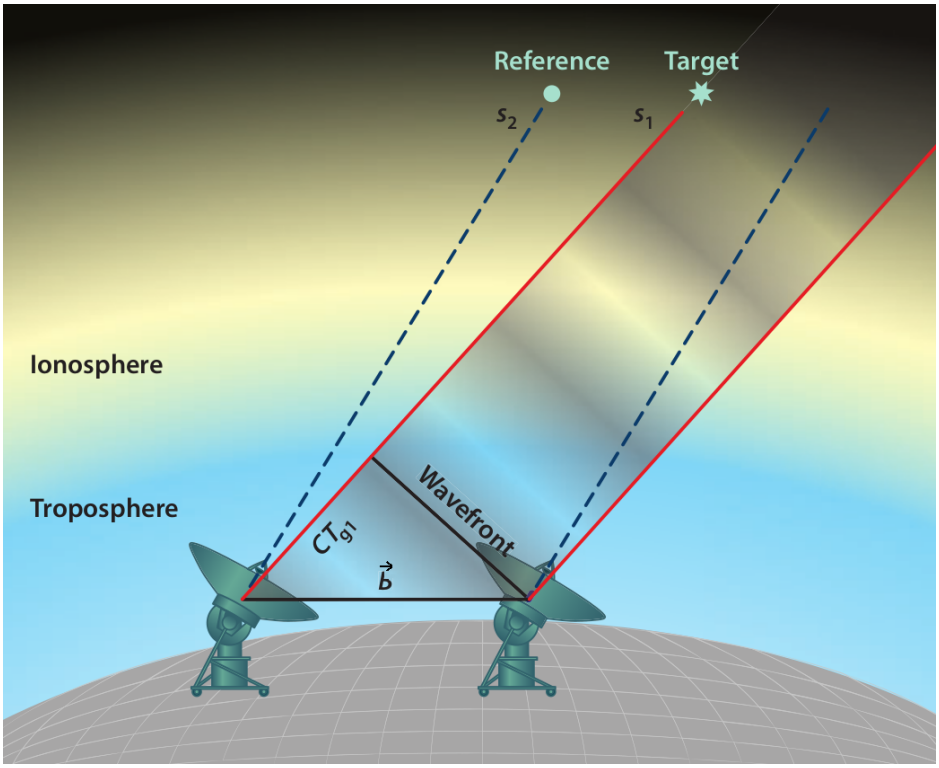

Figure 2.7: Schematic view of a delay measurement in phase-referencing astrometry. Here, for simplicity, an array with two stations is shown. The baseline vector and source directions are indicated by lines. In relative astrometry, the target and adjacent reference sources are observed (nearly) at the same time, thus delay errors can be effectively canceled in the relative measurement. For relative radio astrometry, the dominant sources of error are generally propagation delays in troposphere and/or ionosphere which are not compensated. Credit: Reid & Honma (2014).

is often referred to as phase-referencing, as the observed phase of the reference source is used to correct the phase of the target.

Computing the difference between the two sources, we obtain the delay difference observable (e.g., Reid & Honma, 2014):

$$\Delta\tau_{\phi}^{1-2} = \Delta\tau_{g}^{1-2} + \Delta\tau_{struc}^{1-2} + \Delta\tau_{trop}^{1-2} + \Delta\tau_{ion}^{1-2} + \Delta\tau_{inst}^{1-2} + \frac{n'}{\nu_0} \tag{2.22}$$

where superscripts 1 and 2 denote the quantities for the target and reference sources, respectively. The first term is the difference in geometric delay between the source and reference, which corresponds to the relative position of the target source with respect to the reference source. The additional terms in Equation 2.22

may be reduced if they are similar for the two lines of sight. Four terms (τ_{trop}, τ_{ion}, τ_{struc}, τ_{inst}) are antenna-dependent quantities and generally are similar for the target and reference lines of sight, for small source separations. The difficulty will be to determine the integer, n', for each interferometer phase delay.

In the next section, the most common methods used to perform relative astrometry are presented.

2.7.4 Non-parametric observing methods

There are several methods to obtain the relative position between sources, i.e., to perform relative astrometry. Here we summarize some non-parametric methods, whose peculiarity is that the information about the source properties is obtained after fitting from the output image model instead of directly from the observables.

Phase-referencing

Several methods of phase-referencing commonly used in VLBI are:[6]

- *Source switching* or nodding, which is the most commonly used observing method, because it does not require a special radio telescope and can be used for all source pairs. The only requirement is that slewing times between antennas need to be short enough to track the tropospheric phase fluctuations. Because of the nondispersive nature of tropospheric delays, the interferometer coherence time scales linearly with wavelength, i.e., $\tau_{coh} \propto \lambda$. Thus, at short wavelengths, the coherence time can be problematic. For an observing wavelength of $\lambda = 1.3$ mm ($\nu = 230$ GHz), the coherence time is likely to be ~ 10 s (under good weather conditions). This makes it practically impossible to conduct switched VLBI observations below 1 mm wavelength.

- In *dual-beam* observations, two sources are observed simultaneously using independent feeds and receivers. This can be done using multifeed systems on a single antenna, as with VLBI Exploration of Radio Astrometry (VERA), or with multiple antennas at each site (Rioja et al., 2009; Broderick et al., 2011). There is no gap between the observations of the target and reference sources, and hence there is no coherence loss owing to phase fluctuations. In dual-beam radio astrometry, special care needs to be taken to calibrate the instrumental delay, because it is not the same for the target and reference source and thus will not cancel when phase-referencing.

[6]Extracted from Reid & Honma (2014), where a detailed discussion of the different methods is presented.

- *In-beam* observations can be regarded as a special case of phase-referencing, in which the target and reference sources are so closely located that the two sources can be observed simultaneously with a single feed (within the primary beam of each antenna). In such a case, calibration errors can be very effectively reduced, because the observations are done at the same time for the target and reference and, because the separation angle is small, most systematic errors are largely canceled (Marcaide, 1982; Marcaide & Shapiro, 1984). However, finding a sufficiently strong reference source may be difficult; as such, in-beam observations are more common at lower observing frequencies, as the primary beam becomes larger and the reference sources stronger.

In phase-referenced mapping, one way to measure the relative separation between calibrator and target is to image the phase-calibrated target source and find the position of the target source relative to the image center. From this position offset and the assumed positions of target and reference used at correlation the relative positions of target and reference can be found. For a deeper discussion about VLBI phase-referencing, see, e.g., Beasley & Conway (1995).

Source-frequency phase-referencing

An alternative method to perform high-precision VLBI astrometry is presented in Dodson & Rioja (2009); Rioja & Dodson (2011). The source-frequency phase referencing (SFPR) method combines fast frequency-switching observations (e.g., Middelberg, 2005), to correct for the dominant non-dispersive tropospheric fluctuations, with slow source-switching observations, for the remaining ionospheric dispersive terms. This approach enables high-precision astrometry even at the highest frequencies where conventional phase-referencing techniques fail.

The use of frequency-switching observations increases the coherence time as a result of the dual-frequency tropospheric calibration, which enables the detection of weak sources (Middelberg, 2005). However, remaining dispersive errors still need to be corrected in order to provide high-precision astrometry. This is achieved with a two-step calibration strategy: the first step assumes that the dominant tropospheric residual errors (and in general, any non-dispersive errors) in the target data set can be removed using the observations at a lower reference frequency, on the same source. The second step assumes that the remaining ionospheric and instrumental errors (and, in general, any other dispersive errors) can be removed using the interleaved observations of an external calibrator source (Rioja & Dodson, 2011).

In Chapter 4 we make use of a slightly modified version of the SFPR technique to obtain the core-shift of the sources of the S5 polar cap sample.

2.7.5 A parametric method: differential phase-delay astrometry

Another method to determine relative positions is to observe two neighboring sources and determine their relative phases, either simultaneously (if they are both within the primary antenna beam of each element of the interferometer), or alternately (if switching between sources is needed). The observation of neighboring sources cancels out most of the systematic effects in the astrometric data reduction, since they are mostly common for both. That is the basis of *differential phase-delay astrometry*, where most of the geometric parameters involved in the observation are taken into account during the correlation process, leaving one to work with the residuals (e.g., Shapiro et al., 1979; Marcaide, 1982; Marcaide & Shapiro, 1983; Bartel et al., 1986).

From Equation 2.22, assuming both sources are strong enough to be detected, we can remove $\Delta\tau_{struc}$ by using hybrid maps from the two sources, provide an *a priori* model for $\Delta\tau_{trop}$, $\Delta\tau_{ion}$, and $\Delta\tau_{inst}$, and determine all integers n' through the phase-connection procedure. Thus, we can obtain $\Delta\tau_g^{1-2}$ (which is directly related to the relative position between the sources), as well as corrections for $\Delta\tau_{trop}$, $\Delta\tau_{ion}$, and $\Delta\tau_{inst}$, via a weighted least-squares fit.

The power of the phase-delay astrometry analysis relies on the possibility of a simultaneous fit of all the parameters that define both the geometric and the instrumental components of the interferometer, such as clock drifts, position of the antennas, and tropospheric/ionospheric delays, together with the source positions. All these parameters are optimized self-consistently in the analysis, as opposed to other non-parametric approaches (e.g., phase referencing), where the instrumental and atmospheric effects are not properly parameterized and optimally accounted for all sources, but rather estimated and interpolated from one calibrator to a target.

Typically, the inclusion of the differential delays in the astrometric analysis improves the precision by roughly an order of magnitude, when compared to an ordinary phase-referencing analysis. This is due to the many redundancies present in the multi-source duty-cycle scheduling, and to the superior quality of a parametric astrometry analysis (i.e., fitting delays and phases to a complete geodetic + astrometric model) when compared to ordinary phase-referencing astrometry (where the geodetic + atmospheric models cannot be optimized). See Martí-Vidal (2008) and Martí-Vidal et al. (2008) for more complete comparative discussions about the astrometric precision with differential phase-delays.

Finally, phase-reference astrometry requires small angular separations between the sources (up to a few degrees), while phase-delay astrometry allows us to obtain the relative positions of sources spread across larger angular separations (e.g., Pérez-Torres et al., 2000; Martí-Vidal et al., 2008). In Chapter 4 we present an

application of the differential phase-delay astrometry technique at the 15 and 43 GHz bands for the sources of the S5 polar cap sample.

Chapter 3

AGN jets: relativistic outflows from the AGN cores

We are just an advanced breed of monkeys
on a minor planet of a very average star.
But we can understand the Universe. That
makes us something very special.

Stephen Hawking

In this chapter we summarize the main properties of AGN, mainly those of the structure and radio emission of the relativistic jets that emerge from the AGN cores. We briefly describe synchrotron self-absorption, which is the most likely absorption mechanism taking place in the jets, and introduce the *core-shift effect*. The chapter concludes by detailing the importance of the core-shift and presenting some of the most common methods used to determine it.

3.1 Properties and structure of AGN

The luminosity of most of the known galaxies is dominated in the optical by their stellar emission, but in some galaxies a significant fraction of the energy output has a non-thermal origin. These are called active galaxies or Active Galactic Nuclei (AGN), if the non-thermal emission comes mainly from the core.

Although AGN represent only a small fraction of all galaxies they have been studied intensively over the last decades at all accessible wavelengths. This is partly because their high luminosities made them the only objects that could be studied at cosmologically significant distances for a long time. At radio wavelength some active galaxies are the most luminous sources in the sky and were the first sources detected in the early days of radio astronomy (e.g., Baade & Minkowski, 1954).

These bright AGNs are among the strongest indirect proofs for the existence of supermassive black holes (SMBHs), although the enormous bursts in luminosity observed from AGN are not coming from the SMBHs themselves. Instead, the massive burst of radiation (which includes emission in the radio, microwave, infrared, optical, UV, X-ray, and gamma ray wavebands) is coming either from cold matter (gas and dust) that surround the black holes or from relativistic outflows (jets).

The accretion disks that orbit the SMBHs gradually feed the central engines. The innermost side of these disks is possibly the launching region of the relativistic outflows seen in radio-loud AGN (e.g., Marscher et al., 2008). The incredible force of gravity in this region compresses the material of the disk until friction and momentum transfer heat the disk's plasma up to millions of degrees kelvin. This generates bright electromagnetic radiation that peaks in the optical-UV waveband. A corona of hot material forms above the accretion disk as well, and can scatter photons up to X-ray energies.

A large fraction of the radiation of the AGN may be obscured by interstellar gas and dust close to the accretion disk, but will likely be re-radiated at the infrared waveband. As such, most (if not all) of the electromagnetic radiation is produced through the interaction of cold matter with the SMBH.

The interaction between the rotating magnetic field and the accretion disk also creates powerful magnetic jets that fire material perpendicular to the disk around the SMBH at relativistic speeds. These jets can extend over hundreds of thousands of parsecs, and are a second potential source of observed radiation (see Figure 3.1).

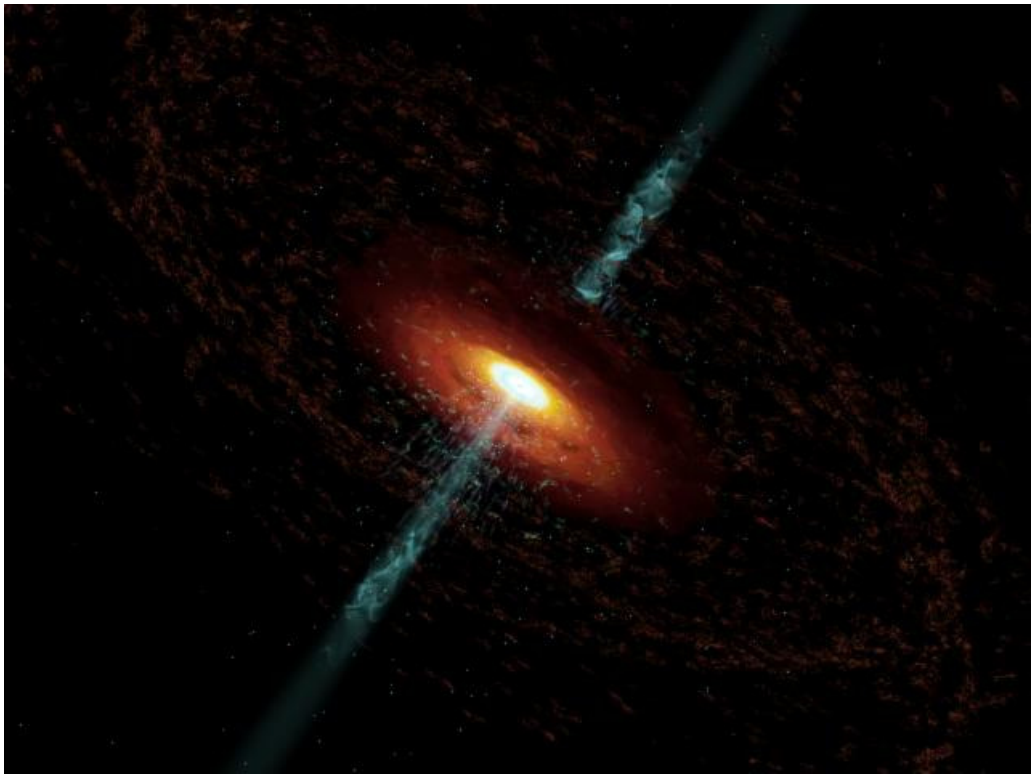

Figure 3.1: 3C 120 still frame from animation that illustrates the discovery discussed in Marscher et al. (2002). Courtesy of W. Steffen.[1]

AGN are the most luminous persistent sources of electromagnetic radiation in the universe, and as such can be used as a means of discovering distant objects. Their evolution as a function of cosmic time also puts constraints on models of the cosmos.

The physical structure of AGN is now quite well understood (Figure 3.2). According to the *Unified Model* (e.g., Lawrence, 1987; Antonucci, 1993; Urry & Padovani, 1995), an AGN is composed of:

- **Supermassive black hole (SMBH):** At the center of the AGN, with a mass of $M \sim 10^6 - 10^{10}\ M_\odot$.
- **Accretion disk:** Surrounding the SMBH there is a hot accretion disk of $\sim$ a few light days across ($r \sim 10^{-3}$ pc).

[1] `https://www.bu.edu/blazars/3c120.html`

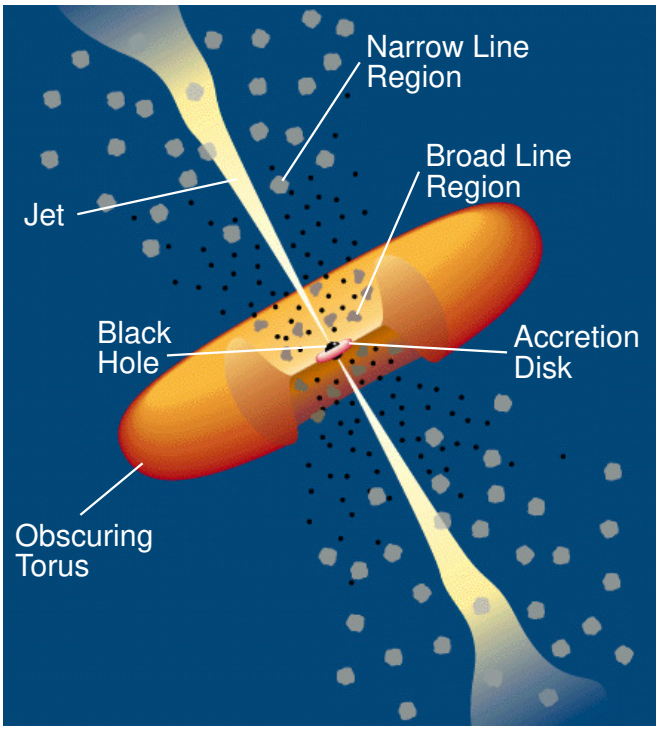

Figure 3.2: A schematic diagram of the Unified Model of AGN. Credit: Urry & Padovani (1995).

- **Broad Line Region (BLR):** At $r \sim 0.01 - 0.1$ pc the broad line region of a dense and fast rotating medium, with BLR clouds that are whirling around rapidly as they are quite close in to the AGN. These clouds yield optical emission lines with widths of thousands of $\mathrm{km\,s^{-1}}$ and have high electron densities of 10^9 $\mathrm{cm^{-3}}$ or higher.

- **Obscuring torus:** In the same plane as the accretion disk, colder material forms a torus around the central engine ($r \sim 10 - 100$ pc). This is an optically thick donut-shaped ring of cold gas and dust.

- **Narrow Line Region (NLR):** The NLR clouds are low-density ionized gas (electron densities $10^3 - 10^6$ $\mathrm{cm^{-3}}$) at $r \sim 100 - 1000$ pc. The NLR clouds are much further out from the AGN and so do not whirl around quite as fast as those of the BLR. The NLR optical emission lines have widths of hundreds of $\mathrm{km\,s^{-1}}$, and can be resolved.

- **Relativistic jets:** Perpendicular to the plane of accretion disk and torus, a radio-loud AGN exhibits collimated jets of relativistically outflowing material.

3.2 Internal structure and radio emission of jets

Jets of relativistic particles with magnetic fields are responsible for the radio emission. This emission is thought to be due to synchrotron radiation of relativistic electrons spinning along magnetic fields. These powerful and luminous sources are formed due to mass accretion onto the SMBH and part of the infalling matter is accelerated and ejected, forming a symmetric jet-counterjet-system (see Figures 3.1 and 3.2). This process covers an enormous range of linear scales; the jet is launched close to the AGN on scales of a few Schwarzschild radii (sub-parsec scales), while the jets can span several kiloparsecs ending sometimes in bright lobes. It is still not fully understood how jets form, and the composition of jets (leptonic or hadronic) and the underlying emission mechanisms to produce the observed broadband emission are a major topic of current research and requires further research and comparison to theoretical models.

Strong magnetic fields are thought to play an important role in the formation and propagation of the jets, and they are also necessary to produce the non-thermal emission (e.g., Blandford & Königl, 1979; Marscher, 1980).The magnetic field and the particle density in the jet decrease with distance from the AGN central engine, mainly due to the jet opening angle (e.g., Marscher, 1980; Lobanov, 1998b). As a result, extremely high magnetic fields may be found at short distances from the central engine (e.g., Martí-Vidal et al., 2015).

An illustration of the structure of a jet is shown in Figure 3.3. Based on the parametric model of the continuum emission from AGN jets (from radio to X-rays) described in Marscher (1980), a radio-loud AGN jet can be divided into three different parts:

1. The jet "nozzle" that connects the central AGN engine (i.e., the SMBH) to the physical base of the jet.

2. The collimation (or launching) region, where the trajectories of the electrons are focused towards the jet direction and the electrons of the plasma are accelerated to relativistic speeds. This small region in the jet base presents a *concave shape*.

3. The free region where the trajectory of the electrons of the plasma is believed to be ballistic. This region presents a *conical shape* and corresponds to the area usually observed, and resolved, in VLBI at mm/cm wavelengths.

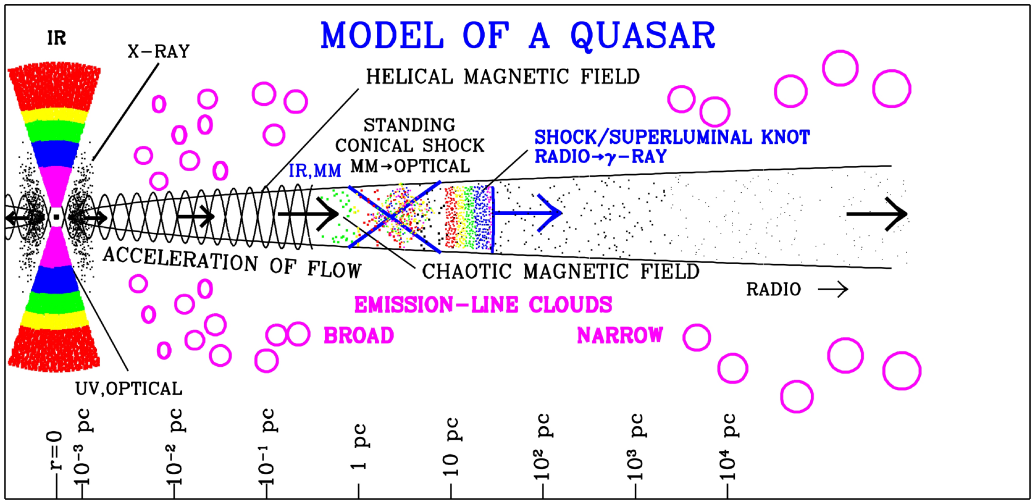

Figure 3.3: Illustration of the physical structure and emission regions of a radio-loud AGN, not including the extended radio lobe at the end of the jet. Credit: color version of Figure 1 in Marscher (2005).[2]

Although jets with constant opening angles (i.e., conical jets) can be used to model the spectra and the structures seen on VLBI scales (e.g., Lobanov, 1998b), deviations from simple conical structures have been found (e.g., Asada & Nakamura, 2012). From the theoretical point of view, departures from a conical shape jet are expected from magneto-hydrodynamic collimation effects close to the jet base.

Thus, despite the success of the standard jet model (Blandford & Königl, 1979) to explain the multiband spectra and the VLBI structures seen in many radio-loud AGN, the injection and launching mechanisms of the jets are poorly understood. It is believed that the accretion of material into the SMBH triggers the injection of plasma into the jet. However, the exact mechanism from which the material is brought from the infalling region of the accretion disk to the base of the jet is unknown.

Observational constraints on the emission from the regions involved in this process (e.g., Marscher et al., 2008) are essential for the progress of the theoretical models. However, these constraints are limited owing to the large distances to these objects and the small spatial scales (sub-parsec) involved.

[2]Research of the Blazar Group, Boston University Institute for Astrophysical Research. Available online: `https://www.bu.edu/blazars/research.html`.

3.3 Synchrotron self-absorption and the core-shift effect

The early model of Blandford & Königl (1979) has been successfully used to explain most of the AGN observations at several bands and spatial resolutions, from the radio to γ-rays (e.g., Begelman et al., 1984; Maraschi et al., 1992). One of the main successes of this model in the radio band was the prediction of the apparent shift along the length of the jet of the position of the core with frequency. This shift takes place due to the presence of synchrotron self-absorption (SSA, Pacholczyk, 1970). The "core" of the jet at a given frequency is the most compact feature, commonly related to the surface at which the optical depth becomes $\tau = 1$ (photosphere) in the continuous jet.

Here we present some of the basic equations of synchrotron self-absorption. We assume that the electron energy distribution is described by a power law of the form

$$N(E) \propto E^{-s} \tag{3.1}$$

where s is the particle energy spectral index. The equation for the specific intensity of the synchrotron radiation at the frequency ν, I_ν, can be written as

$$I_\nu = \frac{\varepsilon_\nu}{\kappa_\nu}\left(1 - e^{-\kappa_\nu \tau}\right) \tag{3.2}$$

where ε_ν is the synchrotron emissivity, κ_ν is the absorption coefficient, and τ is the line-of-sight optical depth through the source. For a plasma with electron self-absorption, the spectral distribution of emission can be expressed as (Pacholczyk, 1970):

$$I_\nu \propto \left(\frac{\nu}{\nu_1}\right)\left[1 - \exp\left(\frac{\nu}{\nu_1}\right)^{\alpha_0 - \alpha_t}\right] \tag{3.3}$$

where ν_1 is the frequency at which the optical depth $\tau = 1$, α_t is the *optically thick* spectral index ($\alpha_t = 5/2$ for a homogenous source), and $\alpha_0 < 0$ is *the optically thin* spectral index (with spectral index defined by $S \propto \nu^\alpha$). The optically thin spectral index is related to the spectral index, s, by the following relation:

$$\alpha_0 = -\frac{(s-1)}{2} \tag{3.4}$$

Using the transformation from intensities to flux densities, Equation 3.3 can be expressed in terms of the observed turnover flux-density, S_m, and turnover frequency, ν_m (Türler et al., 1999):

$$S_\nu \approx S_m \left(\frac{\nu}{\nu_m}\right)^{\alpha_t} \frac{1-\exp\left(-\tau_m(\nu/\nu_m)^{\alpha_0-\alpha_t}\right)}{1-\exp(-\tau_m)} \tag{3.5}$$

where $\tau_m = \frac{3}{2}\left(\sqrt{1-\frac{8\alpha_0}{3\alpha_t}}-1\right)$ is the optical depth at the turnover. Depending on the value of ν/ν_m, Equation 3.5 describes an optically thick ($\nu < \nu_m$) or optically thin ($\nu > \nu_m$) spectrum with their characteristic shapes $S_\nu \propto \nu^{5/2}$ and $S_\nu \propto \nu^{-(s-1)/2}$, respectively.

Once the turnover frequency, ν_m, and the turnover flux-density, S_m, are obtained, estimates for the magnetic field, B, and the particle density, N_e, (e.g., Marscher, 1987) can be derived. The magnetic field and particle density decrease with r (where r is the distance from the central SMBH along the jet), and can be approximated as:

$$B(r) \propto r^{-m}. \tag{3.6}$$

$$N_e(r) \propto r^{-n} \tag{3.7}$$

with m and n positive indices. Assuming that the observed VLBI core is identical to the $\tau = 1$ surface, Lobanov (1998b) derives the observed position of the core, r_c, as:

$$r_c \propto \nu^{-1/k_r} \tag{3.8}$$

where the coefficient $k_r = [(3-2\alpha_0)m + 2n - 2]/(5-2\alpha_0)$. Assuming that the jet is conical (constant opening angle), freely expanding (with constant velocity), and there is an *equipartition* between the (non-thermal) particle and magnetic field energy densities, then the coefficient $k_r = 1$, the magnetic field $B \propto r^{-1}$ ($m = 1$), the particle density $N_e \propto r^{-2}$ ($n = 2$), and the position of the core $r_c \propto \nu^{-1}$. However, if jet flow speed and/or its opening angle are changing along the jet, other combinations of k_r, m, and n are possible, so that we could expect a different dependence of r_c.

When the core at each frequency corresponds to the surface where the optical depth for synchrotron self-absorption becomes unity (i.e., the $\tau = 1$ surface), the position of the radio core moves towards the central engine with increasing frequency (e.g., Blandford & Königl, 1979; Königl, 1981; Lobanov, 1998b). This effect is known as the *core-shift effect* (see Figure 3.4).

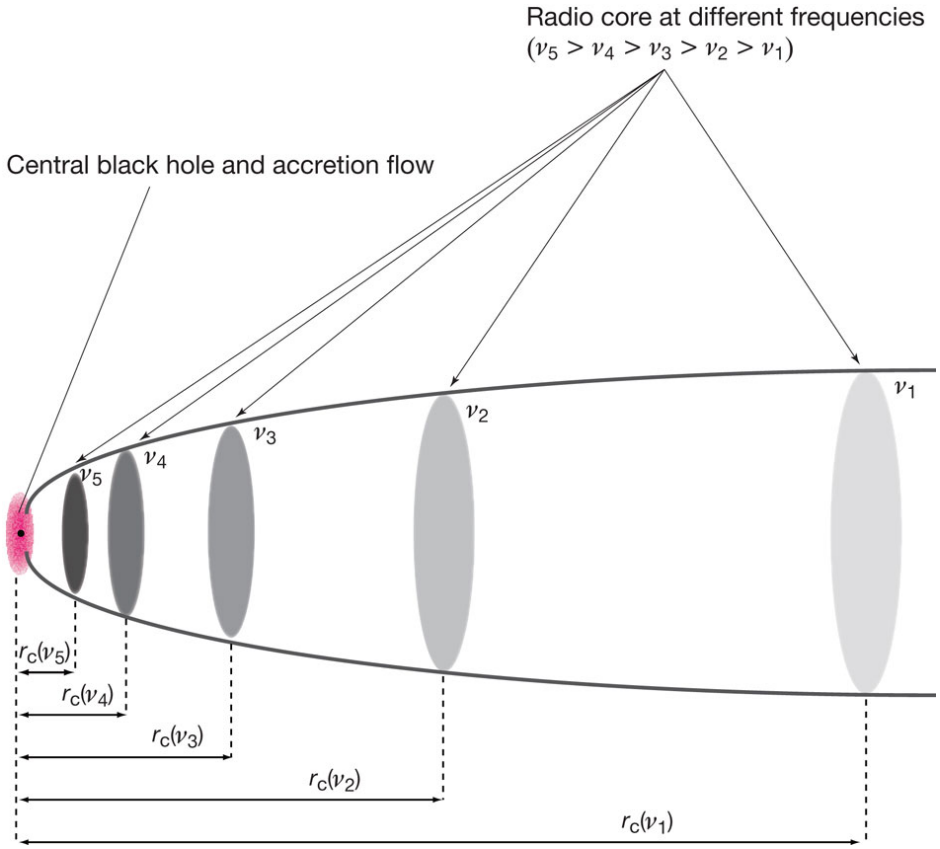

Figure 3.4: Schematic diagram explaining the radio core-shift of a jet. The diagram illustrates the core-shift of a jet generated from the central black hole (the black dot) surrounded by the accretion flow (represented as a magenta ellipse), with the horizontal axis showing a distance from the black hole (r_c). The cores of a jet, the bright surfaces of optical depths being unity, are indicated as grey ellipses at each frequency; darker colours indicate higher frequencies. The optical depth τ_{ssa} for the synchrotron self-absorption is a function of the radio-emitting electron number density N_e, the magnetic field strength B and the observing frequency ν. Because N_e and B have a radial profile in the jet, the radial position on the surface at which τ_{ssa} becomes unity shifts as a function of frequency. If we assume that N_e and B have power-law profiles described as $N_e \propto r^{-n}$ and $B \propto r^{-m}$ (n and m positive), the frequency dependence of the core position results in $r_c \propto \nu^{-\alpha}$. Here $\alpha = 1/k_r$ is the positive power index described as a function of n and m (Blandford & Königl, 1979). According to the relation, the core shifts towards the upper stream with increasing frequencies and would converge on the location of the central black hole at an infinite frequency. Credit: Hada et al. (2011).

3.4 Importance and determination of the core-shift

The observational discovery of the core-shift effect was made by Marcaide & Shapiro (1984), where they reported a 0.7 mas shift between 2.3 and 8.4 GHz in 1038+528A by comparing their separations from a feature in the nearby quasar 1038+528B, which had a perpendicular structure and hence allowed for an unambiguous registration. Since then, simultaneous VLBI observations at several frequencies have been used to analyze the variations in the observed core positions with frequency. These studies allow the observed core position to be related to source-intrinsic parameters, such as the magnetic field and the particle density (e.g., Lobanov, 1998b; Hirotani, 2005; Kovalev et al., 2008; O'Sullivan & Gabuzda, 2009; Pushkarev et al., 2009). Based on the core-shift corrected maps, reliable spectral index maps can be produced that show the spectral slope between two adjacent frequencies (e.g., Marcaide & Shapiro, 1984).

The complete spectral information (i.e., turnover frequency, ν_m, turnover flux-density, S_m, and spectral index, α) can be extracted from multi-frequency VLBI maps by performing a spectral analysis. Such studies have been performed (e.g., Lobanov, 1998a; Savolainen et al., 2008), and yield the spatial distribution of the spectral values and source-intrinsic parameters, such as the particle density, N_e, and the magnetic field, B.

Investigation of the core shift effect is important to gain deeper understanding of the structure and physics in AGN jets. It may also provide information about the pressure, magnetic field, and density gradients in ambient medium surrounding VLBI-scale jets near the central engine of AGN (e.g., Lobanov, 1998b, 2007; Martí-Vidal et al., 2011; Fromm et al., 2013). The impact of the effect on the interpretation of current and future radio VLBI astrometric measurements has been discussed by, e.g., Porcas (2009); Charlot (2010); Rioja et al. (2015).

Distant AGN, like quasars and BL Lacs, are currently used as position references in the definition of astronomical inertial frames, from radio (the International Celestial Reference Frame, ICRF Fey et al., 2004, 2015) to the optical (e.g., *Gaia*, Lindegren et al., 2012, 2016; Mignard et al., 2016). The consolidation of reference frames at different regions of the spectrum relies on a well-defined and time-stable chromaticity (i.e., frequency dependence) of the AGN emission. The core-shift is expected to introduce systematic offsets between the optical and radio positions of reference extragalactic sources (e.g., Kovalev et al., 2008, 2017; Petrov & Kovalev, 2017), which need to be taken into account for accurate radio-optical reference frame alignment in the era of modern space-based astrometric missions such as *Gaia*. It should also be taken into account when constructing VLBI spectral index (e.g., Kovalev et al., 2008) and Faraday rotation maps (e.g., Hovatta et al., 2012).

Therefore, precise measurements of the core shifts are necessary. One way to obtain core shifts is through phase-referencing VLBI (see Section 2.7.4). However, this is a complex and resource-intensive technique, and phase-referencing core shifts have been determined for only a few AGN, such as 1038+528 (Marcaide & Shapiro, 1984; Marcaide et al., 1994; Rioja & Porcas, 1998), 3C 395 (Lara et al., 1994), 4C 39.25 (Guirado et al., 1995), 3C 390.1 (Ros & Lobanov, 2001), M 81 (Bietenholz et al., 2004; Martí-Vidal et al., 2011), M 87 (Hada et al., 2011), and 3C 454.3 (Kutkin et al., 2014).

Another indirect method to measure core shifts is to align optically thin parts of an AGN jet at different frequencies (e.g., Croke & Gabuzda, 2008; Kovalev et al., 2008; O'Sullivan & Gabuzda, 2009; Sokolovsky et al., 2011; Fromm et al., 2015). However, this method requires simultaneous multi-frequency VLBI observations, which are likewise fairly resource intensive, and the need to have resolved jets with clear optically-thin hot spots. Besides, the method does not always yield unambiguous results. The limitations of these techniques are exacerbated by the fact that the core shift may well depend on the activity state of an AGN, and therefore be time-dependent, whereas at present only isolated core-shift measurements for individual AGN are available. In addition, the magnitude of the core shifts that can be detected is limited by the resolution of the VLBI observations used.

In the next chapter we study and compare three different methods to estimate the core-shift in several sources of the S5 Polar Cap Sample: 1) a slightly modified version of the SFPR technique presented in Section 2.7.4); 2) a global differential phase-delay astrometry (see Section 2.7.5); and 3) a combined global astrometry at U and Q bands.

Chapter 4

High-precision astrometry over frequencies and time

Insanity: doing the same thing over and over again and expecting different results.

Albert Einstein

The content presented in this chapter is essentially based on the publication appeared in the journal Astronomy & Astrophysics, 596, A27 (2016), and the manuscript *Core-shifts and proper-motion constraints in the S5 polar cap sample at the 15 and 43 GHz bands* submitted to Astronomy & Astrophysics on August 31, 2017.

Abstract

We have studied a complete radio sample of AGNs with the VLBI technique and for the first time successfully obtained high-precision phase-delay astrometry at Q band (43 GHz) from observations acquired in 2010. We have compared our astrometric results with those obtained at U band (15 GHz) from data collected in 2000. The differences in source separations among all the source pairs observed in common at the two epochs are compatible at the 1σ level between U and Q bands. The time interval between observations enables us to achieve precisions in the proper motions of the source cores of a few μas yr^{-1}. We study the source-position stability by analyzing the changes in the relative positions of fiducial source points (the jet cores) over a decade. We find motions of $0.1-0.9$ mas among close-by sources between the two epochs, which imply drifts in the jet cores of approximately a few tens of μas yr^{-1}. These results have implications for the standard AGN jet model (where the core locations are supposed to be stable in time). With the benefit of quasi-simultaneous U/Q band observations in 2010, we have made spectral-index maps and studied chromatic effects (i.e., core-shift) at the radio source cores with three different methods. The magnitudes of the core-shifts are of the same order for all methods, although some discrepancies arise in the core-shift orientations. In some cases, these discrepancies are due to insufficient information for the method to be applied. In others, the discrepancies reflect assumptions of the methods and could be explained by curvatures in the jets and/or departures from conical jets.

4.1 Introduction

Supermassive black holes are thought to be the engines of AGN and enormous relativistic jets may be powered by them. These jets show very strong and compact radio emission. The "core" of the jet is the most compact feature, commonly related to the surface at which the optical depth becomes $\tau \approx 1$. Due to opacity and synchrotron self-absorption (SSA) effects, the position of the core, often the position of the peak intensity (i.e., the $\tau \approx 1$ surface) depends on the observing frequency (e.g., Blandford & Königl, 1979; Königl, 1981; Lobanov, 1998b). Since the re-absorption of synchrotron radiation is more efficient at low frequencies, the peak will appear further downstream along the jet axis as the observing frequency decreases (see Section 3.3). Detailed studies of the core-shift in the astrometric catalogues may provide essential information for different aspects of astronomy; from geodesy and astrometry (i.e., to determine and remove the core-shift contribution in the alignment of the sources at different radio frequencies) to AGN astrophysics (understand how the jets form and propagate).

Several methods for measuring the core-shift have been proposed heretofore (see Section 3.4). For example, Rioja & Dodson (2011) presented a source-frequency phase-referencing (SFPR) method that makes possible to perform an intra-source dual-frequency calibration which is particularly convenient at high frequencies. Croke & Gabuzda (2008) developed a program to determine the shift between two VLBI images based on a cross-correlation analysis of the images, making use of all optically thin regions in the source structure. Kovalev et al. (2008) measured the core-shift of 29 compact extragalactic radio sources by model-fitting the source structure with two-dimensional Gaussian components, and referencing the core position to optically thin jet features, whose positions are expected to be frequency-independent.

However, the sky location of AGN cores may not only depend on frequency, but also on time. If the opacity in the jet changes (owing to variability in the particle density and/or the magnetic-field structure) or the jet changes its orientation (e.g., owing to precession), the position of the core at any given frequency (and also the core-shift) evolves. This kind of an evolution of core positions encode information about the changing physical conditions at the innermost regions of the AGN jets, and also map into time-dependent misalignments among AGN-based reference frames at different frequencies.

To date, a large fraction of geodetic and astrometric VLBI observations rely on the group-delay observable. The group-delay astrometry does not usually take the effect of source structures into consideration, whose time variability (and frequency dependence) can introduce astrometric biases of even several times the nominal astrometric group-delay precision (Moór et al., 2011). Restricting the observations to very compact jet structures (i.e., jets with low "structure indices" Charlot, 1990) and/or to jets with smooth profiles in a particle-field energy equipartition, help us to minimize the frequency (and time) astrometry variations in the definition of the reference frames with group-delay astrometry (Porcas, 2009). But, in any case, the use of phase delays instead of group delays provides a better solution for accounting for the source structure in the astrometry. Moreover, the phase delays are more precise than the group delays by up to several orders of magnitude (see, e.g., Martí-Vidal et al., 2008; Martí-Vidal, 2008, for a deeper discussion).

The study of core-shifts (as well as absolute proper motions) in a complete radio sample were the main science drivers of a large VLBI astrometry programme (BM300) of observations of the complete S5 polar cap sample (Kühr et al., 1981; Eckart et al., 1986). The main goals of this campaign were the study of the frequency dependence and time stability of the jet structures (especially, the jet cores), as well as the characterization of the absolute kinematics of the optically-thin jet components of all sources.

The S5 polar cap sample consists of 13 radio-loud AGN that are located at high declinations (circumpolar for the VLBA). Over two decades, we carried out a set of VLBA observations of the complete S5 polar cap sample, in phase-referencing mode, covering a frequency range from 1.4 to 43 GHz. Partial results for some of those observations (study of the source structures) have already been reported at 8.4 GHz (Ros et al., 2001) and 15 GHz (Pérez-Torres et al., 2004), as well as astrometry results for subsets of the sample (Ros et al., 1999; Guirado et al., 2000; Pérez-Torres et al., 2000; Guirado et al., 2004; Jimenez-Monferrer et al., 2007). The first global astrometry analysis (where the relative positions among source pairs at 15.4 GHz could be determined with an unprecedented accuracy) was published in Martí-Vidal et al. (2008). In year 2010, we used, for the first time in this astrometry project, the fast-frequency-switching (FFS, Middelberg, 2005) observing capabilities of the VLBA. The observations were carried out at U and Q bands, quasi-simultaneously. This approach enables us to perform one single (i.e., global and self-consistent) fit of the source positions at both frequencies, and thus, to obtain the shift of the positions between the low and the high frequencies (i.e, the core-shift).

Here we present a global differential phase-delay astrometry at 14.4 and 43.1 GHz. The analysis performed at 14.4 GHz is similar to that performed in (Martí-Vidal et al., 2008) but with higher quality observations. Instead, the analysis performed at 43.1 GHz marks likely the limit of application of this technique with current instrumentation. This is due to the short ambiguities of the phase delays, compared to the atmospheric variability at timescales of the order of the slewing times of the antennas. The power of the phase-delay astrometry analysis relies on the possibility of a simultaneous fit of all the parameters that define both the geometric and the instrumental components of the interferometer, such as clock drifts, position of the antennas, and tropospheric/ionospheric delays, together with the source positions. All these parameters are optimized self-consistently in the analysis, as opposed to other non-parametric approaches (e.g., phase referencing), where the instrumental and atmospheric effects are not properly parameterized and optimally accounted for all sources, but rather estimated and interpolated from one calibrator to a target (see Sections 2.7.4 and 2.7.5).

In addition to this global astrometry analysis, we study and compare three different methods to estimate the core-shift in several sources of this sample: 1) the global differenced phase-delay astrometry at 14.4 GHz, directly compared to the global astrometry at 43.1 GHz; a combined (i.e., simultaneous) global astrometry at the two bands; and 3) a slightly modified version of the SFPR technique. As a complementary study, we also compare the core-shift directions (for the subset of sources with successful detections) with the orientation of the core emission at the two frequencies, as a study of the jet geometry at (sub)-parsec scales.

In the next section, we describe the VLBA observations, the calibration strategy and the analysis of the data. In Section 4.3, we show the maps of the sources at both frequencies. In Section 4.4, we present the results of the core-shifts obtained with the SFPR technique. The details of our astrometric analysis as well as the phase-connection at 14.4 and 43.1 GHz are explained in Section 4.5. In Section 4.6, we present the results of the global astrometry. An analysis of the core structures of the sources is presented in Section 4.7. In Section 4.8, we show spectral-index images for a subset of sources. In Section 4.9, we summarize our conclusions.

4.2 Observations and data calibration

The VLBA observations were performed in 2010 December 18, starting at 01:26 (UT) with a duration of about 24 hours. The recording rate was set to 256 Mbps and the observations were in single-polarization mode (only the left circular-hand polarization, LCP, was registered). We covered a total bandwidth of 64 MHz, divided into eight intermediate frequency bands (IFs). We used the FFS capabilities of the VLBA frontends, which enabled us to change among different observing bands in approximately half a minute, without loss of coherence among band switches (Middelberg, 2005). Our lowest reference frequency was 14.35099 GHz (hereafter 14.4 GHz or U band) and the highest reference frequency was 43.10099 GHz (hereafter 43.1 GHz or Q band). Thus, the higher frequency was very nearly three times (3.003346) the lowest frequency. Such a frequency configuration makes it possible to perform an intra-source dual-frequency calibration (SFPR, Rioja & Dodson, 2011), and thus help us to determine robustly the core-shifts of all sources between these two observing frequencies.

In Table 4.1, we list all the sources of the S5 polar cap sample, together with the short aliases used in this work. We take the positions reported in Martí-Vidal et al. (2008) (i.e., those estimated at 15 GHz in year 2000) as the initial positions for the fit of the 2010 observations. Hence, any shift observed from the observations reported here can be directly related to a physical shift in the source positions between June 2000 (i.e., the epoch reported in Martí-Vidal et al. (2008)) and December 2010 (i.e., our new observations).

Table 4.1: Individual sources observed. Positions are referred to June 2000 at U band (Martí-Vidal et al., 2008). The last column indicates which sources had enough GFF detections at Q band for our phase-delay analysis.

Source name	Alias	Right Ascension J2000	Declination J2000	Q Fringe
B0016+731	00	$00^h\ 19^m\ 45.7862^s$	73° 27' 30.0167"	✓
B0153+744	01	$01^h\ 57^m\ 34.9649^s$	74° 42' 43.2289"	
B0212+735	02	$02^h\ 17^m\ 30.8132^s$	73° 49' 32.6213"	✓
B0454+844	04	$05^h\ 08^m\ 42.3635^s$	84° 32' 04.5440"	
B0615+820	06	$06^h\ 26^m\ 03.0062^s$	82° 02' 25.5678"	
B0716+714	07	$07^h\ 21^m\ 53.4485^s$	71° 20' 36.3630"	✓
B0836+710	08	$08^h\ 41^m\ 24.3653^s$	70° 53' 42.1724"	✓
B1039+811	10	$10^h\ 44^m\ 23.0628^s$	80° 54' 39.4428"	✓
B1150+812	11	$11^h\ 53^m\ 12.4991^s$	80° 58' 29.1536"	✓
B1749+701	17	$17^h\ 48^m\ 32.8403^s$	70° 05' 50.7687"	✓
B1803+784	18	$18^h\ 00^m\ 45.6840^s$	78° 28' 04.0183"	✓
B1928+738	19	$19^h\ 27^m\ 48.4952^s$	73° 58' 01.5698"	✓
B2007+777	20	$20^h\ 05^m\ 30.9987^s$	77° 52' 43.2471"	✓

The observations were arranged in duty cycles. Each duty cycle covered a subset of two to four close-by sources (with integration times between 30 and 60 seconds in each source pointing), in a similar way as the duty cycles described in Martí-Vidal et al. (2008). The duty cycles were designed to maximize the antenna elevations to optimize the quality of the differential phase delays. We show in Figure 4.1 the time distribution of all the observations. The frequency-switching changes were applied in two types of duty cycles, which were alternated every four iterations. In the first type of cycle (optimized for the frequency-switching calibration), half of the switchings were applied while the antennas were slewing among sources. If A_L and A_H are observations of source A at 14.4 GHz and 43.1 GHz, respectively, the duty cycles were arranged as

$$A_L - B_H - B_L - A_H - A_L - B_H - B_L ...$$

This approach saves some time due to switching. In the second type of duty cycle, observations of different sources at the highest frequencies were put close in time:

$$A_L - A_H - B_H - B_L - B_H - A_H - A_L ...$$

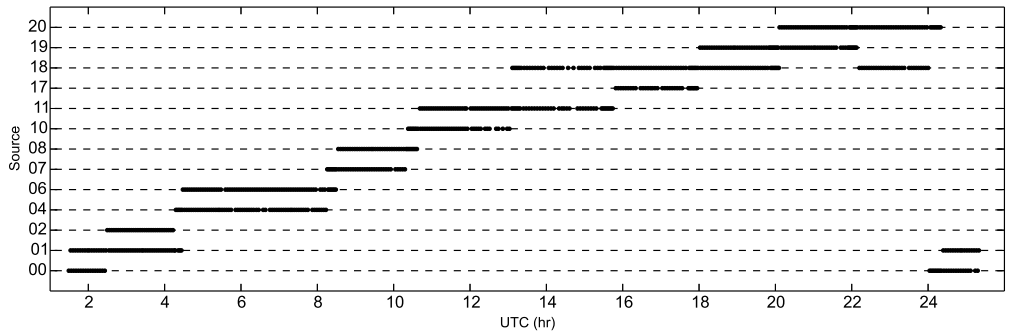

Figure 4.1: Time distribution of our observations in year 2010. Sources under similar time windows were observed in common duty cycles. The pair 18−19 was not observed in year 2000.

This approach minimizes the time lag among consecutive observations of different sources at the highest frequency band (43.1 GHz), where the atmospheric effects are more critical for the phase connection of the differential phase delays. Due to the dual-frequency observations, the duty cycles were, on average, longer in time than those of the epoch of year 2000. Hence, we restricted our duty cycles to close-by sources, to minimize the slewing time and ensure a successful phase connection. The source pairs observed in the duty cycles that have been used in this analysis are listed in Table 4.2.

The data were correlated at the NRAO headquarters (Socorro), using the NRAO version of the DiFX software correlator (Deller et al., 2007). A total of 128 spectral channels per visibility were generated (16 channels per IF).

4.2.1 Fringe search

The calibration was performed using the Astronomical Image Processing System (AIPS) software[1] by NRAO, using standard procedures. The dispersive (i.e., ionospheric) delay contribution was removed with the AIPS task TECOR, using GPS satellite data. The effect of source structures at each band was removed by obtaining CLEAN hybrid images of all sources and using the resulting source models in the computation of the model phases, prior to the final fringe search. The positions of the peak intensities of all the sources at each band were used as the source phase centers (i.e., the fiducial reference points for the astrometry). For the phase, delay, and phase-rate calibration, we applied the Global Fringe Fitting (GFF) algorithm (e.g., Alef & Porcas, 1986) to all data at both bands. We only detected fringes at Q band for a subset of all sources observed (see Table 4.1).

[1] `http://www.aips.nrao.edu`

Table 4.2: Source pairs observed. The separations, used as *a priori* in this work, are those determined in June 2000 (Martí-Vidal et al., 2008) using source 07 as reference. The last two columns indicate the source pairs available at U and Q bands in 2010.

Pair	Separation (deg)	U band	Q band
01 - 00	6.7707315679	✓	-
01 - 02	1.6149364850	✓	-
04 - 06	3.3327854279	✓	-
08 - 07	6.4191401883	✓	✓
11 - 10	2.6993766419	✓	✓
11 - 18	14.8392077764	✓	✓
18 - 17	8.4082929389	✓	✓
18 - 20	6.3423054016	✓	✓
19 - 20	4.5218913640	✓	✓

Our phase-delay analysis approach (Section 4.6.2) requires detection of fringes at both bands in consecutive scans, and a sufficiently long integration time, for a robust estimate of the inter-frequency (core-shift) astrometry. Hence, we could only perform our core-shift analysis on a subset of the S5 polar cap sample (right column in Table 4.1).

The total (phase and group) delays were exported from AIPS for their later analysis with our astrometry software, the University-of-Valencia Precision Astrometry Package (UVPAP, Martí-Vidal, 2008; Martí-Vidal et al., 2008). The source pairs available to perform the global differenced astrometry at U/Q bands are listed in Table 4.2. Notice that, even though we have observations of sources 00 and 02 at Q band (Table 4.1), we could not compute their differential phase-delays due to the lack of detections of source 01 at Q band (observed in the same duty cycle).

4.3 Imaging and deconvolution

4.3.1 Maps at U band

We show the source structures of all sources of the S5 polar cap sample at 14.4 GHz in Figure 4.2. The structures in year 2000 (i.e., the observations reported in Martí-Vidal et al. (2008)) are shown in blue contours, and the structures recovered in 2010 in red contours. All sources have been shifted to set their intensity peaks (i.e., the phase centers in our astrometry analysis) at the coordinate origin of each image. The ten contours shown are spaced logarithmically, from 0.75% to 99% of the source intensity peaks. The restoring beams have a full width at half maximum (FWHM) of 1×1 mas in all cases (this is close to the typical major axis of the restoring beams in all sources, using natural weighting of the observed visibilities).

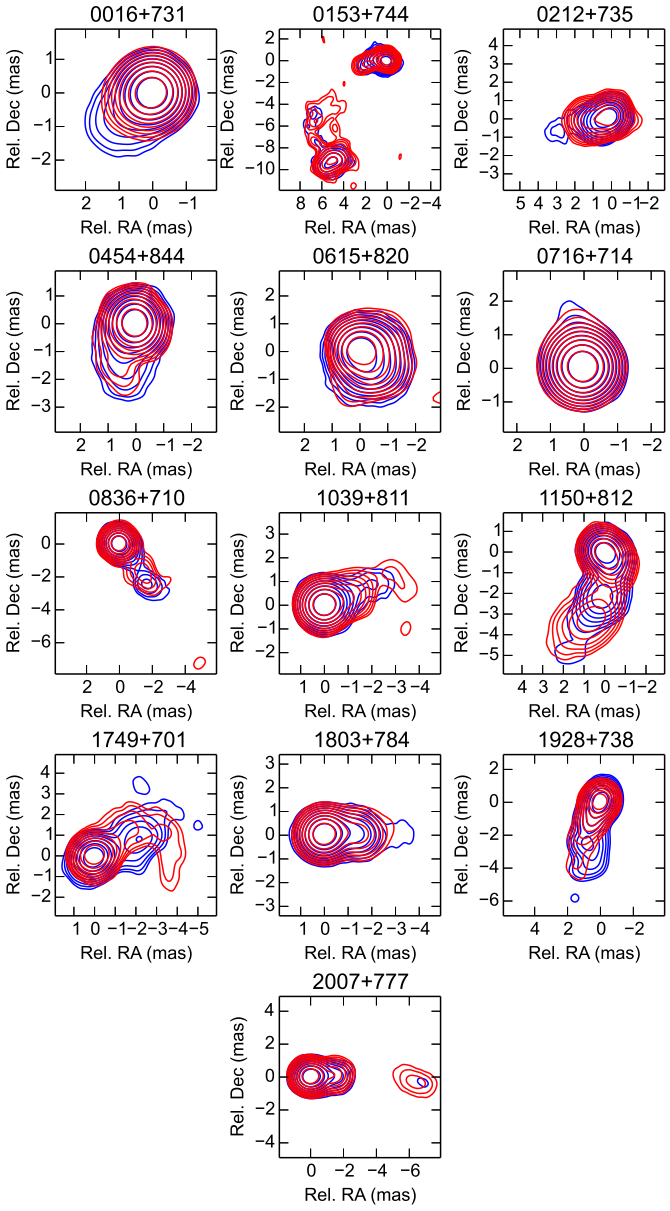

Figure 4.2: Images of the S5 polar cap sample sources in year 2000 (at 15 GHz, in blue contours) and in year 2010 (at 14.4 GHz, in red contours). The sources have been shifted to set their intensity peaks at the coordinate origin. The contours are spaced logarithmically from 0.75% to 99% of the source peaks. The restoring beams have a FWHM of 1×1 mas.

4.3.2 Maps at Q band

In Figure 4.3, we show the structures of all sources at 43.1 GHz, as observed in year 2010. Similar to Figure 4.2, all images in Figure 4.3 have been shifted to have their intensity peaks at the coordinate origin of each image. The ten contours shown are spaced logarithmically, from 0.5% to 99% of the source intensity peaks (for sources 00, 07, 08, 10 and 18), from 2% to 99% (for sources 02, 06, 11 and 17) and from 10% to 99% (for sources 01, 04 and 20). The restoring beam in all cases is set to 0.3×0.3 mas of FWHM. The intensity peaks of all the maps at 14.4 GHz and 43.1 GHz are given in Table 4.3.

From all images shown, there are a few cases that deserve additional comments. The jet extension of source 04 (0454+844) at 14.4 GHz is seen towards the south (see Figure 4.2), while the jet extension at 43.1 GHz (see Figure 4.3) is seen apparently the other way around, with the brightest feature (i.e., the core) at south. The northern extension at 43.1 GHz could be due, for instance, to a jet feature (hot spot) propagating downstream from the jet base. If the feature is approaching the 43.1 GHz core (but it is still in the self-absorbed region), it could be seen, morphologically, as a false jet-like extension towards the north (or as a false counter-jet in the direction to the jet base). The core-shift of 04 (Section 4.4) confirms this interpretation.

Another source worth mentioning is 06 (0615+820). At 43.1 GHz, it shows two cores, one at northeast (NE) and the other at southwest (SW). The NE core shows a jet extension in the east-west direction, whereas the SW core seems unresolved. This geometry is quite different of what it is guessed from the 14.4 GHz image alone (Figure 4.2), where the two cores are blended in an apparent jet-like structure in the north-south direction. In Section 4.8, we discuss on the frequency-dependent brightness distribution of this source.

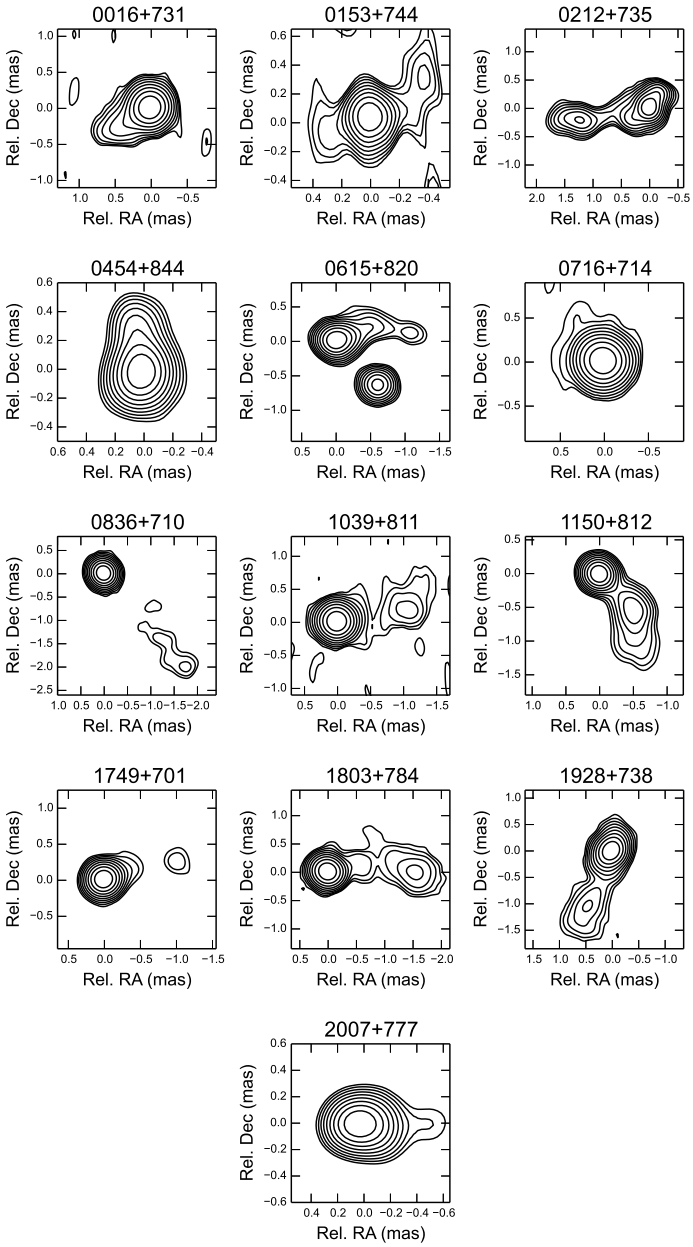

Figure 4.3: Images of the S5 polar cap sample sources at 43.1 GHz. The sources have been shifted to have their intensity peaks at the coordinate origins. The contours are spaced logarithmically, from 0.5% to 99% of the source intensity peaks (for sources 00, 07, 08, 10, 17, and 18), from 2% to 99% (for sources 02, 06, 11, 19, and 20), and from 10% to 99% (for sources 01 and 04). The restoring beams are 0.3×0.3 mas FWHM.

4.4 Source-frequency phase referencing and core-shifts

The observations reported in this work were performed using the FFS capabilities of the VLBA. These capabilities enabled us to make a phase transfer between 14.4 GHz and 43.1 GHz using an adaptation of the SFPR method described in Rioja & Dodson (2011) (see also Rioja et al., 2014).

The phase-transfer calibration was performed using an in-house developed software, which makes use of the scriptable `ParselTongue` interface to AIPS (Kettenis et al., 2006). Once we accounted for the source structures in the fringe fitting, the remaining antenna gains at our two observing frequencies were only affected by atmospheric, instrumental and chromatic effects (e.g., core-shifts) in the source structure. The bulk of the ionospheric contribution was removed using the AIPS task TECOR. The non-dispersive contributions were removed by scaling the phase-like antenna gains at 14.4 GHz by the frequency ratio ($43.1/14.4 \sim 3$), to calibrate the 43.1 GHz data.

Since the observing times at 14.4 GHz and 43.1 GHz do not coincide (there is a difference between consecutive scans of at least 30 seconds, which is the time needed by the FFS system to switch between observing bands), we had to interpolate the gains at 14.4 GHz to the observing times at 43.1 GHz, using the rate integral at 14.4 GHz and accounting for the phase ambiguities among the consecutive 14.4 GHz observations. For each scan, the instrumental and ionospheric offsets between the scaled 14.4 GHz phases and the 43.1 GHz phases were subtracted by phase-referencing from sources observed in common duty cycles (see Figure 4.1).

After applying the SFPR calibration, we measured the position shifts of the intensity peaks in all the resulting images (shown in Figure 4.4). These shifts contain the core-shift of the target sources plus the core-shifts of their respective phase-referencing calibrators (Table 4.3). In order to decouple the shifts of the calibrators from those of their targets, we re-referenced the shifts in all the SFPR images to common points in the sky: the compact and optically-thin jet components in sources 10, 11, 18, 19, and 20 (shown in Figure 4.5).

In Figure 4.4, we also show the expected SFPR peak positions for the pairs 19-20, 19-18 and 18-20, by assuming that the compact optically-thin jet features at 14.4 and 43.1 GHz are co-spatial. These results cannot be directly compared to those in Rioja et al. (2015), since the spatial resolutions are very different and jet-blending effects introduce additional shifts of the source peaks at each frequency.

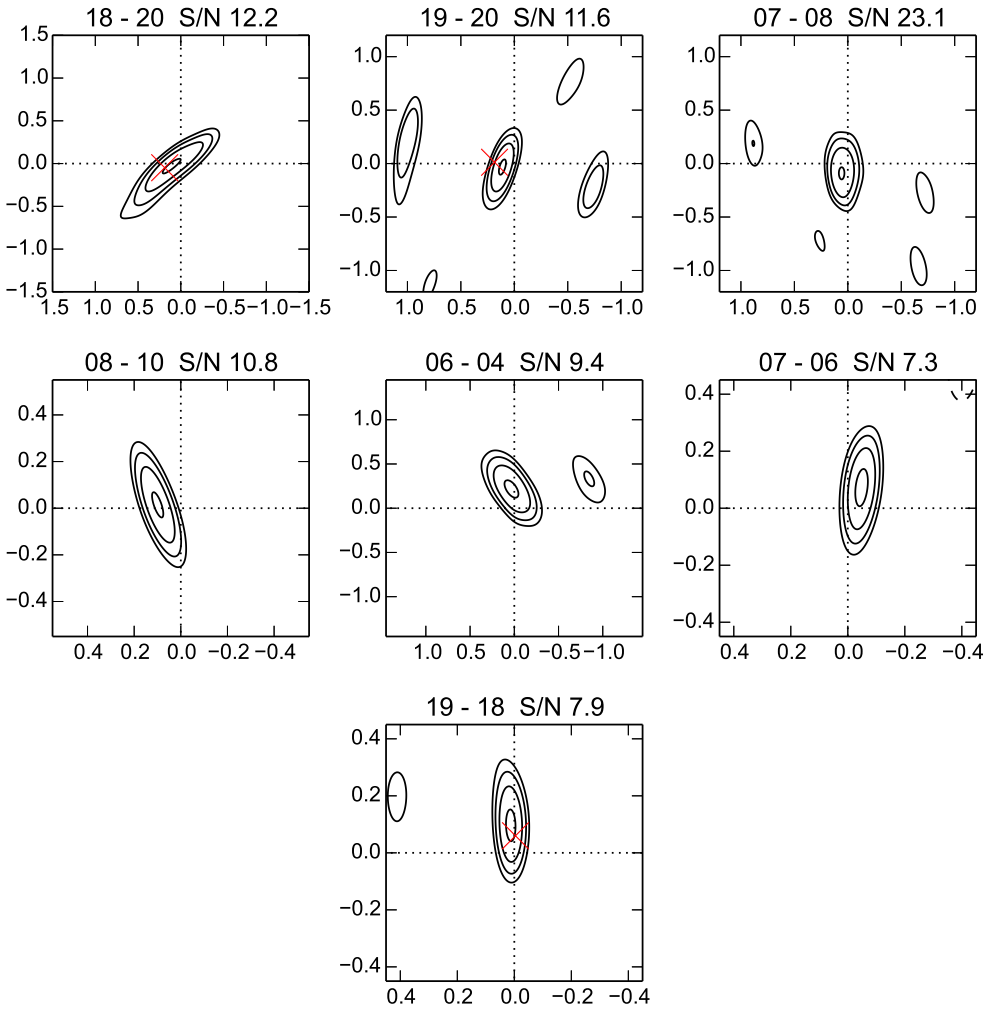

Figure 4.4: SFPR images at 43 GHz. The axes, given in mas, correspond to the RA and Dec offsets with respect to the peaks at 14.4 GHz. Contours are logarithmically spaced between 5σ noise and the source peak. The label XX-YY indicates source YY phase-referenced to the calibrator XX. The red crosses indicate the expected peak positions of sources 18, 19 and 20, assuming that their compact optically-thin jet components (as well as those of their calibrators) are co-spatial at 14.4 and 43.1 GHz.

The strategy of using compact optically-thin features as an astrometry reference has been applied in previous core-shift studies (e.g., Kovalev et al., 2008; Fromm et al., 2013). We notice that the use of more extended optically-thin emission (e.g., the jet extension in source 08) may bias the core-shift, due to spectral gradients accross the jet structure.

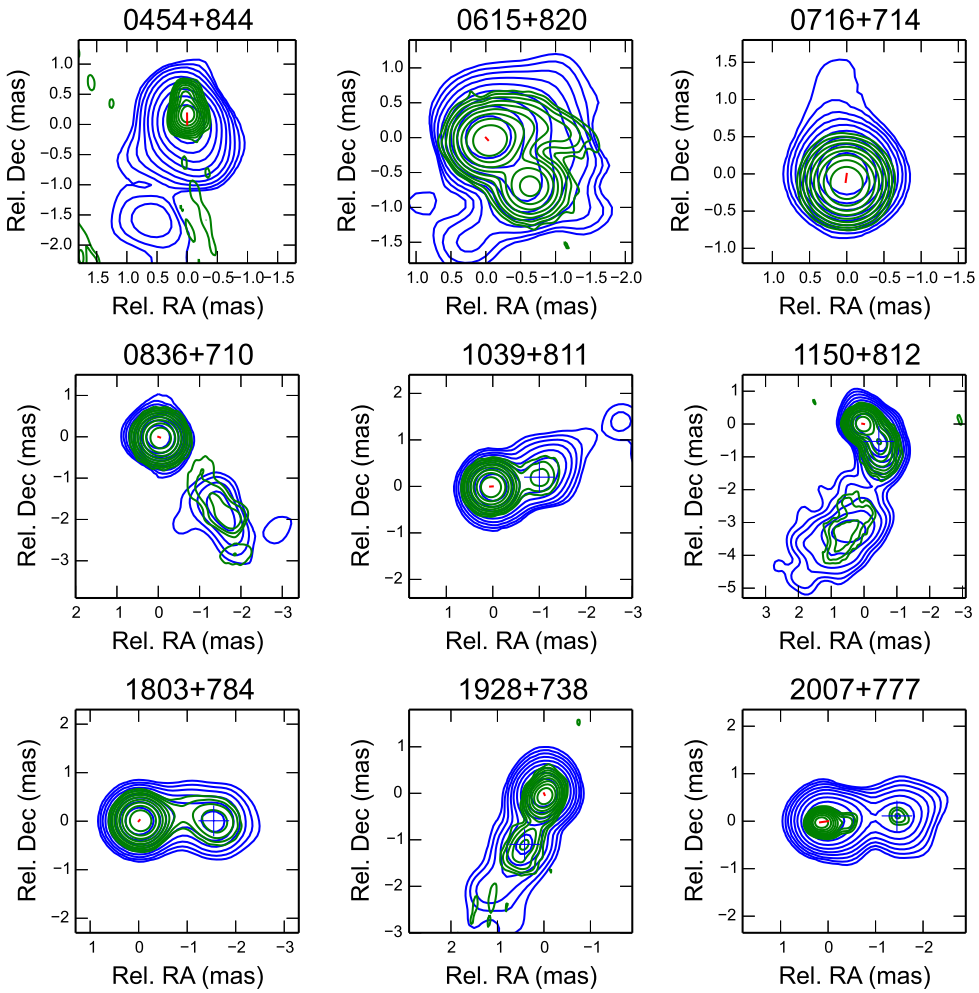

Figure 4.5: Sources with a successful phase-transfer calibration. Contours at 14.4 GHz are shown in blue; at 43.1 GHz, in green. Notice the short red lines close to the image peaks, which indicate the direction and magnitude of the core shifts. The FWHM of the restoring beam in all images is 0.6×0.6 mas. The optically-thin components used as astrometry references in the SFPR analysis (Section 4.4) are indicated with crosses. The uncertainties in the core shifts (Table 4.3) are not shown in this figure for clarity.

In Figure 4.6, we show the difference between the overall Pie Town phase gains at 14.4 GHz (scaled up by a factor of three, to convert them into 43.1 GHz gains, and interpolated in time) and the overall phase gains computed directly from the 43.1 GHz fringes. We notice that the differences in the phase gains for most of the sources are not random. This is indicative of a successful phase-transfer calibration. However, there were few successful gain solutions at 43.1 GHz for source 01, which were not sufficient to perform the SFPR calibration among sources 00, 01, and 02. In addition, we only considered successful SFPR detections those with an image dynamic range S/N > 5. As a consequence, the core-shift of sources 11 and 17 could not be re-referenced to any other source of the sample.

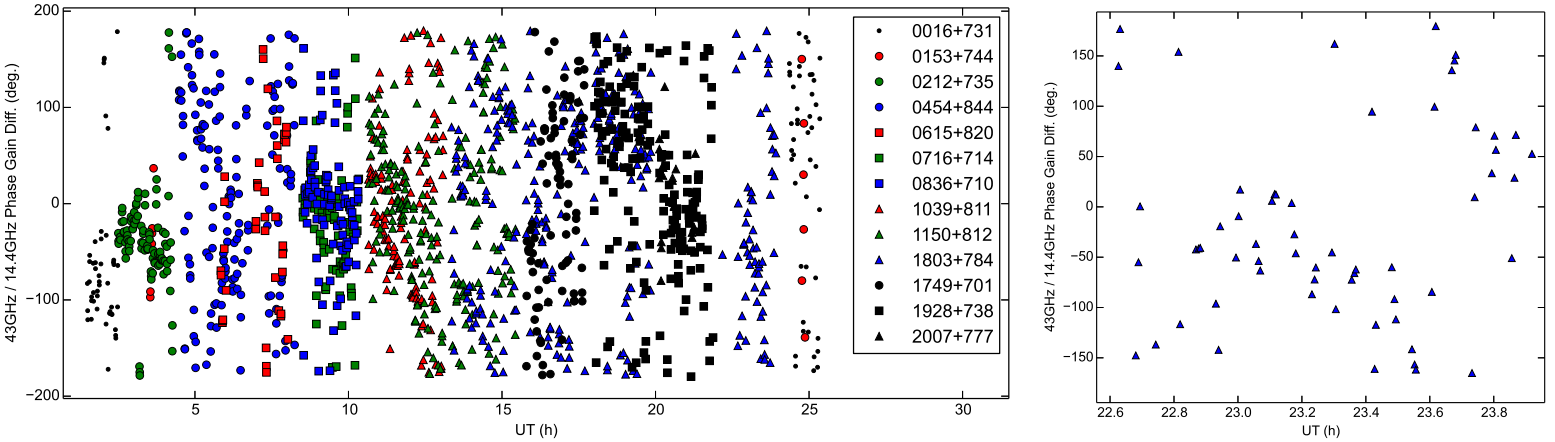

Figure 4.6: Left, difference between the phase gains at 43.1 GHz and the –scaled up by a factor of three– phase gains at 14.4 GHz for the Pie Town antenna. The instrumental phase offset has been removed (see text). Hence, the differences among sources observed in common duty cycles encode information related to the core-shift of the sources between the two observing frequencies. Right, zoom for source $1803+784$.

Table 4.3: Results for individual sources: map peak intensities at the epochs 2000 (only 15 GHz) and 2010 (14.4 and 43.1 GHz) and shift of those peak intensities (usually associated to the cores, and hence called core-shifts) between 14.4 and 43.1 GHz at epoch 2010. All shifts are re-referenced to optically-thin jet components (see Figure 4.5). Source 06 is a special case (see text).

Source name	Alias	PR-Calib	Peak (2000) (Jy/beam)	Peaks (2010) (Jy/beam)		Core shift			Ref.
						RA	Dec	Module	
			15 GHz	14.4 GHz	43.1 GHz	(μas)	(μas)	(μas)	
B0016+731	00	–	0.73	0.98	0.53	–	–	–	–
B0153+744	01	–	0.19	0.08	0.01	–	–	–	–
B0212+735	02	–	1.69	1.69	0.48	–	–	–	–
B0454+844	04	06	0.17	0.17	0.07	2 ± 138	181 ± 74	226 ± 78	10
B0615+820	06	04, 07	0.27	0.38	0.14	-32 ± 95	-35 ± 43	100 ± 56	10
B0716+714	07	06, 08	1.02	2.04	1.62	14 ± 55	-108 ± 26	121 ± 30	10
B0836+710	08	07, 10	1.42	1.81	1.41	-44 ± 53	-16 ± 25	66 ± 35	10
B1039+811	10	08	0.75	0.50	0.44	57 ± 12	-4 ± 13	58 ± 12	10
B1150+812	11	–	0.55	0.43	0.16	54 ± 2	9 ± 2	55 ± 2	11
B1749+701	17	–	0.31	0.47	0.22	–	–	–	–
B1803+784	18	19, 20	1.79	1.70	0.84	-20 ± 4	24 ± 4	31 ± 3	18
B1928+738	19	18, 20	1.53	3.24	1.39	-15 ± 4	-36 ± 5	39 ± 5	19
B2007+777	20	18, 19	0.95	0.60	0.22	168 ± 8	-23 ± 9	170 ± 8	20

Notes: *PR-Calib* are the aliases of the sources used as SFPR calibrators for each source (see Section 4.4). *Core shift* is the shift between the intensity peaks of the images at different frequencies. We notice, though, that the intensity peak may not correspond to the true core of the AGN jet in some cases (see Section 4.8). Restoring beam of 0.6×0.6 mas at all frequencies have been used prior to finding the intensity peaks.The VLBI uncertainties in the absolute flux-density calibration are typically $5-10\%$. *Ref* is the source with an optically-thin jet feature used as a position reference for the core shift (see text).

4.5 Phase connection at U and Q bands

4.5.1 The *a priori* model

In order to perform the phase-connection at U band, the group delays at 14.4 GHz of all sources were used to derive good *a priori* models for the atmospheric non-dispersive delay and the drifts of the stations clocks. These models were then used to perform a preliminary connection of the (otherwise ambiguous) phase delays. The remaining unmodeled phase cycles were derived using an automatic phase-connection algorithm (Martí-Vidal et al., 2008).

The phase connection at 43.1 GHz is especially difficult, since the delay corresponding to one 2π phase cycle is so short (only ~ 23 ps) that very small unmodeled atmospheric effects can add several 2π cycles to the phase-delays between two consecutive observations of the same source. A parameterized interferometer model (with station-based clock drifts described by third-order polynomials and atmospheric delays described by piece-wise linear functions) was fitted to the group delays, which provided a prediction of the delay rates good enough to ensure the proper connection of the phase-delays between consecutive scans of the same source. Since the average time separation between observations is ~ 180 s and the phase cycle at 43.1 GHz is ~ 23 ps, the residual rates have to be lower than (23 ps/180 s) = 0.13 ps/s to ensure a good phase connection.

In Figure 4.7, we plot the distribution of the residual delay rates of our observations at Q band. Residual delay rates with absolute values higher than 0.13 ps/s in the distribution, most of them corresponding to the longest baselines and the weakest sources, are not negligible. The model phase delays were used to perform the connection of the observed phase delays. Remaining 2π cycles were found by applying the same automatic phase-connection algorithm as at U band. The few remaining (antenna-based) ambiguities, left after the connection process, were determined using the *smoothness criterion* described in Martí-Vidal et al. (2008).

4.5.2 Source-based clock offsets

The procedure used to estimate the source-based constant clock offsets (CCOs) for the first global high-precision differential astrometry at U band was described in Martí-Vidal et al. (2008). Basically, they applied an iterative process, where the CCOs were left as free parameters and they fixed (one at a time) the closest CCO to a complete 2π phase-delay cycle. They iterated this procedure until all the source-based CCOs were fixed to complete 2π phase-delay cycles.

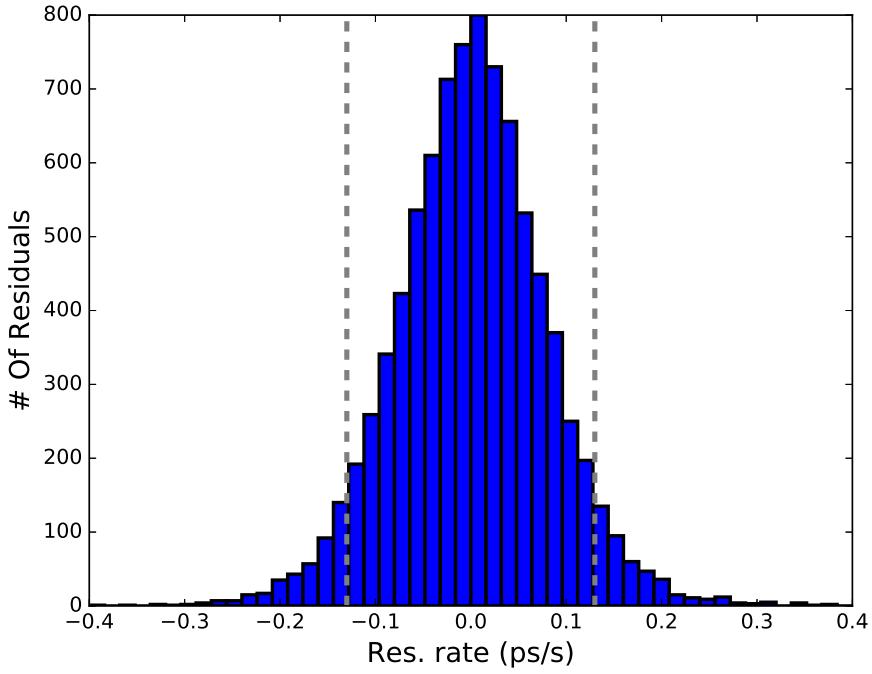

Figure 4.7: Distribution of the residual delay rates for all the baselines, sources, and scans of our observations. The dashed lines at 0.13 ps/s illustrate that most of the values are good enough to ensure the phase-delay connection at 43.1 GHz (see text).

In this thesis, we present another automated procedure, where the CCOs are fixed in the frame of a Monte Carlo analysis for the estimate of the astrometric uncertainties. The source-based CCOs, together with the tropospheric delays, antenna positions, and even the dispersive ionospheric delays, are allowed to vary. From all these random deviations of the model parameters, we derive the posterior probability distributions of the source positions.

The phase-connections at U and Q bands were performed at distinct times and the *a priori* uncertainties selected for the tropospheric and ionospheric delays were slightly different. The nodes of the piece-wise linear functions of the tropospheric delays were randomly perturbed following Gaussian distributions of 0.2 ns (0.1 ns) variance for the U (Q) band. We selected the values from the weather conditions of the experiment, after we evaluated the delay variations of the wet and dry components of the troposphere along the full experiment. For the ionospheric delays, we applied random Gaussian perturbations in the TEC, of variance 0.1 (0.5) TECUs for the U (Q) band. We decided to use a 5$\times$ higher ionospheric

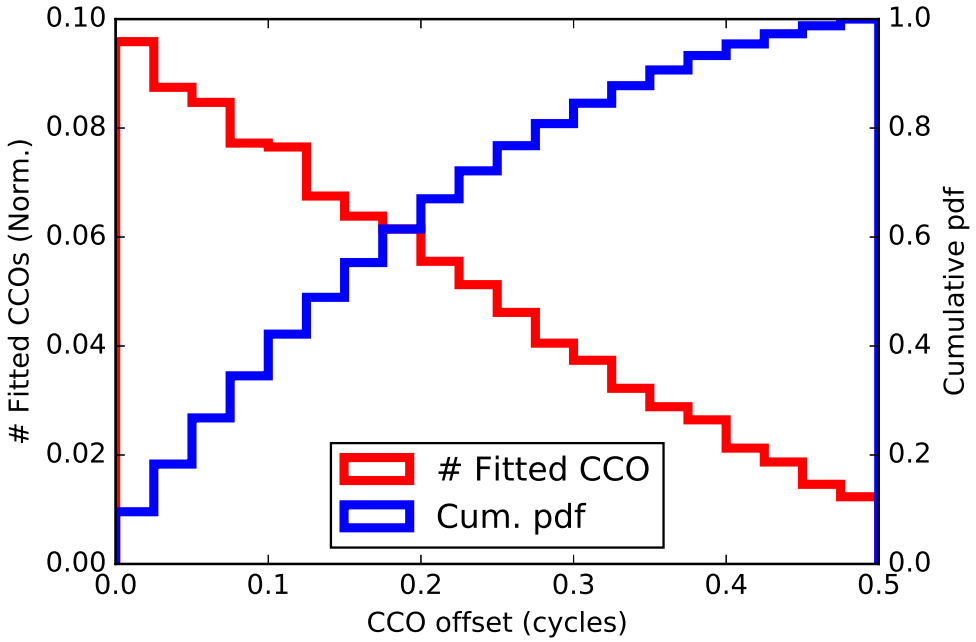

Figure 4.8: Normalized distribution of constant clock offset deviations from complete 2π phase-delay cycles at 43.1 GHz. The red line represents the fitted values while the blue line represents the cumulative probability distribution function. Notice the peak near zero in the red line. Notice as well in the blue line that half of the CCOs are within 0.15 cycles ($\sim$ 3.5 ps).

uncertainty at Q band after we evaluated that our results were not very much affected within that variance interval. Finally, for the antenna positions, we applied Gaussian perturbations of 1 cm variance (in each coordinate).

In Figure 4.8, we show the distribution of CCO deviations from complete 2π phase-delay cycles at Q band, acquired from the whole set of Monte Carlo iterations. We notice that the CCO probability distribution has a clear peak near integer number of 2π phase cycles, being minimum in the region around half 2π cycles. Such a CCO distribution is expected from a successful phase connection, since the difference in phase-delays between antennas for each source shall be, by construction, an integer number of 2π cycles. The fact that we recover such values (from a completely free fit of the CCO values) is a good indicative that the time evolution of the delays for the different sources (which can cover several 2π cycles across the scans) are coherent from source to source, and during the whole experiment.

4.6 Differential phase-delay astrometry at U and Q bands

With the phase-delay ambiguities properly corrected at both bands, we finally computed the differential phase-delays (i.e., differences among delays for sources observed in the same duty cycles). Typically, the inclusion of the differential delays in the astrometric analysis improves the precision by roughly an order of magnitude, when compared to an ordinary phase-referencing analysis. This is due to the many redundancies present in our multi-source duty-cycle scheduling, and to the superior quality of a parametric astrometry analysis (i.e., fitting delays and phases to a complete geodetic + astrometric model) when compared to ordinary phase-referencing astrometry (where the geodetic + atmospheric models cannot be optimized).

In Figure 4.9, we show the undifferenced and differenced phase delays at U band for two different baselines: Fort Davis to Pie Town (FP) and Brewster to Hancock (BH). The delays of all observed source pairs are shown in this figure. The high quality of the global fit is very clear, and indeed superior to the results of the epoch reported in Martí-Vidal et al. (2008). The rms of the post-fit undifferenced delays range from 2.2 ps (baseline Brewster − Hancock observing source 00) to 54 ps (baseline Kitt Peak − North Liberty observing source 20). For the differenced delays, the rms of the post-fit residuals range from 0.26 ps (Brewster − Pie Town observing the pair $19-20$) to 7 ps (Fort Davis − Mauna Kea observing the pair $18-20$).

For the Q band, the rms of the post-fit undifferenced delays range from 3.3 ps (baseline Kitt Peak − North Liberty observing source 08) to 36 ps (baseline Brewster − Kitt Peak observing source 19). For the differenced delays, the rms of the post-fit residuals range from 0.53 ps (Brewster − Pie Town observing the pair $19-20$) to 10 ps (Fort Davis − Hancock observing the pair $18-20$).

In Figure 4.10, we show the undifferenced and differenced phase-delays for two representative baselines: Kitt Peak to Pie Town (KP), which corresponds to the shortest baseline in our sample (~ 420 km); and Hancock to Mauna Kea (HM), which corresponds to the longest baseline in our sample (~ 7500 km). The residual delays of all observed source pairs are shown in this figure.

The uncertainties in all observables were scaled to the rms of the post-fit residuals, arranged for each baseline and source pair, to minimize the effect of bad data on the final astrometric results, as also done in Martí-Vidal et al. (2008).

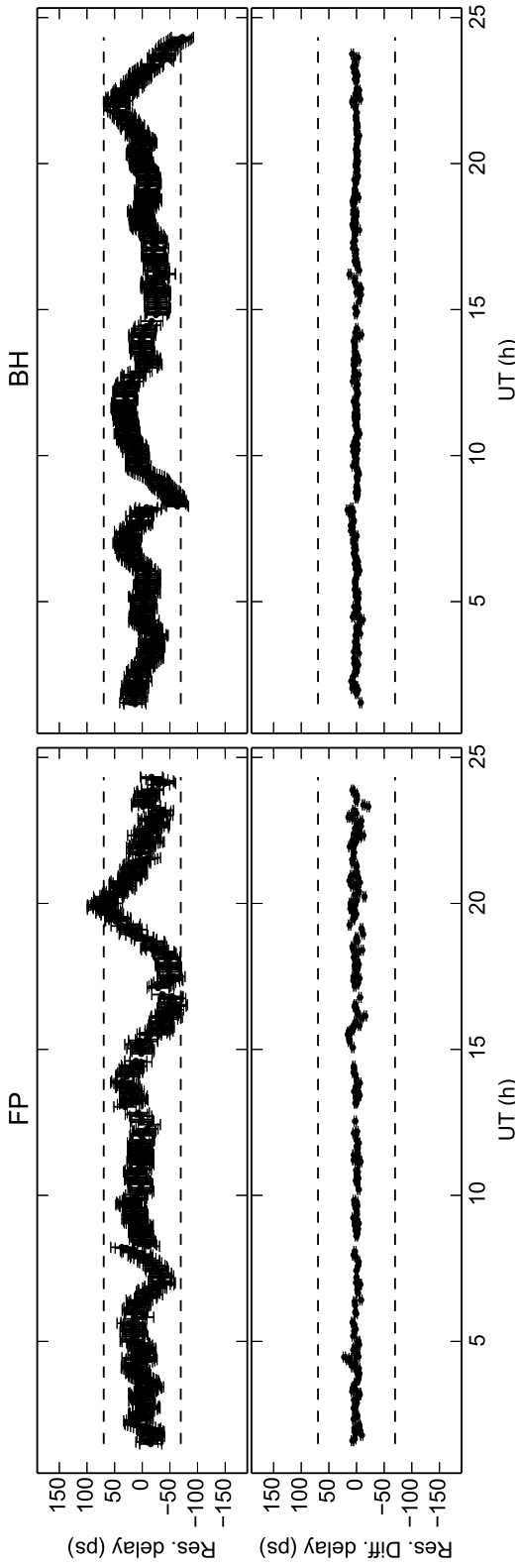

Figure 4.9: Post-fit residual phase delays for baselines Fort Davis – Pie Town (left) and Brewster – Hancock (right) for all observed sources: undifferenced delays (top); differenced delays (bottom). The dashed lines correspond to the delays of a $\pm 2\pi$ phase ambiguity at 14.4 GHz. The error bars are shown in all figures.

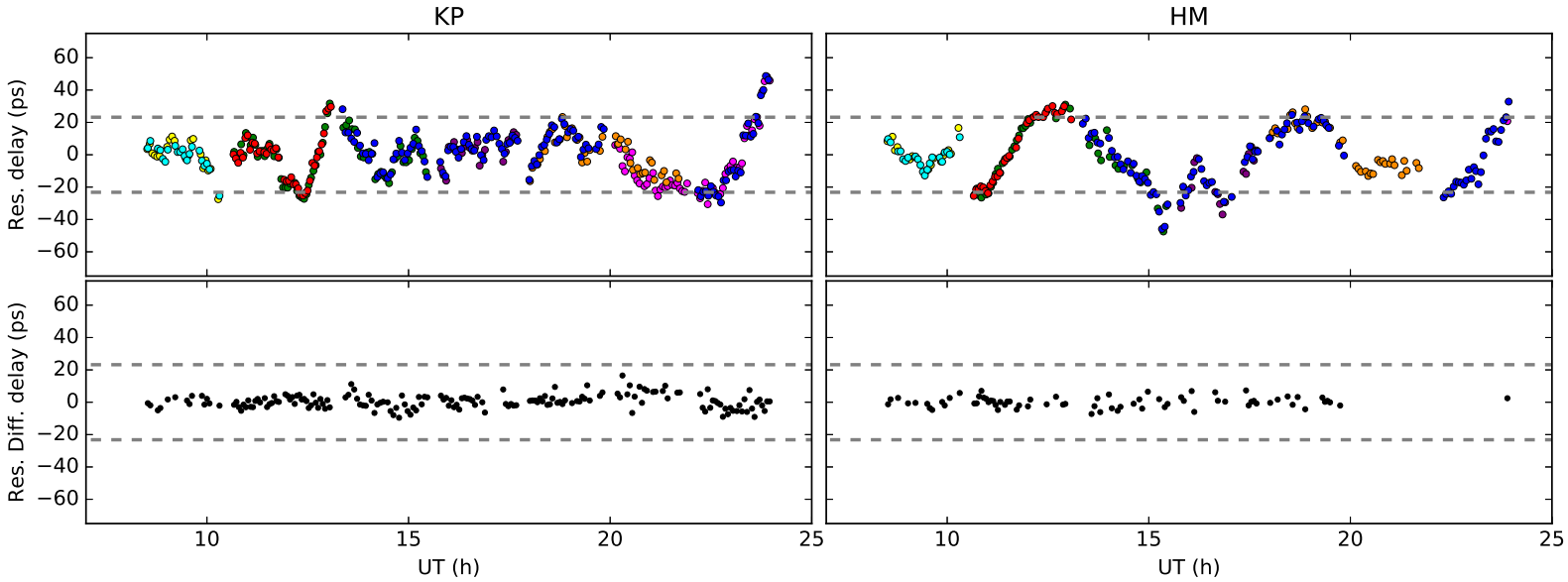

Figure 4.10: Post-fit residual phase-delays for baselines Kitt Peak – Pie Town (left) and Hancock – Mauna Kea (right) for all observed sources: undifferenced delays (top); differenced delays (bottom). The dashed lines correspond to the delays of a $\pm 2\pi$ phase ambiguity at 43.1 GHz. Each color represents one source in the sample. The lack of residual differenced phase-delays between $20 - 25$ h for the baseline HM is due to low S/N data of the source 20 (magenta) in that interval. The error bars are not shown in this figure for clarity.

Table 4.4: Results for the source pairs at U band: the displacements indicate the change in angular separation among source cores between the two epochs.

Pair	$U_2\|U_1$ (mas)
01 - 00	-0.334 ± 0.190
01 - 02	-0.123 ± 0.065
04 - 06	$+0.451 \pm 0.230$
08 - 07	-0.440 ± 0.300
11 - 10	$+0.423 \pm 0.090$
11 - 18	-0.920 ± 0.970
18 - 17	-0.371 ± 0.750
18 - 20	-0.394 ± 0.210
19 - 20	-0.260 ± 0.640

4.6.1 Changes in source separation with time and frequency

From the global astrometric analysis, we can analyze changes in the source core positions between our observations, either over time (i.e., between 2000 and 2010) or between frequencies (i.e., U and Q bands). We have used source 07 (0716+734) as the absolute reference source, because it has shown a rather compact structure at all epochs and frequencies. However, the choice of a different reference source does not affect the observed differences in source separations substantially (the disagreements are well within the error bars), since any shift in the sky (due to the shift of the reference source) keeps constant the angular separations among the sources.

Source separation as a function of time

We call θ the angular separation between a given pair of sources. Since we refer the position of the sources to the intensity peaks at each frequency, we can think of the angular separation as a function of time (proper motions) and frequency (core-shifts). Thus, we write $\theta(t,\nu)$. First, we determined the changes in the angular separation between epochs for the case of *almost* the same frequency ($\nu \sim 15$ GHz, U band). If we denote epochs 2000 and 2010 with indexes 1 and 2, respectively, the change in angular separation of a pair of sources between the two epochs at U band, $\Delta\theta_{U_2|U_1}$, will be

$$\Delta\theta_{U_2|U_1} = \theta_{U_2} - \theta_{U_1}, \tag{4.1}$$

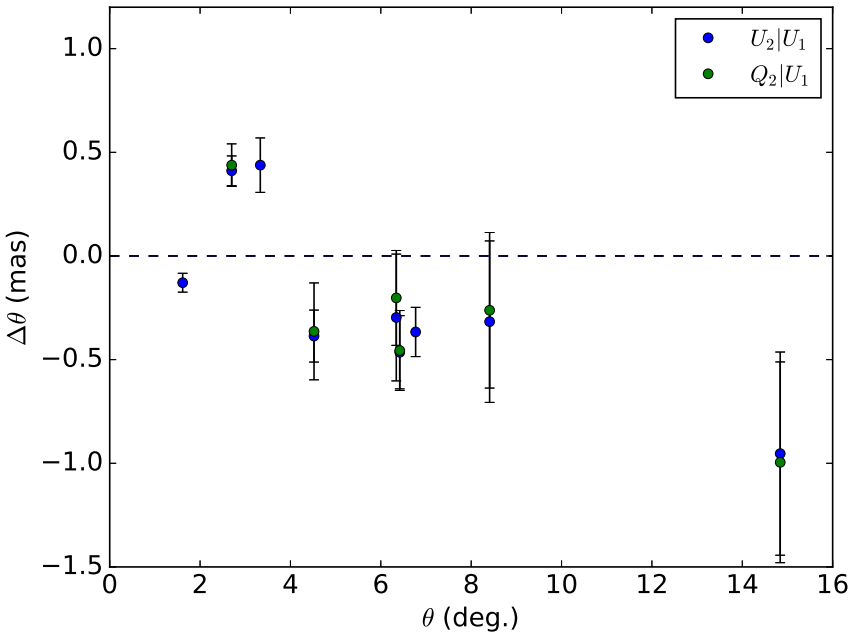

Figure 4.11: Differences in source separations between years 2000 and 2010 among all the source pairs observed in common in the two epochs at the different frequencies.

where θ_{U_1} and θ_{U_2} are the angular separations of the pair of sources (at U band) in years 2000 and 2010, respectively. Since the *a priori* uncertainties selected for the U band were slightly different to those selected for the Q band (see Section 4.5.2), we present first the results for the U band in Table 4.4.

On the other hand, since we have also determined the position of the sources at Q band, we can calculate the change in the angular separation between epochs and frequencies, i.e.,

$$\Delta\theta_{Q_2|U_1} = \theta_{Q_2} - \theta_{U_1}, \tag{4.2}$$

where θ_{Q_2} is the angular separation between a pair of sources at Q band in year 2010. In Figure 4.11, we show the changes in angular separation between sources as a function of source separation for the U band (epochs) and Q band (frequencies and epochs) with respect to the U_1 reference positions.

We find that the results at U (blue) and Q (green) bands are compatible at 1σ for those source pairs available at both bands. For the U band, on average and in absolute value, the source pairs have changed their separations by 0.26 ± 0.20 mas (compatible with zero), although there is a pair of sources, $11-10$, for which a

non-zero proper motion is detected at 4.7σ. The proper motions of the 14.4 GHz cores, averaged over a decade, are thus in the range $0-100$ μas yr^{-1}. In contrast, a comparison of the images of all sources in years 2000 and 2010 (see Figure 4.2) indicates that a substantial evolution in the source structures has taken place over a decade in some of them, with differences in the contour locations (with respect to the position of the peak intensity) of the order of a large fraction of a milliarcsecond (this is specially true for source 11).

These results suggest that a small fraction of the jet cores (at least, source 11) whose locations are believed to be relatively stable, compared to those of optically-thin features (Blandford & Königl, 1979), do change after a few years their absolute positions in the sky at levels higher than the astrometry precision of current and future AGN-based inertial reference frames.

Titov et al. (2011) have reported on proper motions for a large sample of radio-bright AGN, from global geodetic and astrometric VLBI observations spanning several decades. Indeed, all the S5 polar cap sample sources, but 02, have peculiar motions reported by Titov et al. (2011). The average peculiar motion for the S5 sources at 8 GHz, according to Titov et al. (2011), is 99 ± 65 μas yr^{-1}, which is of the order of the peculiar motions that we report for the same sources at 14.4 GHz (i.e., $0-100$ μas yr^{-1}).

There are other cases of AGNs where systematic motions have been found in their jet cores from intensive VLBI campaigns in phase-referencing mode, either at several frequencies (e.g., Martí-Vidal et al., 2011) or at a single frequency (e.g., Bartel, 2012). In some sources, the core motions appear to be periodic (likely due to jet precession, e.g., Martí-Vidal et al., 2011; Kudryatseva et al., 2011; Lobanov & Roland, 2005) and could be the effect, for instance, of either binary central engines or large-scale hydrodynamical instabilities (e.g., Perucho et al., 2006). More random jitterings found in other jet cores (e.g., Bartel, 2012) could be due to a randomly-changing activity in the central engine.

The peculiar core motions reported in all these works reach values of up to several tens of μas yr^{-1}, which are similar to the proper motions reported here for the S5 polar cap sample. These results somewhat challenge the picture of an astrometrically-stable AGN jet core.

Table 4.5: Results for the source pairs at U and Q bands: the displacements indicate the change in angular separation between frequencies and epochs (second column) and between frequencies for the same epoch (third column).

Pair	$Q_2\|U_1$ (mas)	$Q_2\|U_2$ (mas)
10 - 11	$+0.411 \pm 0.072$	$+0.027 \pm 0.083$
19 - 20	-0.386 ± 0.125	$+0.023 \pm 0.197$
18 - 20	-0.297 ± 0.306	$+0.094 \pm 0.304$
07 - 08	-0.465 ± 0.177	$+0.008 \pm 0.071$
17 - 18	-0.317 ± 0.389	$+0.055 \pm 0.177$
11 - 18	-0.953 ± 0.490	-0.042 ± 0.135

Source separation as a function of frequency

Combining Equations 4.1 and 4.2 we can also calculate:

$$\Delta\theta_{Q_2|U_2} = \Delta\theta_{Q_2|U_1} - \Delta\theta_{U_2|U_1} = \theta_{Q_2} - \theta_{U_2} \tag{4.3}$$

Since we use the same *a priori* positions of the sources to calculate θ_{Q_2} and θ_{U_2}, $\Delta\theta_{Q_2|U_2}$ contains information about the *combined* core-shift of the pair of sources (i.e., the difference of the core-shifts between the two sources). We summarize the results of Equations 4.2 and 4.3 in Table 4.5.

In Figure 4.12, we show the difference in angular separation between sources at different frequencies in year 2010. We find that all variations are compatible with zero at 1σ. Furthermore, if we apply the core-shift position corrections determined in Section 4.4 by means of phase-transfer phase referencing calibration, we conclude that all frequency-dependent changes in the angular separations between sources are also compatible with zero at 1σ.

The uncertainties in the source motions between epochs 2000 and 2010 were estimated using a Monte Carlo approach. We generated a set of one thousand different realizations of the fit, obtained by adding random tropospheric delays, ionospheric delays, and antenna-position shifts, as discussed in Section 4.5.2. From each Monte Carlo iteration, the motions of all pairs of sources between epochs 2000 and 2010 were computed. The uncertainties in the motions were then obtained from their standard deviation over all the Monte Carlo iterations. The contributions to the error budget related to other (non-atmospheric) effects, such as station clocks or UT1-UTC, are much smaller than those included in the Monte Carlo analysis, and were already taken into account in the estimate of the position uncertainties made by UVPAP, which are based on the post-fit covariance ma-

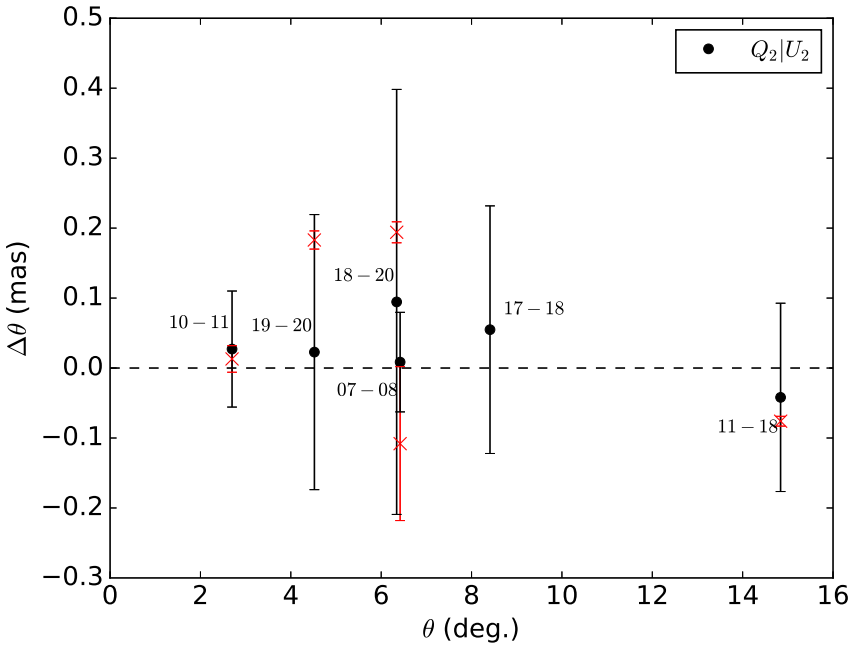

Figure 4.12: Differences in source separations between U and Q bands in year 2010. The red crosses correspond to the changes in angular separations estimated from the core-shift position corrections given in Table 4.3.

trix. These uncertainties were added in quadrature to those from the Monte Carlo analysis.

4.6.2 Inter-frequency differential phase-delay astrometry

Once all the 2π ambiguities (and clock offsets) of the phase-delays were corrected at both bands, all the data could be included into a *single self-consistent fit* (comprising data from both bands). The differences of delays between the bands for each source (we call them "inter-frequency differential phase-delays", IFDPD) are sensitive to the change of source position with frequency (i.e., the core-shift). Given that the ionospheric effects were removed from the group (and phase) delay observables before the phase connection (using IONEX maps, as described in Martí-Vidal et al., 2008), at least to a first-order approximation, the remaining effects in the data are all non-dispersive (i.e., numerically the same for both bands). Therefore, we can use the same atmospheric model, clock drifts, and antenna positions to fit the delays at the two frequencies.

There is, though, a small instrumental effect left between the bands, which is related to the different optical paths followed by the signals at the different frequencies, from the antenna sub-reflectors to the VLBI backends. We account for this effect by including a new set of fitting parameters into the model, in the form of antenna-dependent constant clock offsets (common to all sources), for only Q band. If τ_U and τ_Q are the delays at U and Q band, respectively, for a given source at a given baseline and time, then

$$\tau_Q - \tau_U = \tau_Q^{geo} - \tau_U^{geo} + \tau_Q^{inst} - \tau_U^{inst} + \tau_Q^{sou} - \tau_U^{sou}, \tag{4.4}$$

where τ^{geo} is related to antenna positions and atmosphere (the same at both bands), τ^{sou} is the delay induced by source structure (which encodes the core-shift) and τ^{inst} contains the instrumental effects (clock drifts and optical path into the system). The drift of the maser is the same at both bands, so that $\tau_Q^{inst} - \tau_U^{inst}$ is only affected by the different (and constant) optical path of the signals between U and Q bands. This delay is modeled as

$$\tau_Q^{inst} - \tau_U^{inst} = \Delta\tau^A - \Delta\tau^B, \tag{4.5}$$

where A and B are the antennas in the baseline and $\Delta\tau^X$ is the extra path of the Q signal (with respect to U) at antenna X (i.e., the extra clock offsets added to the UVPAP model, for the IFDPD analysis). Using this set of extra parameters, the differences in phase-delays at the two frequencies can be used to determine the core shift, since Equation 4.5 models the instrumental delay, so that only the term $\tau_Q^{sou} - \tau_U^{sou}$ remains unmodeled in Equation 4.4.

The IFDPD analysis is performed in a global fit, where all sources are fitted to the same geometrical and instrumental interferometer model. As was discussed in Section 4.6, the use of more than two sources in a global differential-astrometry fit increases the precision and robustness of the astrometry results, due to the extra redundancy in the observables (i.e., the same clock drifts and atmospheric model apply to all the different sources and source pairs). Extending the global analysis to the IFDPD observables has thus clear advantages compared to the standard SFPR technique, where each target uses only gains interpolated from one calibrator.

We performed the IFDPD analysis using a Monte Carlo approach, to determine the effects of atmosphere, clocks, and antenna positions on the estimated core-shifts. The atmospheric delay at each station was allowed to vary following Gaussian distributions with a variance of 0.1 ns (for the troposphere) and 0.5 TECUs (for the ionosphere), which are realistic estimates of the uncertainty levels in the atmospheric models, as we previously discussed in Section 4.5.2. The antenna positions were left to vary following Gaussian distributions with a variance

of 1 cm. On each iteration, the (antenna-dependent) CCOs were found for each antenna and source at Q band in an automatic way, as was also done in the global fit (see Section 4.5.2). We show in Figure 4.13 the 2D histograms of the core-shifts for all sources with successful fringe detections at both bands, as estimated from the IFDPD analysis. The core-shift estimates obtained with the SFPR technique are shown as red crosses for the sources with successful SFPR detections.

For sources 10, 11 and 18, the IFDPD core-shifts are almost degenerate (at sub-mas scales) among different directions on the sky. This degeneracy indicates strong coupling with the varying parameters in the Monte Carlo analysis (mainly, the atmosphere and its cross-talk with the CCOs at Q band). For source 20, the uncertainty derived from the Monte Carlo analysis is very large (of the order of a milliarcsecond in the major axis of the 2D histogram distribution), which makes the result unusable. For sources 07, 00, 02, and 08, the IFDPD core-shifts have lower uncertainties, although we see a remarkable difference between the IFDPD and the SFPR core-shift estimates for source 07. At the moment of writing these lines, we do not find any explanation for such a difference between the two methods. The SFPR result seems to agree better with the source morphology.

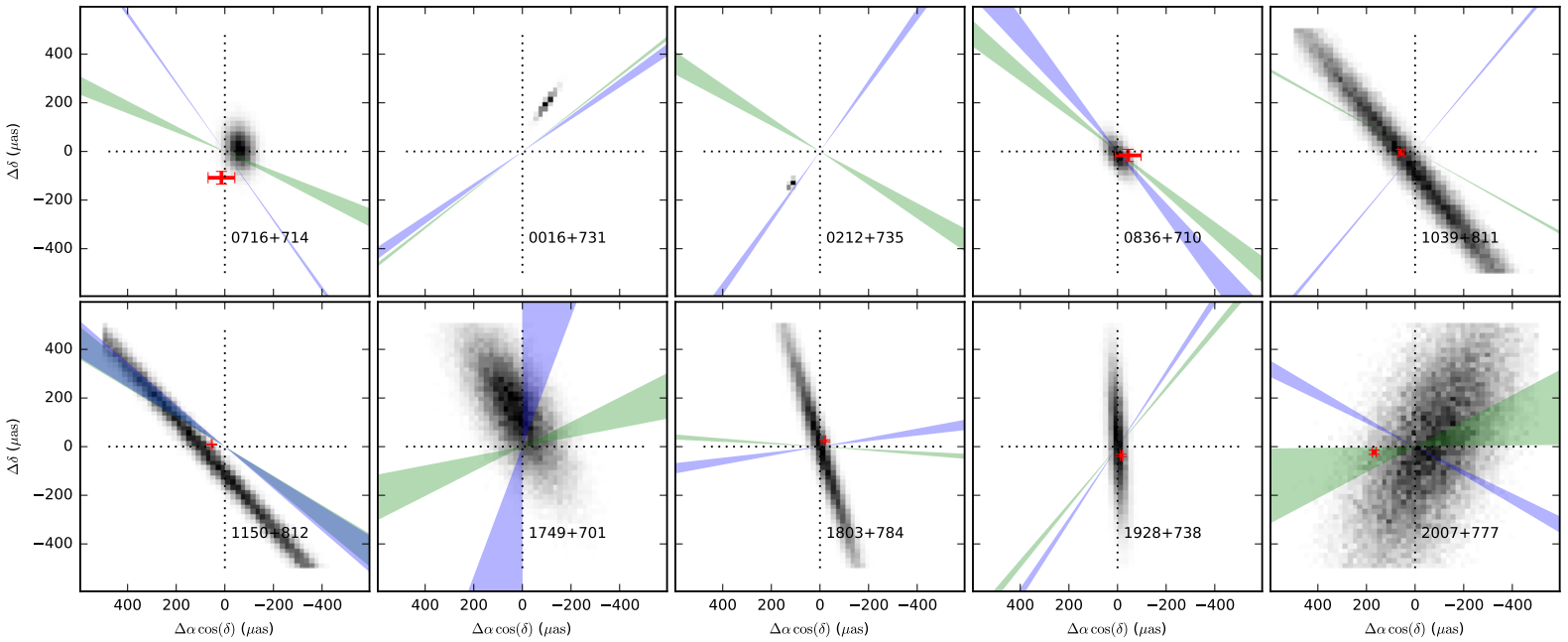

Figure 4.13: In black, 2D histograms of the core-shifts in the S5 polar cap sample estimated from the IFDPD analysis (see Section 4.6.2). In red crosses, core-shifts estimated using the SFPR technique (Section 4.4). Blue (green) shaded areas indicate the orientations (within 1σ) of the main axis of the Gaussian intensity distributions fitted to the jet cores at U (Q) band (see Section 4.7.1).

4.7 Core structures

4.7.1 Visibility model-fitting of the core emission

As a complement to our global differenced phase-delay analysis, we have carried out a morphological study of the core regions at both bands. In principle, and as long as the core regions can be resolved at our VLBI resolutions, we would expect that the elongation of the jets in the core regions would be aligned to the direction of the core shifts. In addition to this, and according to the standard jet interaction model (e.g., Blandford & Königl, 1979), the elongations of the core regions at both bands should have a similar orientation, as long as the jets are straight in these regions. Indeed, if the core emission at U and Q bands comes from the conical regions of the jets, the core sizes should be inversely proportional to the observing frequencies (e.g., Blandford & Königl, 1979; Marscher, 1980; Martí-Vidal et al., 2011).

Any deviation of the core morphology from these predictions, which are based on the standard jet model, may indicate either bent jet geometries or emission from non-conical (i.e., concave) jet regions, likely related to the Poynting-dominated zone of the outflows close to the jet bases (e.g., Marscher, 1980; Marscher et al., 2008; Martí-Vidal et al., 2013).

We have used the UVMULTIFIT program (Martí-Vidal et al., 2014), based on the CASA[2] software by NRAO, to derive the sizes, morphologies and orientations of the core regions of all sources detected in both bands. Before fitting the core regions, we subtracted the optically-thin jet extensions from the visibilities, using the CASA task `uvsub`. The emission from the optically-thin jet extensions was taken as that of all the CLEAN components beyond one restoring beam from the peak intensity (using natural visibility weighting). After subtraction of the jet extensions, the core regions were fitted using elliptical Gaussian intensity distributions.

In Figures 4.14 and 4.15, we show some examples images that show the subtraction of the optically-thin extended jet components, as well as images of the post-fit residuals (right), after fitting the Gaussian intensity distributions to the core regions. In all cases, the unmodeled (i.e., residual) post-fit peak intensities are $\lesssim$1% of the pre-fit peak intensities. This indicates that most of the core emission can indeed be sucessfully modeled with an elliptical Gaussian intensity distribution. We show in Figure 4.13 the orientations (within 1σ) of the main axis of the Gaussian intensity distributions fitted to the jet cores at both bands.

[2] `http://casa.nrao.edu`

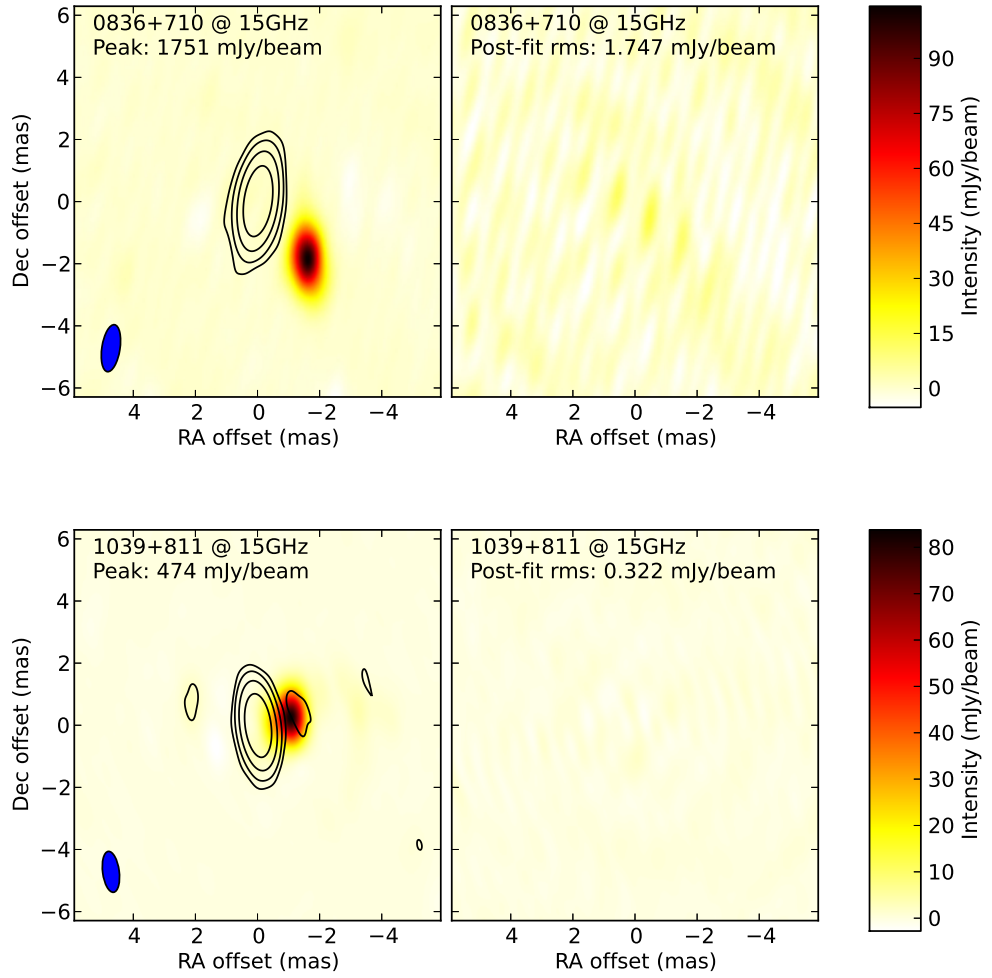

Figure 4.14: Left, images of sources 08 (top) and 10 (bottom) at U band, separating the core emission (contours) from the extended jet (color scale). The contours are spaced logarithmically in ten levels, running from two times the rms of the residuals to the image peak. Right, post-fit residuals of UVMULTIFIT, fitting a Gaussian brightness distribution to the core emission of each source.

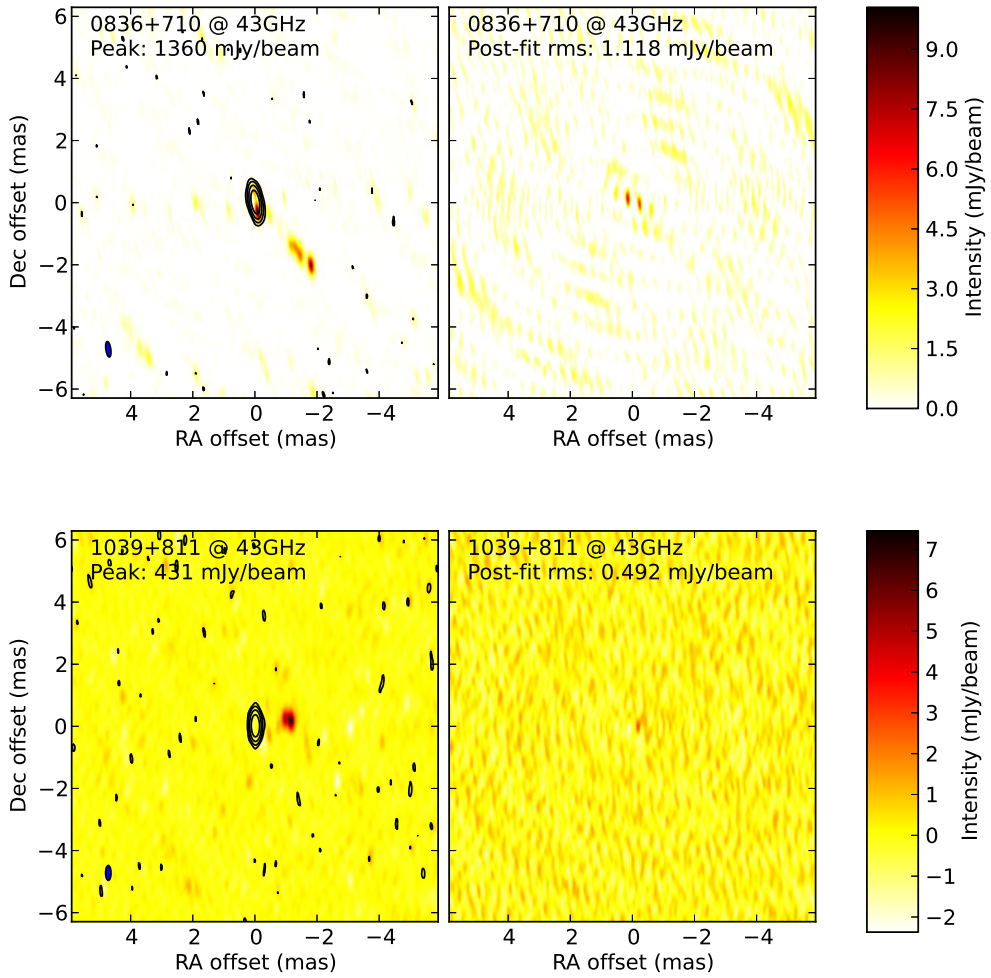

Figure 4.15: Same as Figure 4.14, but at Q band.

4.7.2 Fitting results

In Figure 4.16, we show the orientations, ellipticities (i.e., minor-to-major axis ratios) and sizes of all the Gaussians fitted to the jet cores at both bands. Several conclusions can already be drawn from this comparison between the bands. On the one hand, the position angles of the major Gaussian axes are similar between the two bands for most sources (differences of a few sigmas are seen between the bands), with some outliers (sources 02, 07, 10, and 20). Hence, the jets seem to be rather straight for a large subset of the sample.

On the other hand, the axis ratio, which should be the same at both bands if the core emission originates in the conical jet region (since, in this region, the brightness distribution is self-similar at any frequency), shows remarkable systematics between the two bands. At the lowest frequency, the ratio is typically higher (i.e., the Gaussians are more elongated at the higher frequency). A natural explanation of this deviation from self-similarity is that there may be a contribution to the emission at Q band coming from the concave (i.e., Poynting-flux dominated) jet region, where there is a shallower dependence of the magnetic-field intensity and particle density with distance to the jet base (Marscher, 1980), hence extending the core regions at the highest frequencies (Martí-Vidal et al., 2013).

This interpretation is supported by the comparison of core sizes (Figure 4.16, right), where the size of the minor Gaussian axis (i.e., the axis related to the width of the jet), when scaled by the frequency ratio from the observed U band size, is *smaller* than the observed Q band size. At the concave jet region, the jet width is not proportional to the distance from the jet base. Hence, if the emission at Q band (or at least, a fraction of it) comes from the concave jet region, the estimated jet width will be larger than the frequency-scaled size from the U band.

Our results with visibility model-fitting thus seem to indicate that at least a fraction of the core emission at Q band is not originated in the conical jet region, and/or that the standard jet model may not apply to all sources in our sample at Q band. Of course, this will have an effect on the expected core shift, since it will be smaller in the concave jet region, compared to that in the pure conical model (e.g. Martí-Vidal et al., 2013).

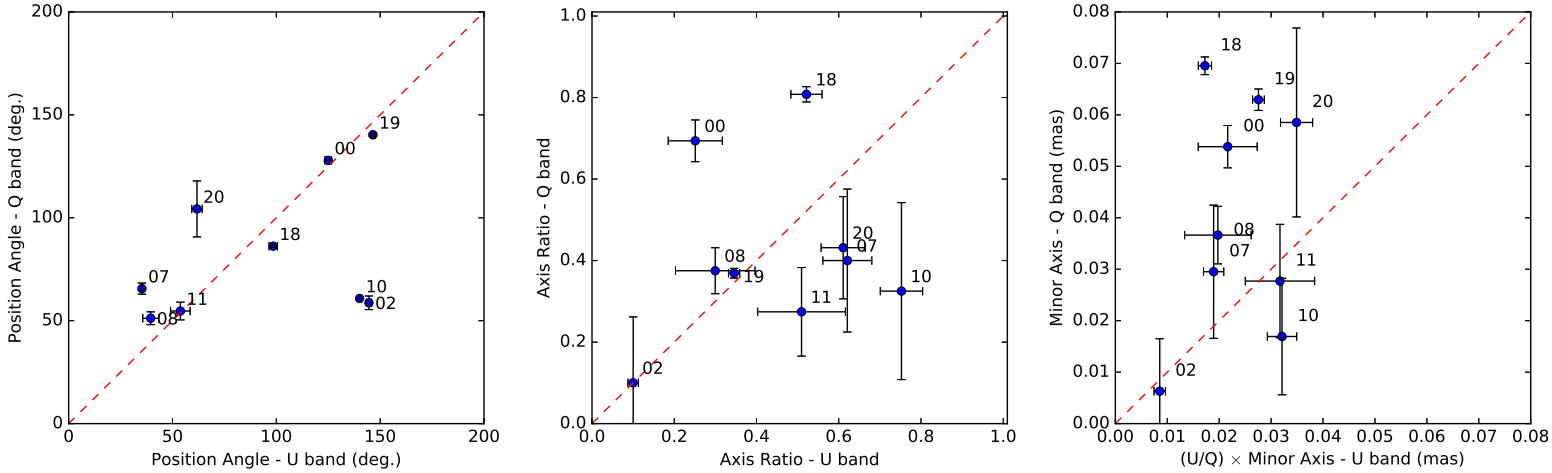

Figure 4.16: Left, position angles of Gaussian intensity distributions fitted to the core emission at U band (horizontal axis) and Q band (vertical axis). Center, minor-to-major axis ratios of the same fitted Gaussian intensity distributions. Right, size of the minor Gaussian axis at U band (multiplied by the U/Q frequency ratio) vs. size of the minor Gaussian axis at Q band.

4.7.3 Core-shifts vs. core-orientations

From the standard jet model, it is expected that the major axis of the Gaussian distributions fitted to the core (which would follow the local direction of the jet) will be in line with the direction of the core-shift. This statement holds as long as the jet remains straight in the region between the cores at both bands. We can test it by direct comparison of our core-shift estimates and the UVMULTIFIT results. Indeed, Rioja et al. (2015) find agreement between core-shift directions at several bands (from 43 GHz up to 140 GHz), observed with the Korean VLBI Network (KVN) and the orientations of the jets in several AGN. We notice, though, that the limited angular resolution of the KVN (beam larger than the core-jet regions) might introduce blending effects of the jet emission within the beam and partially mask the true core-shift in these sources. Instead, the VLBA angular resolution is adequate to resolve the core from the extended jets.

The two sources with highest S/N in the IFDPD core-shift estimates are 00 and 02 (see Section 4.6.2). We show in Figure 4.17 a reconstruction of the jet core structure based on the Gaussians fitted with UVMULTIFIT. We show the FWHM of the cores at both bands shifted one from the other using the IFDPD core-shift. For source 00, we see an excellent agreement between the orientations of the Gaussians at both bands and the direction of the core-shift. This is indicative of a straight jet (notice that source 00 falls on the 1:1 correlation in Figure 4.16, left). Regarding source 02, the core-shift is almost aligned to the major axis of the core Gaussian at U band, although the core Gaussian at Q band shows a rotation of almost 90 degrees with respect to U band. This may be indicative of a strongly curved jet at pc scale from the central engine. Similar curved jet structures have indeed been reported for other AGN (e.g., Savolainen et al., 2006; Molina et al., 2014).

A direct comparison between the SFPR core-shift direction and the orientation of the elliptical-Gaussian intensity distributions, fitted to the core emission at both bands, is shown in Figure 4.18 (top). We notice that, for a correct comparison, an ambiguity of 180 degrees has to be applied to the position angles of the (axisymmetric) elliptical Gaussian distributions. We have done so by either adding or subtracting 180 degrees to the UVMULTIFIT estimates, so that the angles get as close as possible to the core-shift directions. For completeness, we show in Figure 4.18 (bottom) the comparison between core position angles and IFDPD core-shift directions (only for those sources with clear, non-degenerate, detections). In both cases (SFPR and IFDPD), there is a hint of a weak correlation. For the SFPR, we find a correlation coefficient R^2 of 0.59 and 0.56 for U and Q bands, respectively. Sources 19 and 07 are far from the correlation by about 50 degrees at both bands, whereas sources 08, 11, 10, 18 and 20 are about $20-40$ degrees away.

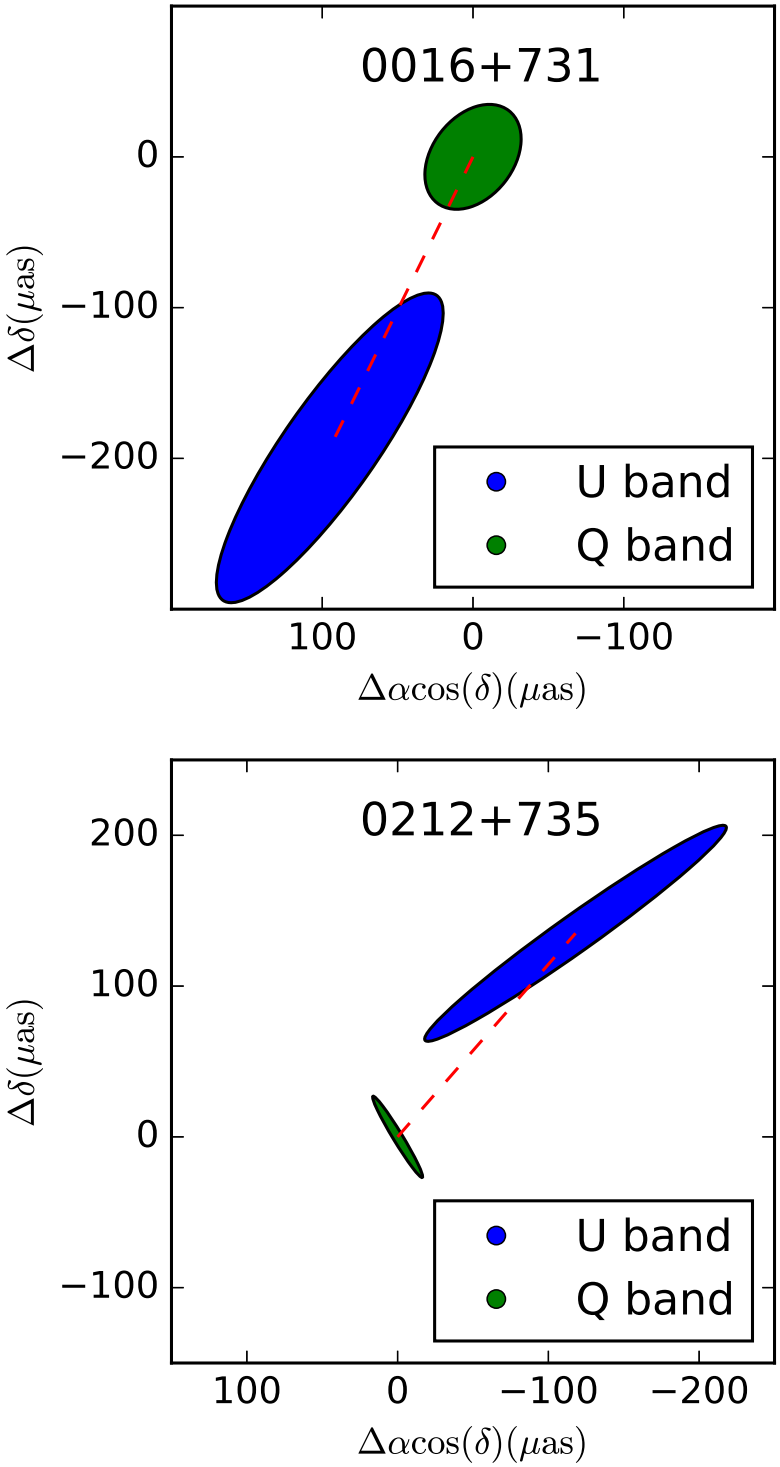

Figure 4.17: FWHM of the Gaussian intensity distributions fitted to the cores of sources 0016+731 (top) and 0212+735 (bottom). The U and Q distributions have been placed as indicated by the core-shifts estimated from our IFDPD analysis (red dashed line). Notice that the directions of the core-shifts almost coincide with the orientations of the main axis of the Gaussians at U band.

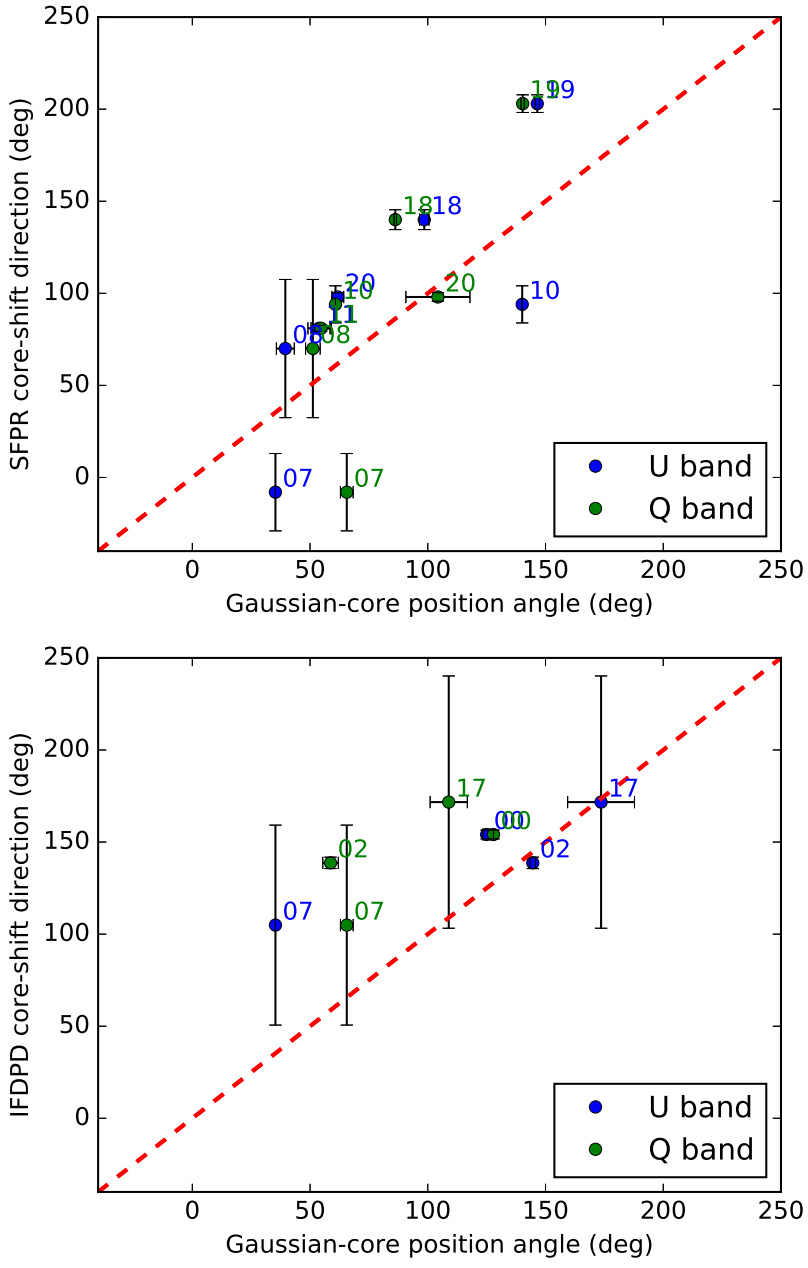

Figure 4.18: Core-shift directions estimated using the SFPR (top) and the IFDPD (bottom) techniques vs. position angles of Gaussian intensity distributions fitted to the core emission at U (blue) and Q (green) bands. Only sources with successful (non-degenerate) core-shift detections are shown in the bottom figure.

The lack of a 1:1 correlation between the morphological jet direction (i.e., the position angle of the core Gaussian distributions) and the direction of the core shift indicates large departures of the sources from straight jets. Helicoidal jet shapes, coupled to opacity effects at the jet cores, could help explain both the different orientations of the cores at the different frequencies seen in some sources (Figure 4.16, left), as well as the misorientation of the core-shift with respect to the core major axes (Figure 4.18).

4.8 Spectral-index maps

We show in Figure 4.19 the spectral-index distribution (i.e., α, being the flux density $\propto \nu^{\alpha}$) for the sources where a successful phase-transfer calibration could be performed. For the spectral-index computation, we have used a compromise convolving beam of 0.6×0.6 mas FWHM for the images at 14.4 GHz and 43.1 GHz. In Figure 4.19, we see that the jet cores have nearly flat (or even inverted) spectra, with the spectral index, $\alpha > 0$. This is due to synchrotron self-absorption effects in the core region. The jet extensions are, however, optically thin, with $\alpha < 0$. Similar distributions of spectral index have been found in many other AGN jets (e.g., Marcaide & Shapiro, 1984; Kovalev et al., 2008) and are well understood in terms of the standard jet model. We notice that, since the 14.4 GHz images have been over-resolved, there can be artifacts in the spectral-index distributions shown, especially in the regions close to the lowest contours.

A peculiar case is source 06. The hardest spectrum (i.e., highest spectral index) is found on the SW component. This would be the "spectral core" of the source. However, the intensity peak at both 14.4 GHz and 43.1 GHz (i.e., what we could call the "morphological core") is located at the NE component. In any case, a clear result is that the SW emission does show clear signs of synchrotron self-absorption (being thus more likely close to an AGN central engine) and is much misaligned to the 43.1 GHz jet extension propagating towards the west from the NE component. A possible explanation for this morphology could be that the true core of the jet is the SW component, with the jet propagating towards NE. The hot spot at NE could be due, for instance, to a strong interaction region of the jet with its surrounding medium, which would break or re-direct the jet toward the west (causing the east-west jet extension seen in the 43.1 GHz image of the NE component). This interpretation, though, would be insufficient to explain another intriguing morphological feature in this source: there is a hint of ring-like structure in the image at 14.4 GHz, with a diameter of $\sim$1 mas. This structure resembles the image at 5 GHz reported by Dodson et al. (2008) from space-VLBI observations.

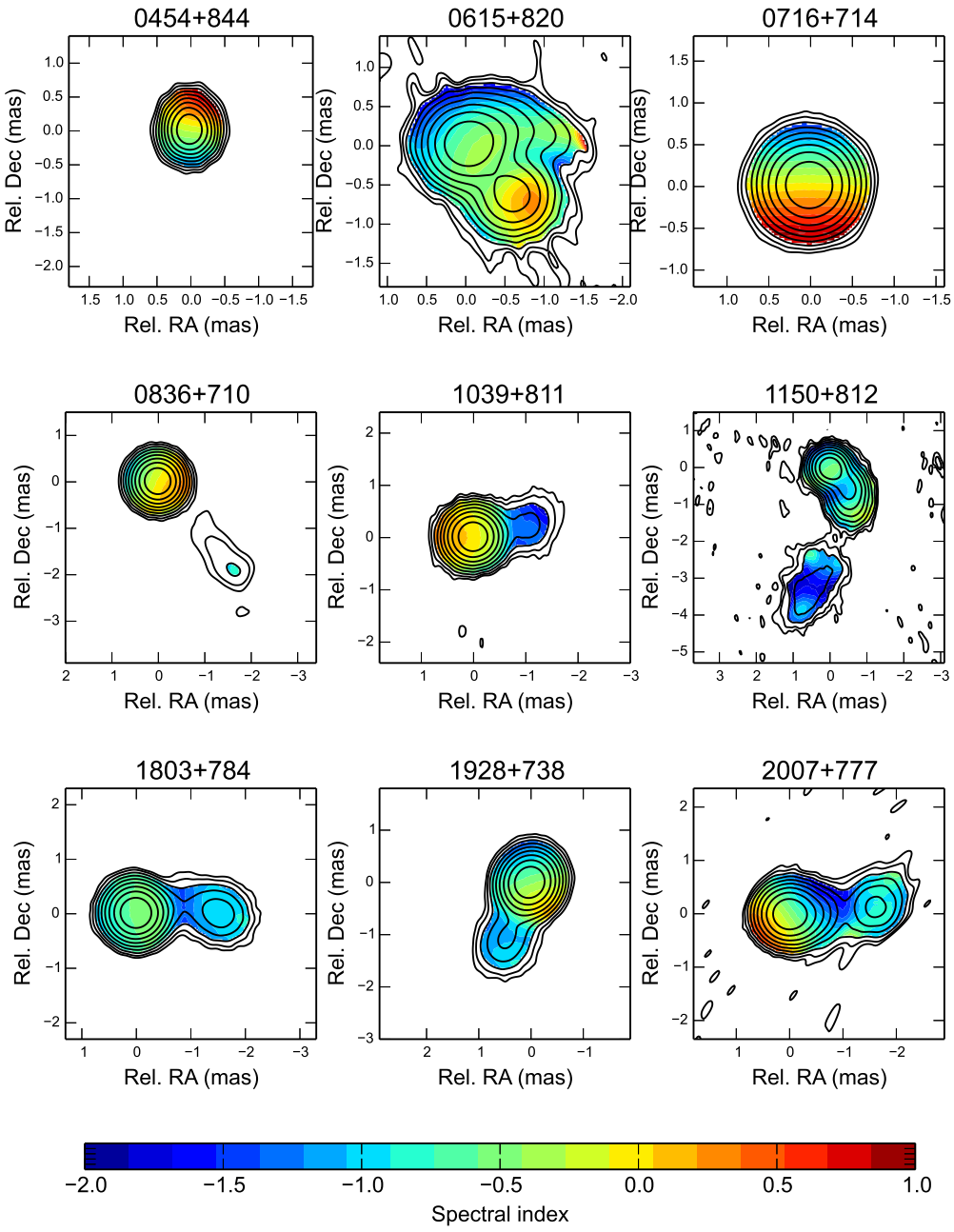

Figure 4.19: Spectral-index distribution of a subset of the S5 polar cap sample sources (see text). The contours correspond to the 43.1 GHz images, convolved with a beam of 0.6×0.6 mas FWHM. We notice that the effects of the core-shift uncertainties (Table 4.3) are not shown in this figure.

A possible explanation for such a structure might be a mas-size gravitational lens, although a more complete multi-frequency (and full-polarization) analysis should be performed to confirm this possibility. Another possibility would be a strongly bent jet oriented to the line of sight, as is seen in, for example, PKS 2136+141 (Savolainen et al., 2006), although the fact that the ring structure in 06 is unbroken would be difficult to explain in that scenario.

An alternative explanation could be that NE and SW are the cores of different AGN, so that 0615+820 would be a binary massive black hole. A precise astrometric follow-up between NE and SW at high frequencies, together with simultaneous observations at lower frequencies (to study the evolution of the spectral-index distribution) would be required to confirm this possibility.

In Figure 4.20, we show the over-resolved images of source 06 at 15 GHz for year 2000 (blue contours) and 2010 (red contours), using the NE component as position reference. We indicate with crosses (of the same contour colors) the location of the SW component at each epoch. An intriguing shift is seen between the two epochs, which might be caused by an orbital motion of SW in a binary massive black hole. In addition, a third weaker component can be seen to the west of SW in year 2000. A deeper analysis of the binary black hole scenario (and other alternative explanations) for source 06, using all available VLBI data of this source, will be published elsewhere.

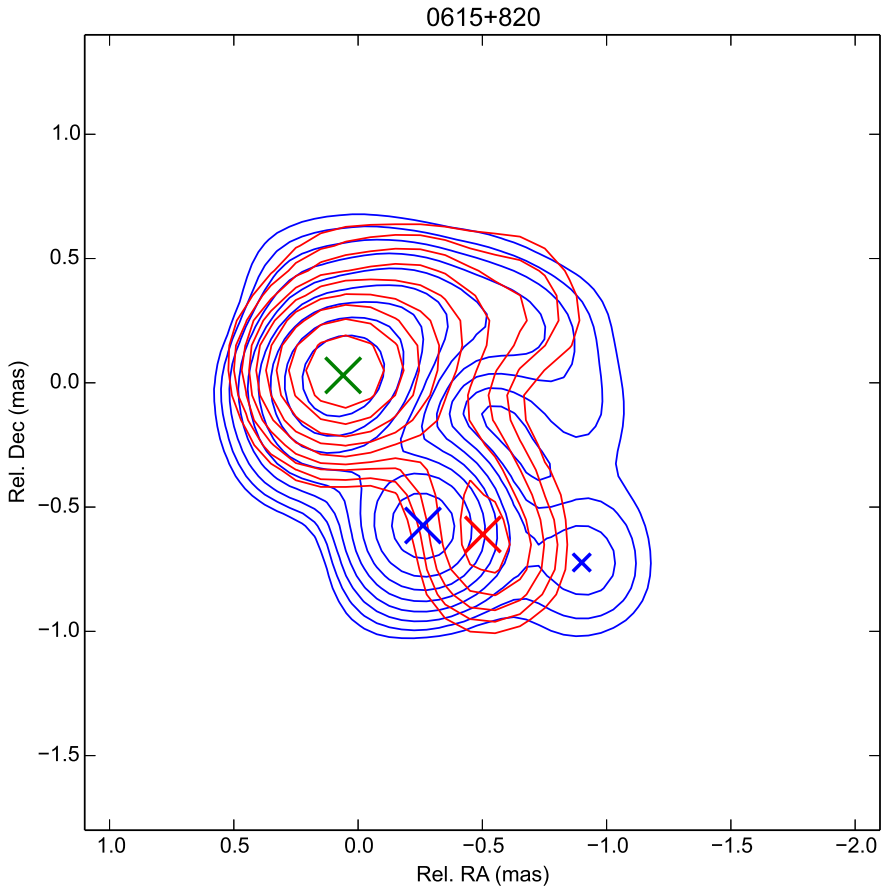

Figure 4.20: Images of source 06 at 15 GHz in the year 2000 (blue contours) and 2010 (red contours). The restoring beam is 0.4×0.4 mas and the ten contours are spaced logarithmically from 5% to 99% of the peak intensities (0.15 and 0.27 Jy/beam for year 2000 and 2010, respectively). The blue and red crosses indicate the position of the SW component in 2000 and 2010, respectively. The green cross shows the location of the NE component (set equal in both epochs). A second component peak west of the SW component in the year 2000 is also shown by a smaller blue cross.

4.9 Conclusions

We report on quasi-simultaneous VLBA observations of the S5 polar cap sample at U and Q bands, performed in December 2010 in phase-referencing mode, using the FFS capabilities of the VLBA, and compare them to earlier results at U band. We have performed a high-precision wide-angle astrometric analysis of a complete radio sample, and for the first time in VLBI, we have globally connected the phase-delays at a frequency as high as 43.1 GHz. Since the delay corresponding to one 2π phase cycle at this frequency is so short ($\sim$ 23 ps), the Q band probably marks the observational limit for this astrometric technique, mainly due to the fast atmospheric variations and the long slewing time of the antennas between scans. A similar work at higher frequencies (e.g., 86 GHz with a phase cycle of $\sim$ 12 ps), where the atmospheric conditions vary faster than at lower frequencies, might not be feasible with the current instrumentation.

Our successful global astrometric analysis at Q band enables us to study the changes in the source core positions between different epochs (year 2000 at U band and year 2010 at U/Q bands) and/or between different frequencies (i.e., U and Q bands). From the inter-epoch analysis, we find that the differences in source separations among all the source pairs observed in common in the two epochs are compatible at the 1σ level between both bands. We find a 4.7σ proper motion of 42 ± 9 μas yr^{-1} between the jet cores of sources 10 and 11 between the epochs 2000 and 2010. For the rest of source pairs, the separations did not change above 2σ.

We have performed a SFPR calibration, from 14.4 GHz to 43.1 GHz, to determine the core-shifts. Only nine of the thirteen sources could be imaged with this technique and we find typical core-shifts of $0.05-0.2$ mas. From the inter-frequency analysis in year 2010, we find that the differences in source separations between U and Q bands are compatible at the 1σ level with those estimated with the SFPR technique.

We have developed an inter-frequency differential phase-delay analysis (IFDPD) to study the core-shift effect between the U and Q bands in a way independent of the SFPR technique. For sources 10, 11 and 18, the IFDPD core-shifts are almost degenerate (at sub-mas scales) in different directions in the sky, perhaps due to strong coupling between the parameters associated with the atmosphere (mainly residual ionosphere) and the CCOs at Q band in the Monte Carlo analysis. This issue might be leading to unreliable estimates of the core-shift directions for these sources. For sources 00, 02, 07 and 17 the uncertainties in the IFDPD core-shift directions are lower. The core-shift estimates of those sources are more accurate and less affected by atmospheric/CCO effects.

We have fitted the core emission at U and Q bands to Gaussian intensity distributions. We find that the position angles of the major Gaussian axes are similar between the two bands for most of the sources except for some exceptions (sources 02, 07, 10, and 20). This result indicates that a considerable fraction of the total sample shows rather straight jets. Besides, we have compared the core-shift directions to the core orientations at both bands and we have found that there is good agreement between the core orientations at U band and the core-shifts, for the sources with most accurate core-shift estimates (sources 00, 02, 07 and 17). This is an expected result since the orientation of the Q band core affects less the core-shift orientation than the orientation of the U band core. On the other hand, from the analysis of the axis ratio of the core Gaussians at each frequency, we conclude that at least a fraction of the Q band emission is likely to come from the concave jet region, where the jet width is not proportional to the distance from the jet base.

We have presented three different methods to study the core-shift effect and we conclude that, even though they do not agree in the estimate of the core-shift directions in some cases, they are all compatible in the absolute values of the core-shifts. In some cases, the discrepant orientations are due to insufficient information for the method used. In other cases, the discrepancies reflect assumptions of the methods and could be explained by curvatures in the jets and/or departures from conical jets. However, the absolute values of the core-shifts determined with all methods presented in this work are of the same order as those predicted by the statistical study of Kovalev et al. (2008) using a simplified SSA jet model (e.g., Lobanov, 1998b), if extrapolated to the whole S5 polar cap sample at U/Q bands.

Finally, we have constructed robust spectral-index maps of the sources. The spectral-index distributions follow the well-known steepening of the spectrum at the jet extensions, from an either flat- or inverted-spectrum regions associated to jet cores. There is one source, $0615+820$, that shows a remarkable double structure at 43.1 GHz (two components, one at northeast, NE, and one at southwest, SW), having one of them, NE, a prominent jet extension roughly perpendicular to the NE$-$SW direction. In this source, the true (synchrotron self-absorbed) jet core (the SW component) does not correspond to the absolute brightness peak (NE component). Possible explanations for this intriguing source structure could be either a strong jet bending at parsec scales from the AGN central engine (due to interaction with the ISM), a gravitational lens of mas scale, or a binary massive black hole. The relative astrometry between NE and SW at U band, using image over-resolution, shows a clear position drift of SW with respect to NE between years 2000 and 2010, thus supporting the third possibility. A deeper analysis on this source, using all the available VLBI data, will be published elsewhere.

Chapter 5

Supernova 1987A

Somewhere, something incredible is waiting
to be known.

Carl Sagan

Sunrise in Africa in the Middle Pleistocene. The Earth has suffered numerous glaciations. *Homo sapiens* has become the dominant specie in the world. Not too far from our planet, in a "nearby" galaxy 1.5×10^{18} (1.5 million million million) kilometers away, a star with the mass of about 20 times the mass of our Sun is about to explode...

In this chapter we introduce supernova SN 1987A. First, we talk about its discovery and the main properties that make this supernova such a particular object. Then we describe its light curve and evolution over the last three decades. We analyze the most important emission regions as well as the emission of dust and molecules from the innermost zones of the remnant. Finally, we conclude the chapter by presenting some state-of-the-art hydrodynamical models aimed to describe supernova explosions such as SN 1987A.

For a more detailed description of SN 1987A, we refer the reader to one of the three reviews published up-to-date: Arnett et al. (1989), McCray (1993), McCray & Fransson (2016), and references therein.

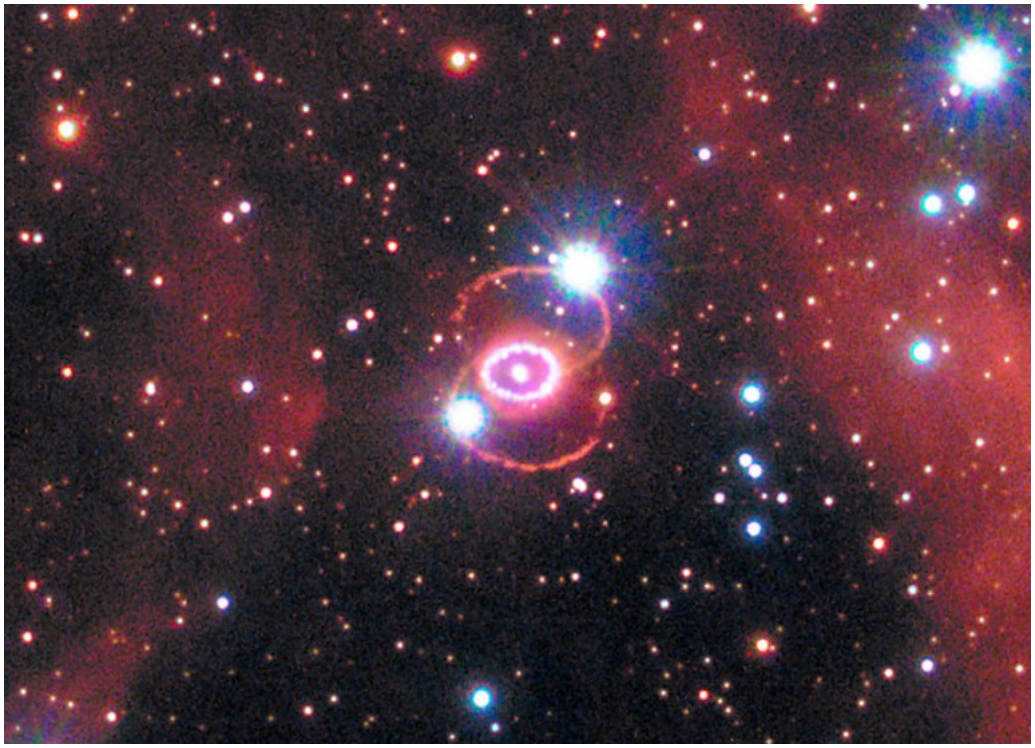

Figure 5.1: Hubble Space Telescope (HST) image of SN 1987A within the LMC, a neighboring galaxy to our Milky Way. The bright ring around the central region of the exploded star is composed of material ejected by the star about 20,000 years before the actual explosion took place. It is unclear how the two outer rings formed. Credit: NASA, ESA, R. Kirshner and P. Challis.

5.1 Introduction

Supernova 1987A, or SN 1987A, is one of the most famous objects in the known universe. Since its first detection on February 23, 1987, this object has fascinated scientists over the last three decades. Located at the edge of the Tarantula Nebula in the nearby Large Magellanic Cloud (LMC), only 50 kpc away from Earth, it is the nearest supernova explosion observed since SN Kepler 1604, a supernova which occurred in our own galaxy more than 400 years ago. The explosion of the progenitor star, a blue supergiant (BSG) star with a mas of $\sim 18-20\,M_{\odot}$, ocurred only about 168,000 years ago, and the supernova blazed with the power of 100 million suns for several months after its explosion. Luckily, the blast occurred in a highly-visible region of the southern sky, unobscured by dust, making it possible to be observed by naked eye, as if a new star had been born (Figure 5.1).

SN 1987A is a type II-P supernova and the light curve during the first 500 days of the photospheric phase was dominated by optical light. However, given the absence of a significant plateau phase (see Section 5.2) and the relatively faint maximum powered by radioactive decay (Fransson et al., 2007), SN 1987A is considered a peculiar supernova that defines an entirely separate class of SN type II, which likely make less than $\sim 3\%$ of all core-collapse supernovae (Smartt, 2009).

Because of its early detection and relative proximity to Earth, SN 1987A has become the best studied supernova heretofore. We have watched it evolve from a stellar explosion into a supernova remnant in unprecedented detail, using telescopes on the ground and in space.

Among the the numerous findings provided by SN 1987A, we can remark:

- The birth of extra-solar neutrino astronomy. For the first time, neutrinos from a source different to the Sun were detected, giving further support to the theory of core-collapse explosions.
- Direct observation of the progenitor star on archival photographic plates. A blue supergiant was identified as the progenitor star, contrary to expectations in which the exploding star was considered a red supergiant.
- Signatures of a non-spherical explosion and mixing in the ejecta. Classic models of spherical explosions were no longer valid.
- Direct observation of supernova nucleosynthesis, including accurate mass measures of radioactive elements such as ^{56}Ni, ^{57}Ni, and ^{44}Ti.
- Observation of the formation of dust in the supernova remnant.

However, despite all this progress, a lot of mysteries remain uncovered in SN 1987A. Large departures from spherical or even cylindrical symmetry in both the SN debris and the circumstellar matter still lack satisfactory explanations. It is known that the neutrino burst was an evidence of the core-collapse and that a compact object must be formed. That object is most likely a neutron star, but it is possible that continued infall triggered a further collapse to a black hole, although this scenario seems much less plausible. However, except for the neutrino pulse, no evidence has yet appeared for the compact object that must have formed in the core collapse. Even more mysterious is the distribution of circumstellar matter beyond the triple-ring system (Figure 5.1) detected through echoes of the SN light reflected by dust grains in interstellar space. SN 1987A has been a cornerstone for our understanding of the Universe, particulary in the field of supernova explosions. Over the last 30 years has provided us a lot of amazing discoveries, and it will surely keep doing so in the coming years...

5.1.1 SN 1987A: an exciting discovery

There was nothing special in the night of February 23-24, 1987, in Las Campanas Observatory (Chile). It was like any other. Astronomers from all over the world were preparing for another night of scheduled observations, and nothing was to indicate what was about to come. That night, astronomer Ian Shelton was observing stars in the LMC. As Shelton was studying a panoramic photographic plate taken with a 10-inch astrograph, he noticed a bright object that he initially thought was a defect in the plate. When he developed the plate he immediately noticed a bright (about 5th magnitude) star where there should not have been one. Shelton walked outside the observatory, looked into the night sky, and he saw that new misterious light by naked eye...

At about the same time, Oscar Duhalde, a telescope operator, stood outside the observatory looking that clear night sky. Suddenly, he also spotted that "new star" visually. Shelton showed the plate to other astronomers at the observatory, and then they realized the object was the light from a supernova, in fact, the brightest extragalactic supernova in history.

A third independent sighting came from Albert Jones, an amateur observer and AAVSO (American Association of Variable Star Observers) member, in Nelson, New Zealand. Jones swung his 0.3-meter telescope for a look at the three variable stars he was studying in the LMC. He noticed that there, in the same viewing field, there was a very bright blue star that did not belong. Jones got his star charts out and noted the position of the new star relative to other stars. Unfortunately, clouds rolled in before he could determine a magnitude estimate so he alerted other observers. Later, the clouds broke and Jones was able to estimate a magnitude of 5.1. Not knowing if other observers were clouded out, he continued observing the supernova for another 4 hours. His perseverance provided critical early coverage of the supernova.

The next morning, the astronomers in Chile had to notify the astronomical community of the discovery. There was not internet back in 1987, so Shelton went down the mountain to the nearest town and sent a message to the Central Bureau for Astronomical Telegrams of the International Astronomical Union (IAU), a service used to announce astronomical discoveries and keep astronomers update of the latest discoveries and developments. Shortly after the supernova was announced, news spread rapidly through the astronomical community, and literally every telescope in the southern hemisphere started observing this exciting new object. As the first supernova spotted in 1987, this one was officially named as SN 1987A. The close proximity and early detection of SN 1987A make it by far the best studied supernova in history.

5.1.2 A first sign: the neutrino burst

About 2-3 hours before the first photons from SN 1987A arrived to Earth, still on February 23, a very rare event was noticed. A "storm" of neutrinos was registered during a short ~ 13 second interval by three separate ground-based detectors. The Kamioka Nucleon Decay Experiment (Kamiokande II), lying deep in the Kamioka zinc mine under the Japanese Alps, and the Irvine-Michigan-Brookhaven detector (IMB), in the Morton-Thiokol salt mine near Fairport (Ohio, USA), are two massive pools of dark water designed to detect flashes of light from decaying protons. At 7h 35m 35s (Greenwich time) on February 23, about two hours before optical light was observed from SN 1987A, the walls of the Kamioka detector registered that 12 neutrinos had smashed into the water pool detectors and that they had penetrated the Earth from the direction of the LMC. Since the LMC is only visible from the southern hemisphere, this meant that the neutrinos passed through the Earth before they were detected.

Of the 12 neutrinos seen by Kamiokande II, 9 were spread over 2 seconds, while the remaining 3 arrived 9 to 12 seconds after the first neutrino (see Figure 5.2). At the same time, 8 more neutrinos hit the Morton-Thiokol mine. Of the 8 neutrinos seen by IMB, 6 arrived over 2.5 seconds, and 2 arrived 5 seconds after the first. A third neutrino detector, the Baksan Neutrino Observatory, located in the North Caucasus Mountains of Russia, under Mount Andyrchi, also recorded the arrival of 5 more neutrinos. Of the 5 neutrinos seen by Baksan, 3 arrived over 2 seconds while 2 arrived 8 and 9 seconds after the first. Thus, a "flare" of 25 neutrinos in total was detected almost simultaneously. This may seem like a little sum if we consider the total 10^{58} neutrinos predicted to be released from this type of supernova, but it was indeed an extraordinary finding that would mark the birth of extra-solar neutrino astronomy.

Neutrinos are elusive particles of *very* small mass and very high energy, which are produced in huge quantities in the supernova explosion of a massive star. When a massive star consumes all of its thermonuclear fuel and becomes gravitationally unstable, it collapses until the degeneracy pressure exerted by protons and neutrons halt the collapse, creating a neutron star. This sudden halt converts the kinetic energy of the core into heat that is trapped inside the neutron star. This heat is radiated out of the core as neutrinos.[1]

The number of neutrinos detected from the supernova translates into a total neutrino energy in neutrinos of $\sim 3 \times 10^{53}$ ergs, which is 16% of the rest mass energy of a 1.4 solar mass core, a value that is consistent with theory. Despite the brilliance of a core-collapse supernova, the light we see is only a tiny frac-

[1] For a deep discussion and detailed analysis of the neutrino burst and the core-collapse supernova explosions, see Arnett et al. (1989), where they review the observations made during the first two years after the discovery of the event.

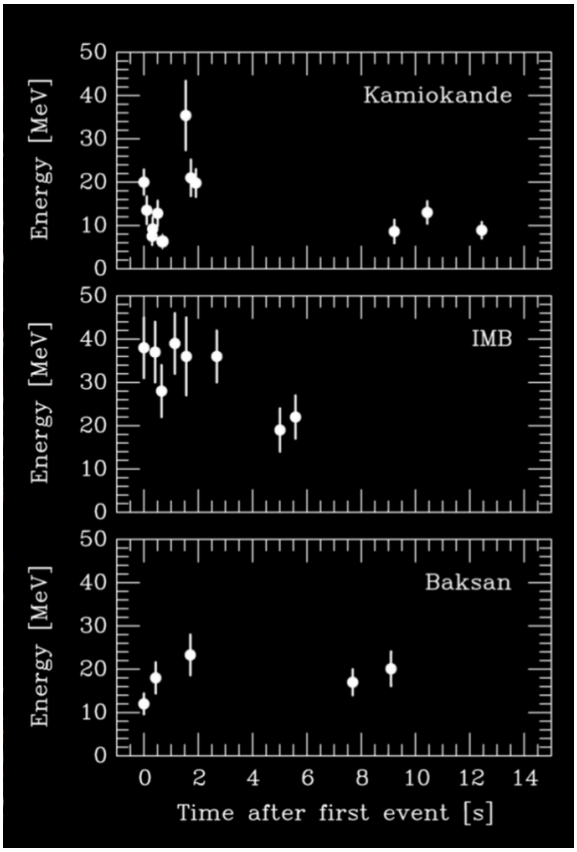

Figure 5.2: Detected neutrinos from SN 1987A at three different observatories.

tion of the total energy released in the explosion, and most of the energy escapes the exploding star as neutrinos. This was the first time neutrinos emitted from a supernova had been observed directly, and the observations were consistent with theoretical supernova models in which 99% of the energy of the collapse is radiated away in neutrinos. The fact that there was no structure in the neutrino burst indicated that they came from the collapse to a neutron star, but no further collapse to a black hole occurred. However, no signal from a compact object has been detected since the neutrino burst. On the other hand, from these observations, a maximum neutrino mass of 1/30,000 of the electron mass, as well as some other properties, could be inferred.

The first detection of neutrinos from a celestial object other than the Sun was certainly a great achievement, and in recognition for this, the japanese physicist Masatoshi Koshiba was awarded the Nobel Prize in Physics in 2002 (shared with Raymond Davis Jr. for the study of solar neutrinos and Riccardo Giacconi for X-ray astronomy).

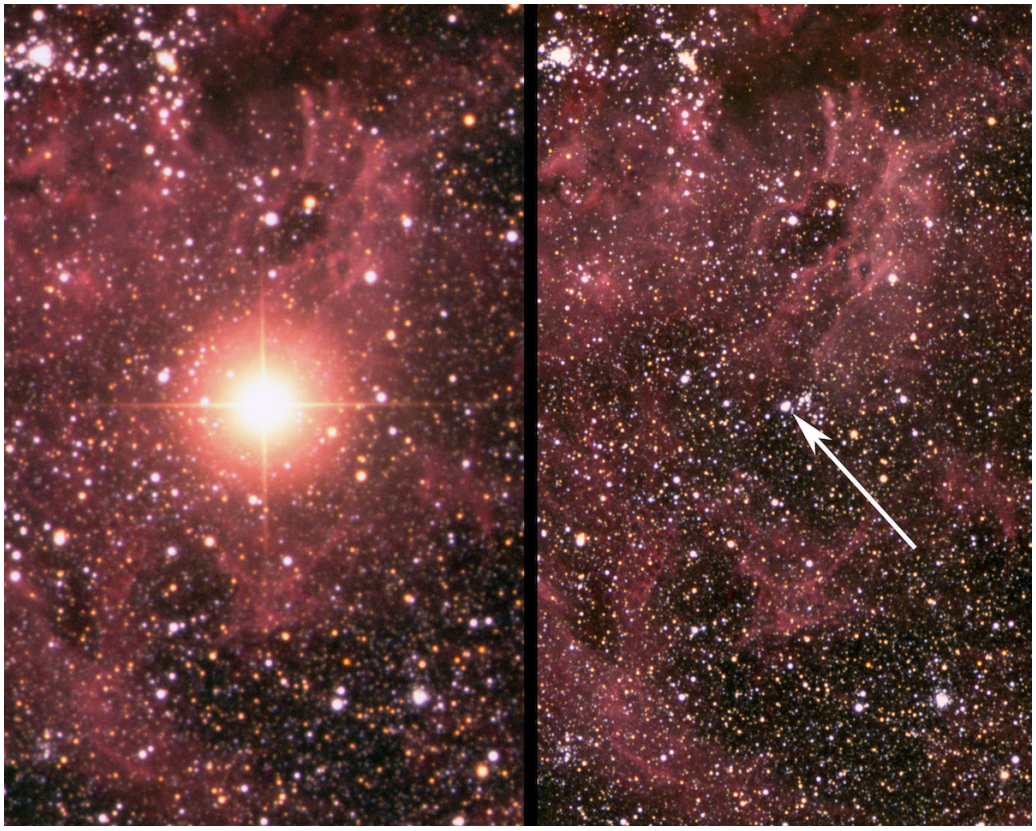

Figure 5.3: SN 1987A in the Tarantula Nebula after the explosion (left) and before the explosion (right). Credit: David Malin, Australian Astronomical Observatory (AAO).

5.1.3 The progenitor star

The day after the discovery, the astrophysicist Robert McNaught provided the first confirmation of the position of SN 1987A using the Aston Hewitt Satellite Schmidt camera at the Siding Spring Observatory (SSO, Australia). A few days later, the progenitor star was identified: it was the blue supergiant Sanduleak -69° 202 (see Figure 5.3).

Like all blue supergiants, it was a extremely luminous star, with an absolute visual magnitude of -6.3, but it was too faint to be seen with the naked eye, having at 50 kpc distance an apparent visual magnitude of 12.2, which is roughly at the limit of the largest portable telescopes. Because of its high luminosity, it was regularly observed, with the last observation occurring about 5 hours before the neutrino burst released by the supernova arrived to Earth. Three more observations were made in the following 6 hours. Subsequent observations, made less than 24

hours after the neutrino burst, finally alerted the astronomical community that a supernova had occurred. The blue supergiant increased its brightness from 12th magnitude to 6th magnitude, a factor of 250 in power radiated as visible light, in the first three hours after the neutrino burst.

Years later, once the supernova faded and the supernova shell expanded sufficiently to become transparent, astronomers confirmed that Sk -69° 202 no longer existed. The progenitor star had a mass of $\sim 18-20\ M_\odot$ (Smartt, 2009) and was spectroscopically classified as a B3 I star (Arnett et al., 1989). This was an unexpected identification, because at the time a BSG was not considered a possibility for a supernova event in existing models of high mass stellar evolution. Instead, everyone expected that the exploding star would be a red supergiant (RSG). Stars with initial masses in the range $8-25$ $M_\odot$ should end their nuclear burning lives as a RSG, i.e., with an hydrogen envelope that gives rise to the extended plateau emission. The fact that the progenitor of SN 1987A exploded as a BSG implies that the RSG evolved back to a BSG before the explosion (Woosley et al., 1988; Crotts & Heathcote, 2000). For a time, astronomers thought that Sk -69°202 might be just a foreground star and that a RSG lurked behind it. But the two-hour delay between neutrino detection and the optical outburst was consistent with the relatively small radius appropriate to a B3 I star.

5.1.4 The lady of the rings

The first images of SN 1987A taken with the ESA Faint Object Camera of the HST on August 23-24, 1990, showed an inner circumstellar ring in the supernova remnant, later known as the *equatorial ring* (ER). Nino Panagia of the Space Telescope Science Institute compared the angular size of the ring to the time delay between the supernova flash and the strongest emission from the ring. In this way, he was able to make a direct geometric measurement of the distance to the supernova (and thus the LMC), as well as an estimate of the inclination of the ring with the line of sight. The distance was 166,000 light-years with an uncertainty of 6% (Panagia et al., 1991). This independent distance determination to the LMC provided an exciting new check on determining cosmological distances.

Later in 1994, the HST revealed the existence of two fainter outer rings, which extended like mirror images in a hourglass-shaped structure (Figures 5.4 and 5.5). The outer rings were roughly coaxial with the inner ring, but not coplanar. They had radii about three times that of the inner ring and were displaced by ~ 1.3 light-years above and below the ER. This was a big surprise since at that time a typical supernova remnant was considered as a simple spherical shell centered at the point of the explosion.

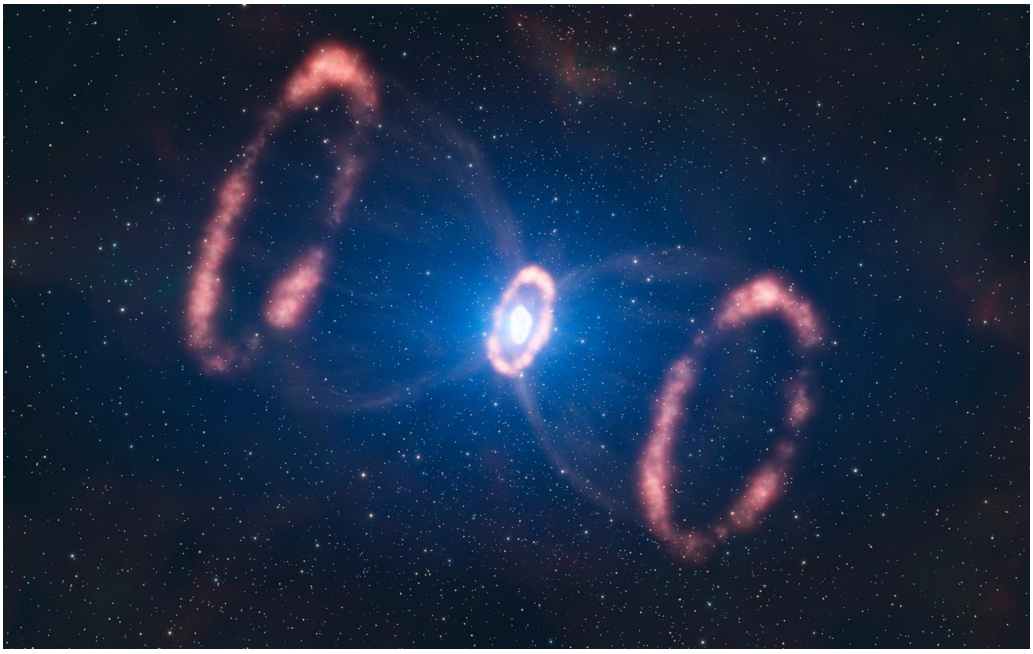

Figure 5.4: Artistic impression of SN 1987A. The image shows the different elements present in SN 1987A: two outer rings, one inner ring and the deformed, innermost expelled material. Credit: L. Calçada, ESO.[2]

We now know that the rings are inner rims of dense regions of gas from the stellar winds of the progenitor star that glow because they were ionized by the flash of extreme ultraviolet (UV) and soft X-rays that lasted a few hours after the SN blast wave emerged from the photosphere of the progenitor star. The inner ring is in the equatorial plane of the exploding star, has a radius of 0.8 arcsec (~ 0.6 ly), and is inclined by about 43° with the northern part closer to us (Jakobsen et al., 1991; Tziamtzis et al., 2011). The ring is expanding with a radial velocity of ~ 10.3 km s^{-1}. Thus, assuming a constant expansion velocity, it is easy to infer that the gas in the ring was expelled by the progenitor star about 20,000 years before the explosion.

Even today, the origin of these rings is still a mystery, and a variety of explanations have been proposed. Rapid rotation of a single star, or powerful magnetic fields could have directed gas from an eruption into a loop around the progenitor star. Morris & Podsiadlowski (2007, 2009) presented three-dimensional hydrodynamical simulations in which the mass ejection associated with a merger of two massive stars reproduced the properties of the triple-ring nebula surrounding the supernova (Figure 5.5).

[2] https://www.eso.org/public/unitedkingdom/images/eso1032a/?lang

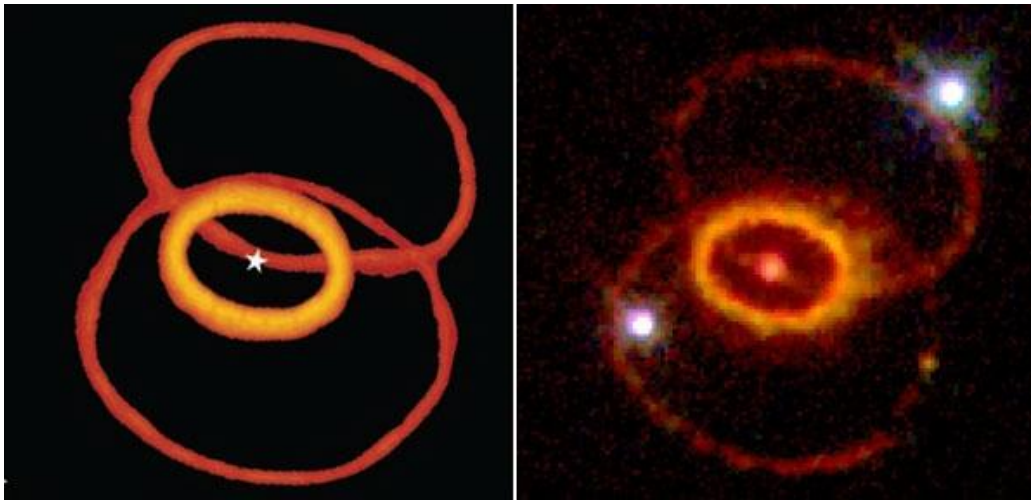

Figure 5.5: *Left*: Rings produced by a computer model of a stellar merger. Credit: Morris & Podsiadlowski (2007). *Right*: The SN 1987A triple-ring structure imaged with the HST in 1994. The rings are dense regions in the stellar wind that were ionized by ultraviolet radiation from the supernova. The supernova remnant is the bright dot at the center. The two bright stars in the top-right and bottom-left are not associated with the supernova. Credit: C. Burrows (ESA/ STScI), HST, NASA.[3]

However, although the merger scenario appears as a plausible explanation for the origin of the triple-ring system, the matter is not yet fully understood.

[3]This image was the Astronomy Picture of the Day (APOD) on July 5, 1996. `https://apod.nasa.gov/apod/ap960705.html`

5.2 Light curve and evolution[4]

A detailed analysis of the SN light curve (Figure 5.6) and the evolution of the remnant is made in this section. The dates given should be considered as approximate dates as they sometimes depend on the consulted bibliography. In Figure 5.7 some of the most relevant events after the first 10,000 days after the supernova explosion are outlined.

- Day $0-30$: About four weeks after the explosion, the supernova light curve was powered by the radioactive decay of freshly synthesized ^{56}Ni ($t_{56} = 111.3$ days). The total amount of ^{56}Ni mass was estimated to be $0.069 \pm 0.003\ M_{\odot}$(Bouchet et al., 1991; McCray & Fransson, 2016) and the radioactive decay chain $^{56}\text{Ni} \rightarrow {}^{56}\text{Co} \rightarrow {}^{56}\text{Fe}$ deposited energy in the debris until about 500 days. One month after the explosion, using images reconstructed through speckle interferometry, it was detected a source of optical emission displaced from the supernova center by 0.06 arcsec (Nisenson et al., 1987). The nature of this so-called "mystery spot" remains unclear, but it was a strong indication of broken symmetry, which was also detected in polarization observations.

- Day ~ 80: About 80 days after explosion, ultraviolet (e.g., NV , NIV], NIII], CV , CIII], HeII) and optical (e.g., Hα) lines were detected. These lines could not possibly come from the fast moving ejecta and were quickly recognized as originating from material outside the supernova, which was ionized by the soft X-rays from the shock breakout. A temperature of $\sim 10^6$ K at the shock breakout could be estimated from the high ionization of these lines.

- Day $100-200$: Only a few months after the explosion, vibrational lines of CO and SiO were detected. Analysis of these bands (Liu et al., 1992; Liu & Dalgarno, 1994) indicated that these molecules had masses $\text{M}_{\text{CO}} = 10^{-3}\ M_{\odot}$ (Liu et al., 1992) and $\text{M}_{\text{SiO}} = 10^{-3}\ M_{\odot}$ (Liu & Dalgarno, 1994), respectively. Furthermore, when first detected, at $t = 192$ days, the CO had a temperature $\text{T}_{\text{CO}} = 4000$ K, which dropped to $\text{T}_{\text{CO}} = 1800$ K at $t = 377$ days. The presence of these molecules within the ejecta was difficult to explain. The formation of molecules required that they be protected from the UV and X-rays in the harsh environment of the ejecta.

[4]Most of the content presented in the following sections has been extracted from Fransson & Kozma (2002), Kjær (2007), Fransson et al. (2007), Larsson et al. (2011), Zanardo (2014), McCray & Fransson (2016), and Spyromilio et al. (2017).

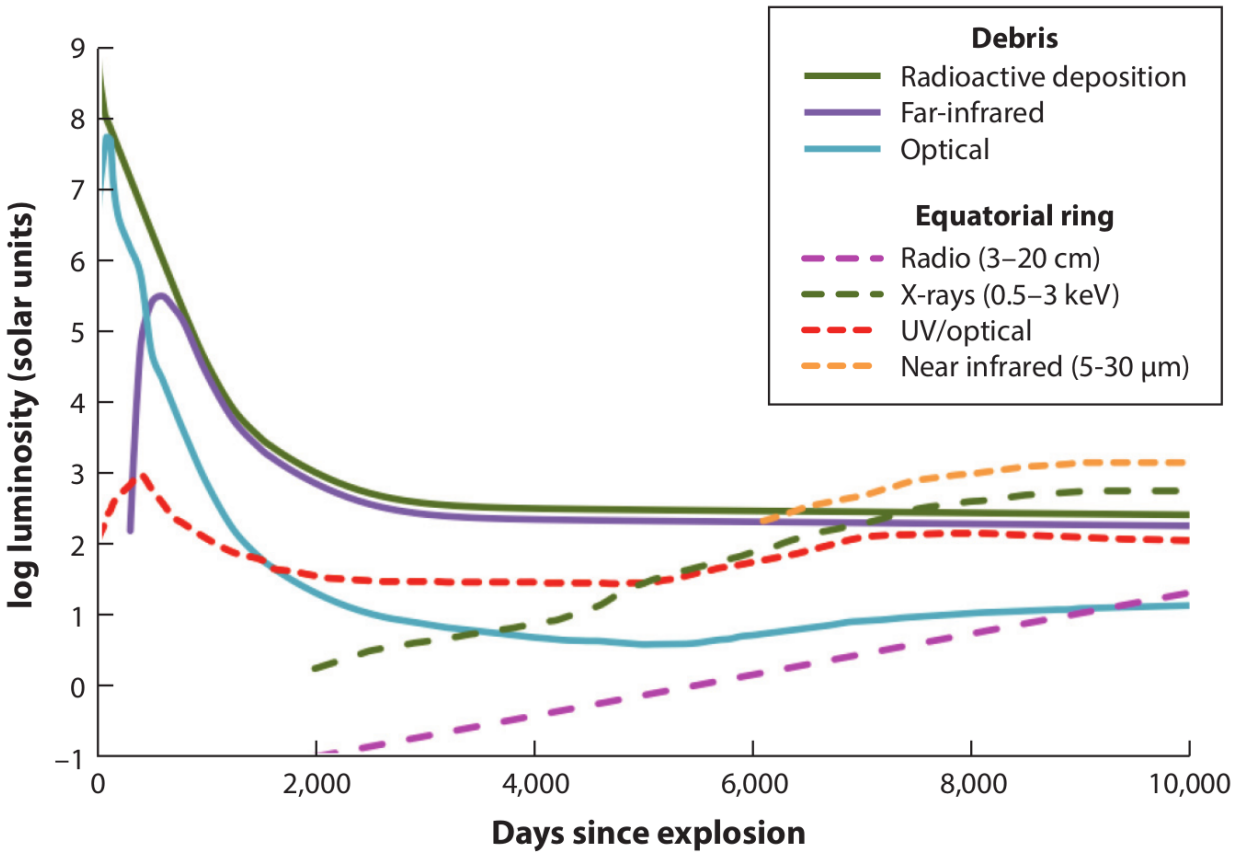

Figure 5.6: SN 1987A light curves. Solid curves are debris: green, radioactive deposition (Fransson & Kozma, 2002; Jerkstrand et al., 2011; Boggs et al., 2015); violet, far-IR (McCray, 1993; Matsuura et al., 2015); and cyan, optical (McCray, 1993; Larsson et al., 2011; Jerkstrand et al., 2011). Dashed curves are the equatorial ring: pink, radio (3-20 cm) (Manchester et al., 2002; Zanardo et al., 2010, 2014; Ng et al., 2013); green, X-rays (0.5 – 3 keV) (Hasinger et al., 1996; Burrows et al., 2000; Frank et al., 2016); red, UV/optical (Lundqvist & Fransson, 1991; Matilla et al., 2010; Fransson et al., 2015); and gold, near-IR (5 – 30 μm) (Dwek et al., 2008, 2010). Credit: McCray & Fransson (2016).

This also contrasted with the observations of the characteristic γ-rays at 847 keV and 1.238 MeV from the ^{56}Co decay. The X-rays from Compton scattering of the γ-rays and their emission peaked after about 200 days and slowly declined thereafter as the number of ^{56}Co nuclei decayed away. The appearance of X-rays and gamma rays earlier than predicted indicated that some of the newly synthesized ^{56}Co had penetrated into the hydrogen outer layer of the ejecta (McCray, 1993). The presence of molecules was a clear sign that there were regions which could cool down significantly, while at the same time the radioactive material from the core had to be transported towards the surface to become observable. Evidence for large-scale asymmetry in the ejecta also emerged within a few months of the explosion. Fine structure appeared in the profile of Hα (Hanuschik & Thimm, 1990), indicating inhomogeneities in the emission by hydrogen expanding with velocities ~ 4500 km s^{-1}. This phenomenon, known as the "Bochum event", was the signature of a radioactive blob rising from the inner ejecta to the surface.

- Day $400-500$: At about 400 days after the explosion, the luminosity of the ring (Figure 5.6) increased to a maximum (Fransson et al., 1989; Sonneborn et al., 1997), which is the time when the ionizing flash illuminated the side of the ring furthest from the observer. Thereafter, the luminosity faded owing to recombination and radiative cooling. For the first 500 days the bolometric light curve was dominated by optical light and the spectrum was thermally dominated.

- Day ~ 500: A crucial change occurred in the light curve and spectrum of the remnant at about 500 days after the explosion. The optical light rapidly dropped below the ^{56}Co decay luminosity while a far-infrared (FIR) continuum appeared. The combined luminosities of the optical light, the FIR continuum, and the escaping γ-rays continued to track the exponential decay of ^{56}Co. This change was due to the formation of dust grains within the debris, which absorbed the optical and near-infrared (NIR) radiation. The dust grains had a temperature of ~ 600 K (McCray, 1993). Thus, infrared wavelengths gained in importance as more and more radiation was emitted at longer wavelengths. The bolometric light curve started to become dominated by long-wavelength radiation and the inclusion of this spectral range became more and more important. The ^{56}Ni $\rightarrow$ ^{56}Co $\rightarrow$ ^{56}Fe decay chain could be observed directly in the changing line ratios of the NIR Co and Fe lines. At the same time the NIR [Fe II] lines dropped dramatically as the ejecta cooled below the temperature to excite these lines, a signature of the infrared catastrophe predicted by modelers (Spyromilio & Gra-

ham, 1992). Macroscopic dust grains which partially covered the ejecta, and hence blocked some of the light, had formed. The radiation was absorbed in the optical spectrum and shifted to the FIR.

- Day $\sim 1000-2000$: After about ~ 1100 days after the explosion, the main energy input to the supernova ejecta came from radioactive decay of long-lived ^{57}Co as predicted by Pinto et al. (1988), Woosley et al. (1989) and Hashimoto et al. (1989).

- Day ~ 1200: After about 1200 days the decline of the light curve started to slow down because of the ^{57}Co ($\sim 0.001\ M_{\odot}$). The time scale for recombination and cooling in the supernova envelope became comparable to the expansion time scale, i.e., some of the "stored" energy was finally released. This was called "freeze-out" as the ejecta were no longer in thermal equilibrium and detailed time-dependent calculations had to be performed.

- Day $\gtrsim 2000$: After about $7-8$ years after the explosion the energy input of the supernova became dominated by the decay of ^{44}Ti ($t_{44} = 85$ years). The radioactive energy was deposited in the debris by fast (596 keV) positrons from the prompt decay of ^{44}Sc, which decays from the ^{44}Ti. The ^{44}Ti mass of $M_{44} = 10^{-4}\ M_{\odot}$ estimated by Woosley et al. (1989) and Hashimoto et al. (1989) was confirmed with the detection by the INTEGRAL (Grebenev et al., 2012) and NuSTAR (Boggs et al., 2015) observatories of 67.9 keV and 78.4 keV hard X-ray lines, respectively, emitted as a result of the decay of ^{44}Ti. The mass of ^{44}Ti inferred from the NuSTAR observation was $M_{44} = (1.5 \pm 0.3) \times 10^{-4}\ M_{\odot}$, which is significantly less than the value $M_{44} = (3.1 \pm 0.8) \times 10^{-4}\ M_{\odot}$, inferred from the earlier INTEGRAL observation. Combining Very Large Telescope (VLT) and HST spectra with time-dependent non-local thermodynamic equilibrium (non-LTE) radiative transfer calculations, Jerkstrand et al. (2011) estimated a ^{44}Ti mass of $M_{44} = (1.5 \pm 0.5) \times 10^{-4}\ M_{\odot}$, which is also consistent with the NuSTAR observation.

- Day ~ 2900: About 8 years after the explosion, the first "hot spot" appeared in the ring (Sonneborn et al., 1998; Lawrence et al., 2000). X-ray spectra obtained with Chandra provided evidence that the optical hot spots and the X-ray producing gas were due to a collision of the outward-moving supernova shock wave with dense fingers of cool gas protruding inward from the circumstellar ring. These fingers were produced long ago by the interaction of the high-speed wind with the dense circumstellar cloud.

- Day $\sim$ 5000: A new phase in the energy budget started at about day 5000. Up to this epoch the luminosity of the ejecta had decreased slowly owing to the ^{44}Ti decay. Photometry in the R and B bands with HST, however, showed that after this epoch the luminosity increased steadily by a factor of $3-4$ at $10,000$ days (Larsson et al., 2011). Evidently, X-rays from the ring interaction absorbed and thermalized by the ejecta now contributed more to the optical luminosity than the ^{44}Ti decay. Adding up the radioactive contribution and a fraction of $\sim 5\%$ of the X-ray luminosity yields a qualitative agreement with the optical light curves. This change may be regarded as marking a transition to the remnant phase, when the luminosity is dominated by interaction rather than radioactive input. At the same time the optical morphology changed from centrally dominated emission to a horseshoe-like shape (Fransson et al., 2013). One finds that X-rays with energy of 2 keV can penetrate into the metal core of the ejecta. At this point, the photoelectric absorption by the metals becomes large enough to shield most of the core from the X-rays. It is therefore mainly the hydrogen and helium envelope that is affected by the X-rays. This accounts for the change of morphology of the ejecta in the X-ray-dominated phase.

- Day $\sim$ 8500: In 2010 the Herschel satellite observed the supernova in the FIR and detected an enormous excess of emission longward of 100 μm (Matsuura et al., 2011). Contemporaneously, Lakićević et al. (2012) used APEX to detect emission from the supernova at 300 and 870 μm. Combining the flux with models of dust, Matsuura et al. (2011) concluded that between 0.1 and 1 $M_{\odot}$ of dust formed in the supernova.

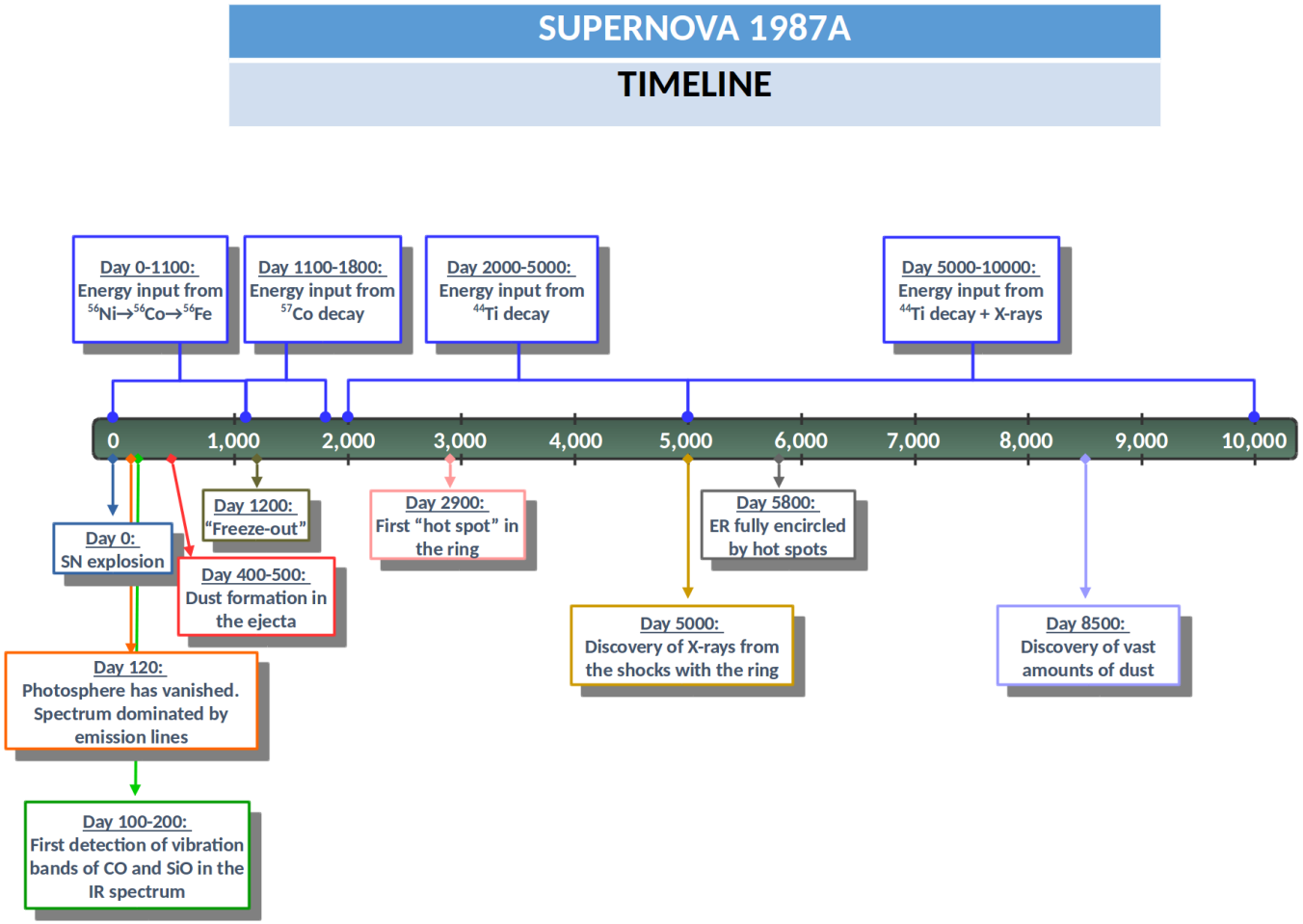

Figure 5.7: Evolution timeline of SN 1987A for the first 10,000 days.

5.3 Emission sites

Figure 5.8 shows two distinct illustrations of the different emission sites of SN 1987A. An explanation of these illustrations based on the color scheme from the figure at the top is given here, although the same description with very similar colors is also valid for the figure at the bottom. The innermost part (blue) represents the cool ejecta, with the nucleosynthesis products and the internal dust. They are surrounded by the freely expanding outer envelope of the SN composed mostly of hydrogen and helium. This envelope is suddenly decelerated at a reverse shock (the blue-dark yellow interface) where the gas is heated to temperatures of $\sim 10^6 - 10^7$ K (yellow). The shocked envelope drives a forward shock or blast wave (bright yellow) into the ER (red), which consists of slowly expanding gas that was photoionized by the ionizing flash from the initial SN shock breakout, and by fingers of relatively dense and cool gas (white). As the blast wave overtakes these "hot fingers", transmitted shocks give rise to soft X-ray and optical emission, manifested as hot spots, while reflected shocks heat and compress the debris further and give rise to a higher temperature component of X-ray emission.

As it is clear from Figure 5.8, the supernova remnant consists of various emission sites with different emission mechanisms. We explain in the following the main emission sites: the ejecta, the ring, and the shocks.

5.3.1 The ejecta

In the center of the equatorial ring sit the inner ejecta, i.e., the visible remains of the supernova itself (see Figure 5.8). Due to the radioactive decay of ^{44}Ti, the ejecta have faded since the explosion time through 2001 (day $\sim$ 5000, see Figure 5.7). It then started to brighten again, as the result of X-ray heating via the interaction with the reverse and reflected/inbound SN shocks (Larsson et al., 2011). These X-rays are mainly absorbed in the hydrogen rich envelope while the metal core is still powered by decay of ^{44}Ti. The equatorial ring optical emission has become increasingly brighter, and the ring has been outshining the ejecta since $\sim$ 1998, with emission sites being brighter on the western side. The inner ejecta have been expanding at $\sim 2000 - 3500$ km s^{-1}(Kjær et al., 2010; Larsson et al., 2013) and changing shape over time. The ejecta shape is not only determined by the distribution of radioactively heated inner debris, but also by the distribution of interior dust clouds, which likely obscure most of the actual optical and NIR emission (McCray, 2007).

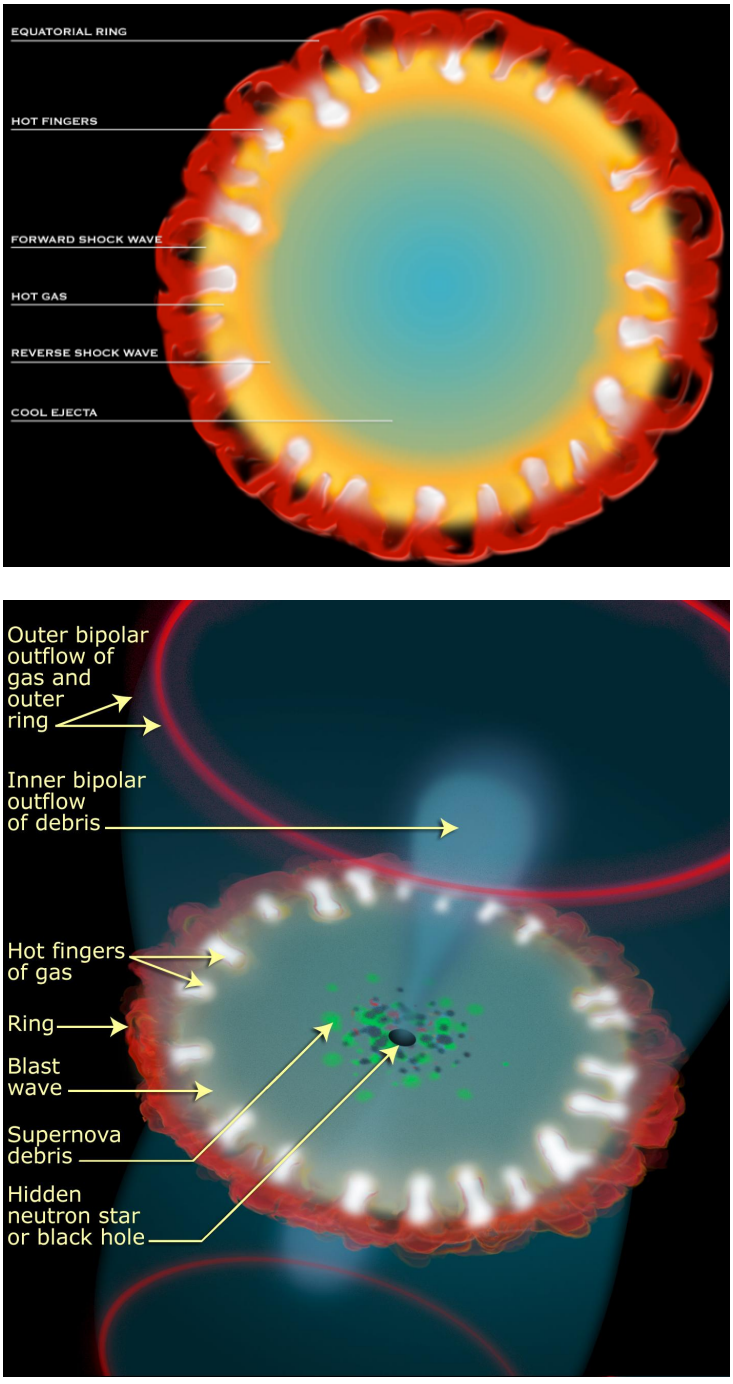

Figure 5.8: Illustration of the emission sites of SN 1987A. Credits: (top) NASA/CXC/M.Weiss; (bottom) NASA, ESA and A. Feild (STScI).[5]

[5] http://hubblesite.org/newscenter/archive/releases/2007/10/image/i/

The ejecta optical morphology has evolved from a roughly elliptical shape up to day $\sim$ 5000, to an irregular north-south elongated shape (Kjær et al., 2010; Larsson et al., 2013), mostly extended along PA $\sim$ 15 $^{\circ}$, with a "hole" in the middle (Larsson et al., 2011), which has been interpreted as a high-density region filled with non-H emitting material (Larsson et al., 2013). Both the ejecta elongation and velocity asymmetry in the Hα emission point to a non-spherical anisotropic distribution of the supernova debris and, thus, to a non-symmetric explosion mechanism (Kjær et al., 2010). The H and He-rich ejecta has been expanding above and below the equatorial ring plane (Fransson et al., 2013), while, consistently with the inclination of the equatorial ring, the Hα and [Si I]+[Fe II] emission from the northern parts is blueshifted and appears more redshifted in the southern sites (Larsson et al., 2013).

5.3.2 The equatorial ring

Surrounding the inner ejecta, the equatorial ring shines as a result of the shocked gas. When the fastest ejecta, moving at $\sim$ 10% of the speed of light, reached the ring, the shocked gas started to emit brightly at wavelengths ranging from radio to X-ray. We now know, from observations of the impact of the blast wave with the ring, that the ring is not uniform, but consists of some thirty hotspots of high-density gas protruding inward from a substrate of lower density gas. The ring was illuminated by the ionizing flash, and hence most of the narrow line emission comes from the hotspots. Recently, observations from HST have been used to show that the ring is beginning to suffer from the effects of the ejecta colliding into it (Fransson et al., 2015), and starting to be destroyed. A simple extrapolation estimates that this destruction process will be completed by $\sim$ 2025. However, new spots of emission outside the ring have appeared and continued observations may yet provide surprises about the surrounding structure.

We will have a splendid opportunity to watch in real time how a shock wave with well-defined characteristics impinges and reveals a hidden structure (both in density and composition).

5.3.3 The shocks

Early models of Type II SNRs (e.g., Chevalier, 1982) show that when the supernova shock wave expands into the circumstellar material a double shock structure forms, consisting of a *forward shock*, which propagates outward into the circumstellar gas (also known as *blast wave* or *shock front*), and a *reverse shock*, which is formed by the supernova ejecta hitting the decelerated medium behind the forward shock. While the forward shock moves through the ring accelerating the

ring material, the reverse shock is formed against slower and denser regions of the supernova ejecta (see Figure 5.8). Between the two shocks, reflected shocks form due to the forward and reverse shocks colliding with the dense circumstellar material.

5.4 Dust and molecules

5.4.1 Dust emission

The Spitzer Space Telescope observed the supernova out to 30 μm and detected the presence of warm dust. Observations with the Gemini South telescope and the VLT in the 10 μm band showed that the thermal infrared emission comes from the equatorial ring. As mentioned in Section 5.2, in 2010 Herschel detected a huge excess of emission longward of 100 μm (Matsuura et al., 2011). Lakićević et al. (2012) used APEX to detect emission at 300 and 870 μm. Combining the flux with models of dust, Matsuura et al. (2011) finally concluded that between 0.1 and 1 $M_\odot$ of dust formed in the supernova. Given the angular resolution of Spitzer and Herschel, the location of the cold dust remained uncertain. Observations in 2013 with ALMA at 1 mm and 450 μm at an angular resolution of ~ 0.5 arcseconds proved the unambiguous association of the cold dust with the inner ejecta of 1987A (see Figure 5 in Indebetouw et al., 2014). The mass estimate of the dust, however, remains "stubbornly high", above 0.5 $M_\odot$ (Matsuura et al., 2015). If the dust were to survive its pass through the reverse shock, then core-collapse supernovae might be a significant contributor to the dust budget in the early Universe.

5.4.2 Molecular emission

The ALMA spectra provided further research excitement because, in addition to the dust observations, they revealed strong molecular emission from CO $2-1$ and SiO $5-4$ transitions. Combined with a detection by Herschel of the CO $6-5$ and $7-6$ transitions, the temperature and mass determination could be refined by Kamenetzky et al. (2013). They found the temperature of the CO to be likely < 100 K. It follows that the mean molecular velocity of the emitting gas, $c_S \sim (kT/\mu)^{1/2} < 0.2$ km s^{-1}, is far less than the typical expansion velocity of the debris, the emission lines of which have FWHM ~ 2000 km s^{-1}. The Doppler shift enables one to infer the structure of the debris in three dimensions from observations of images of emission lines.

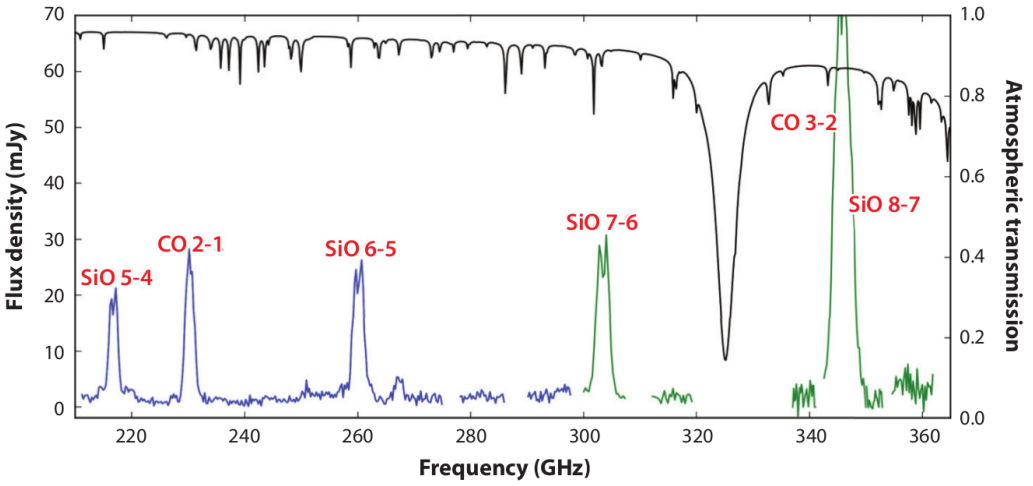

Figure 5.9: ALMA spectrum of SN 1987A showing bright emission lines from CO ($J = 2-1$), SiO ($J = 5-4, 6-5, 7-6$), and a blend of CO ($J = 3-2$) and SiO ($J = 8-7$). Note central dips in SiO profiles, which are not prominent in CO profiles. The black curve denotes typical atmospheric transmission at the ALMA site. Credit: SN 1987A ALMA collaboration.

A good example of this technique was provided by Kjær et al. (2010) and Larsson et al. (2013), who mapped the debris with the SINFONI (Spectrograph for INtegral Field Observations in the Near Infrared) instrument of the VLT. With the commissioning of the ALMA, we have a new window on the inner debris. Unlike optical or NIR radiation, millimeter/submillimeter radiation is not absorbed by dust grains. Kamenetzky et al. (2013) observed SN 1987A in early science observations with a partial ($14-18$ dishes) array in a compact (400m maximum baseline) configuration and found surprisingly strong emission lines from rotational transitions of CO ($1-0$, $2-1$, and $3-2$) and SiO ($5-4$, $6-5$, $7-6$, and $8-7$) (see Figure 5.9).

They found that the CO has a minimum mass $M_{CO} > 0.01\ M_{\odot}$ and temperature $T_{CO} = 10-100$ K. This mass is at least an order of magnitude greater than that inferred from the vibrational lines during the first years, $\sim 10^{-3}\ M_{\odot}$(Liu et al., 1992). However, it remains to be seen whether this is the same CO that was detected at 2000 K and 2000 km s^{-1} during the first year of the supernova or represents newly formed CO.

Even without resolving the debris, observations with the ALMA already gave us evidence that the spatial distribution of SiO differs from that of CO. The line profiles are different. Moreover, the SiO line profiles have a "dip" at their centers. This was clear evidence for departure from spherical symmetry in the distribution of SiO. The ALMA early science observations had angular resolution of ~ 1 arc-

sec, which was sufficient to demonstrate that the CO emission originates in the inner debris of SN 1987A, but not sufficient to resolve the debris.

Now, with the array operating at its maximum baseline, ALMA has been able to resolve the CO $(2-1)$ and SiO $(5-4,\ 6-5)$ emission with angular resolution of ~ 0.04 arcsec, which is comparable with the HST. With that resolution, ALMA has seen the kind of structure in the debris predicted in 3D hydrodynamic simulations of supernova explosions (see Chapter 6).

5.5 Hydrodynamical models

The computational modeling of supernova explosions has experienced enormous progress over the last decades with improved numerical methods, input physics, computational accuracy, and dimensionality. The simulations were initially performed in spherical symmetry (1D), then since the 90's also in two dimensions (2D), and in recent years in full 3D. However, despite many generations of ever improving simulations, the physical processes that cause the explosion are not yet fully understood (see Janka, 2012; Burrows, 2013; Janka et al., 2016, for recent reviews).

For the vast majority of normal core-collapse SNe (CCSNe) the delayed neutrino-driven mechanism (Wilson, 1985; Bethe & Wilson, 1985) is widely considered as the most likely explanation. Current state-of-the-art simulations of neutrino-driven CCSNe explosions predict that hydrodynamic instabilities play a crucial role that leads to the ejection of the stellar mantle and envelope of exploding massive stars (e.g., Janka, 2012). 3D simulations have also achieved to follow neutrino-driven explosions continuously from the initiation of the blast wave, through the shock breakout from the progenitor surface, into the radioactively powered evolution of the SN, and towards the free expansion phase of the emerging remnant.

In particular, Hammer et al. (2010) and Wongwathanarat et al. (2015) have made 3D calculations from the core collapse up to the shock breakout. The authors of the latter paper find that the initial structure is significantly affected by the reverse shock and by the asymmetries resulting from the neutrino heating (see Figure 5.10). These authors also find that the structure is sensitive to whether the progenitor is a compact BSG, like that of SN 1987A, or a RSG. In the former case, they also find significant differences between a 15 $M_\odot$ and a 20 $M_\odot$ progenitor, which is probably related to the different density gradients in the inner core. Their models are only calculated up to less than a day and do not include the heating from the ^{56}Ni decay, which may appreciably change the hydrodynamic structure (e.g., Woosley et al., 1988; Herant & Benz, 1991).

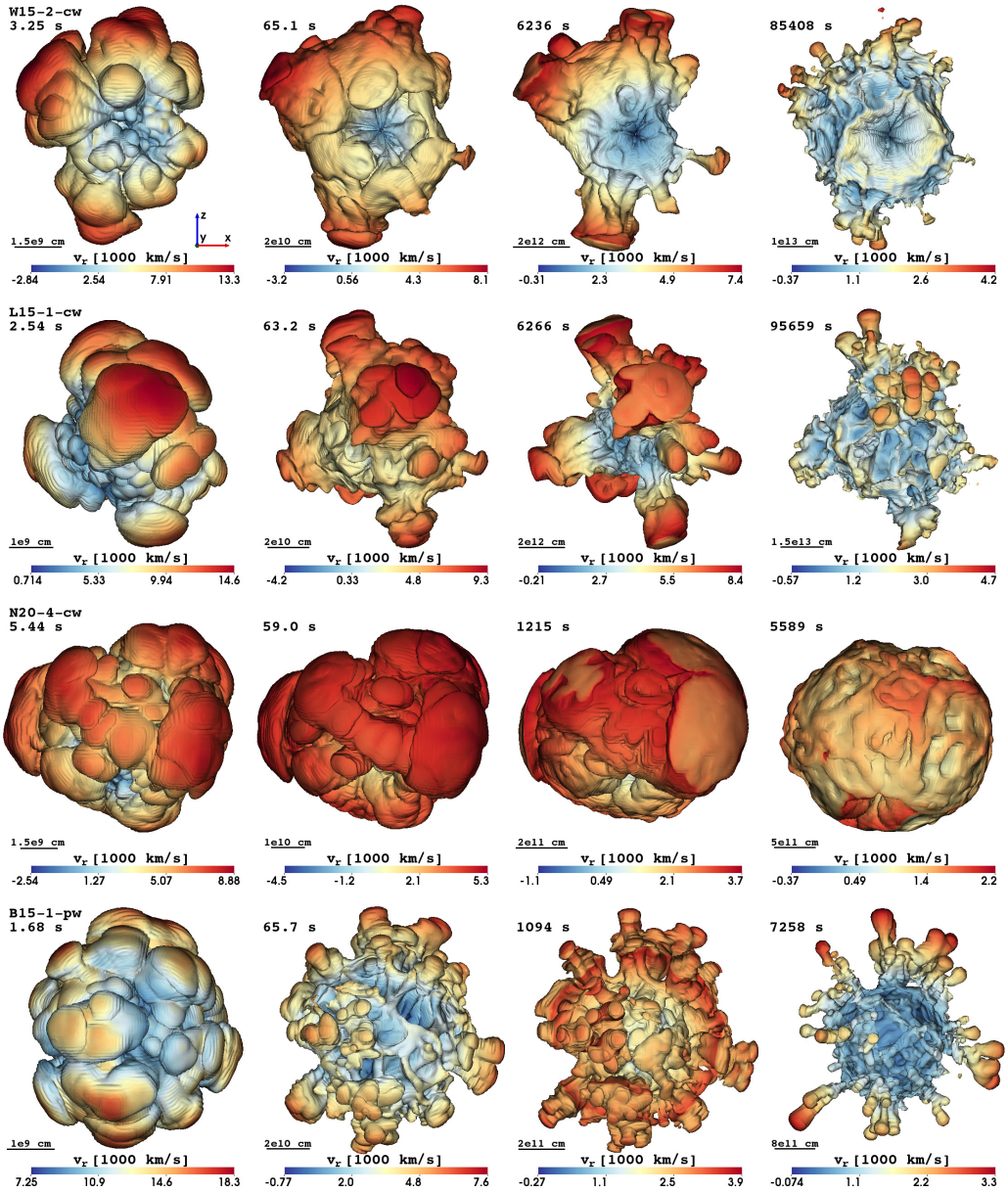

Figure 5.10: Isocontours of the ^{56}Ni distribution for model W15 (top row), L15 (second row), N20 (third row), and B15 (bottom row). The isosurfaces, which roughly coincide with the outermost edge of the neutrino-heated ejecta, are shown at four different epochs starting from shortly before the SN shock crosses the C+O/He composition interface in the progenitor star until the shock breakout time. The colors give the radial velocity (in units of km s^{-1}) on the isosurface, with the color coding defined at the bottom of each panel. In the top left corner of each panel it is shown the post-bounce time of the snapshot and in the bottom left corner a yardstick indicating the length scale. The negative y-axis is pointing toward the reader. Distinct differences in the final morphology of the nickel-rich ejecta of all models, which arise from their specific progenitor structures, are noticeable. Credit: Wongwathanarat et al. (2015).

Direct comparisons of simulations with observations of SNe and SNRs in order to derive constraints on the explosion mechanism have been already performed. As an example, it has been shown that predictions based on hydrodynamic instabilities and mixing processes associated with neutrino-driven explosions yield good agreement with measured neutron star (NS) kicks, light-curve properties of SN 1987A and asymmetries of iron and ^{44}Ti distributions observed in SN 1987A (Janka et al., 2017).

One of the observational probes of the explosion mechanism is the distribution of abundant elements, like C, O, and Si, as well as the morphology of the ejecta. In order to better constrain the explosion physics, we compare in the next chapter the first 3D maps of CO/SiO of SN 1987A from ALMA observations with the explosion models presented in Wongwathanarat et al. (2015). Their simulations covered the evolution only from $11-15$ ms to $1.1-1.4$ s after core bounce. In our case, the ^{56}Ni heating has been also included in the comparison in order to follow the simulations up to about 150 days.

The explosion models considered are W15, L15, N20, and B15. W15 denotes the 15 $M_\odot$ RSG model s15s7b2 of Woosley & Weaver (1995), L15 a 15 $M_\odot$ RSG model evolved by Limongi et al. (2000), N20 a 20 $M_\odot$ BSG progenitor model for SN 1987A by Shigeyama & Nomoto (1990), and B15 a corresponding 15 $M_\odot$ BSG model by Woosley et al. (1988). The BSG models have a shallower density profile at the H/He interface than the RSG models and differ significantly in the C+O core mass (N20 $\sim 3.8\,M_\odot$ versus B15 $\sim 1.7\,M_\odot$).

Chapter 6

Tomography of the SN 1987A ejecta

Science is built up of facts, as a house is with stones. But a collection of facts is no more a science than a heap of stones is a house.

Henri Poincaré

This chapter essentially contains what appeared published in The Astrophysical Journal Letters, 842, L24 (2017), entitled *Very Deep Inside the SN 1987A Core Ejecta: Molecular Structures Seen in 3D*.

Abstract

Most massive stars end their lives in core-collapse supernova explosions and enrich the interstellar medium with explosively nucleosynthesized elements. Following core collapse, the explosion is subject to instabilities as the shock propagates outwards through the progenitor star. Observations of the composition and structure of the innermost regions of a core-collapse supernova provide a direct probe of the instabilities and nucleosynthetic products. SN 1987A in the Large Magellanic Cloud (LMC) is the only supernova for which the inner ejecta can be spatially resolved before it is affected by interaction with the surroundings. Our observations of SN 1987A with the Atacama Large Millimeter/submillimeter Array (ALMA) are of the highest resolution to date and reveal the detailed morphology of cold molecular gas in the innermost regions of the remnant. We have determined the 3D distributions of the emission of carbon monoxide (CO) and silicon monoxide (SiO). The 3D distributions differ, but both have a central deficit, or torus-like distribution, possibly a result of radioactive heating during the first weeks ("nickel heating"). The size scales of the clumpy distribution are compared quantitatively to models, demonstrating how progenitor and explosion physics can be constrained.

6.1 Introduction

Supernova 1987A in the LMC has provided an excellent laboratory for supernova physics. Its short distance (50 kpc) has provided the very rare opportunity to spatially resolve the supernova as it evolves (currently the outer shock is greater than $1''$ or ~ 1 light-year in diameter). The environment of the ejecta of SN 1987A consists of a thin dense circumstellar ring, the *equatorial ring*, that is tilted 43° from the line of sight (Jakobsen et al., 1991; Tziamtzis et al., 2011). The first evidence of interaction of the outermost ejecta with the equatorial ring appeared in 1995 (Sonneborn et al., 1998; Lawrence et al., 2000), and was followed by the emergence of hotspots along the equatorial ring in the following years. These shocks and the reverse shock have provided much of the energy for the recent electromagnetic display from the supernova, as the decay of the radioactive energy sources produced in explosive nucleosynthesis provides ever decreasing amounts of energy.

At present, the ejecta emission at optical wavelengths is dominated by gas illuminated by the X-ray radiation from the ring (Larsson et al., 2011; Fransson et al., 2013). Our view of the inner debris where most of the nucleosynthesis products reside is highly obscured at optical/near-infrared by a massive cloud of dust grains (Matsuura et al., 2015; McCray & Fransson, 2016).

By contrast, millimeter molecular emission originates in the cold innermost ejecta and is free of the obscuration, thus being particularly powerful for understanding the details of elemental distribution and mixing.

Elements in the ejecta material are not simply radially stratified as might be expected from stellar evolution. Theory suggests that instabilities mixed the stellar nucleosynthetic products into a clumpy 3D structure. These began during the neutrino-driven phase of the explosion by convective overturn (Burrows et al., 1995) and/or standing accretion shock instability (SASI, Blondin et al., 2003), and grew by Rayleigh-Taylor instabilities as the shock propagated outwards through the progenitor during the first $\sim 10^4$ s (Ebisuzaki et al., 1989; Benz & Thielemann, 1990). During the next days, radioactive decay of ^{56}Ni$\rightarrow^{56}$Co$\rightarrow^{56}$Fe heats clumps rich in those heavy elements, causing some additional expansion of those clumps. If the process is sufficiently important, a large-scale reduction of heavy products from the central regions and lowest velocities may occur ("nickel heating", Woosley et al., 1988; Herant & Benz, 1991, 1992; Basko, 1994). After the first few days, this structure was frozen in homologous free expansion, a record that can be analyzed long afterwards.

Early detection of hard X-rays and the smooth shape of the light curve provided observational evidence that freshly synthesized material from the core of the supernova had found its way to the outer, less optically thick, regions of the envelope (Arnett et al., 1989; McCray, 1993). Observations of the structure of atomic emission lines (Haas et al., 1990; Spyromilio et al., 1990) also suggested that such macroscopic mixing of the ejecta had taken place. Detailed spectral modeling (McCray, 1993, and references therein), however, placed limits on the microscopic elemental mixing. Adiabatic expansion and radiative cooling caused temperatures to drop rapidly and allowed molecules to form where different atoms coexist. The molecular excitation temperature of $20-170$ K (Kamenetzky et al., 2013; Matsuura et al., 2017) reflects the balance between this cooling and heating due to the gamma rays and leaking positrons from the ^{44}Ti decay, and possible X-rays and UV emission from the ring. Vibrational emission of CO and SiO was observed within the first 2 years (Rank et al., 1988; Spyromilio et al., 1988; Roche et al., 1991), and provided further constraints on the amount of mixing.

However, none of these observations spatially resolved the heterogeneous ejecta. Modest angular resolution (~ 500 mas) ALMA data (Kamenetzky et al., 2013) revealed the presence of bright rotational emission from cold (< 150 K) relatively slow moving (~ 2000 km s^{-1}) carbon monoxide CO and silicon monoxide SiO.

We have now observed SN 1987A with ALMA in the CO $J = 2-1$, SiO $J = 5-4$ and $J = 6-5$ rotational transition lines using the long baseline, high angular resolution mode of the telescope. These observations are of the highest resolution ever made for SN 1987A and enable us to create and compare the first 3D maps of molecular emission from deep inside the remnant with state-of-the-art explosion models.

6.2 Observations and data reduction

ALMA observations of SN 1987A at 1.3 mm (Band 6, $211-275$ GHz) were performed in two different epochs: cycle 2 low angular resolution images were made in September 2, 2014 (A001/X10e/X140), and cycle 3 high angular resolution images were obtained from November 1 to 15, 2015 (A001/X1ee/X620). Combining data from both cycles improves the image quality. Both data sets were calibrated against QSOs (Quasi-stellar objects).

For the cycle 2 data set J0519–4546 (05:19:49.72, -45:46:43.85; 0.75 Jy at 234 GHz) was the absolute flux calibrator and J0635–7516 (06:35:46.51, -75:16:16.82; 0.68 Jy at 234 GHz) was the phase calibrator. The cycle 3 high-resolution data consisted of two separate observations for each spectral setup. The $^{12}C^{16}O$ $2-1$ (230.538 GHz) and $^{28}Si^{16}O$ $5-4$ (217.105 GHz) images include data using J0519–4546 (0.75 Jy at 224 GHz) as the absolute flux calibrator and J0601–7036 (06:01:11.25, -70:36:08.79; 0.70 Jy at 224 GHz) as the phase calibrator. The SiO $6-5$ (260.518 GHz) image includes data using either J0519–4546 (0.63 Jy at 253 GHz) or J0334–4008 (03:34:13.65, -40:08:25.10; 0.44 Jy at 253 GHz) as the absolute flux calibrator and J0601–7036 (0.58 Jy at 253 GHz) as the phase calibrator.

Combining the cycle 2 and 3 data sets results in baselines between 34 m (25 kλ) and 16,196 m (12,600 kλ). We used the Common Astronomy Software Application (casa.nrao.edu) to process the interferometric data into a cube with 50 mas angular resolution and 100 km s^{-1} spectral bins (for spherical expanding ejecta at the time of these observations, 100 km s^{-1} corresponds to a path length of $\sim 9 \times 10^{15}$ cm or 12 mas). For imaging and deconvolution we used the task `tclean` with different `multiscale` scales depending on the resulting beam sizes. For CO $2-1$ and SiO $5-4$ images, we adopted $scales = [0, 7, 21]$, and for the SiO $6-5$ image we adopted $scales = [0, 5, 15]$. In both cases, we used a 6 mas pixel size.

To determine the 3D distribution, we converted velocity into angular size on the sky by assuming the distance to the LMC to be 50 kpc. We adopted a spherical free expansion, and for the age of the supernova we took the time elapsed since the supernova explosion and the date of the observations (~ 28.7 years).

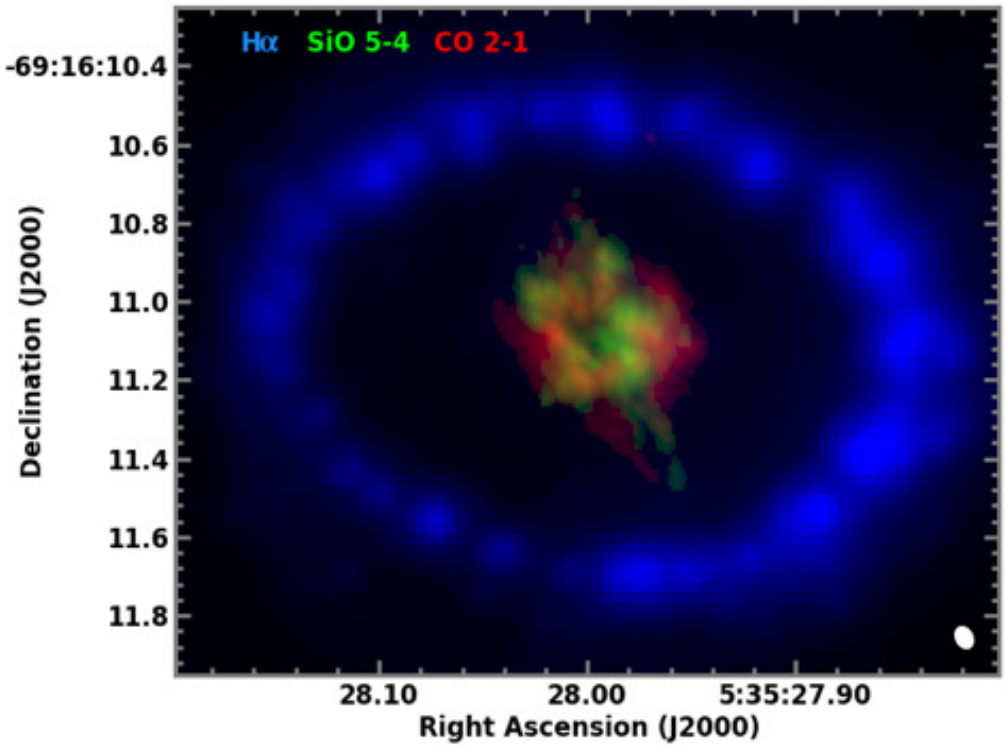

Figure 6.1: Molecular emission and Hα emission from SN 1987A. The more compact emission in the center of the image corresponds to the peak intensity maps of CO $2-1$ (red) and SiO $5-4$ (green) observed with ALMA. The surrounding Hα emission (blue) observed with HST shows the location of the circumstellar equatorial ring (Larsson et al., 2016).

The assumption of free expansion can be tested in the spatially summed image. Using the full width at zero intensity (FWZI) ~ 4000 km s^{-1}, and a corresponding angular size of the velocity-integrated image of ~ 480 mas, we obtain a time of 28.5 years since the explosion. There is no evidence of deceleration of the supernova ejecta, and therefore the free expansion approximation is valid.

6.3 Observational results

In Figure 6.1 we present the CO $2-1$ and SiO $5-4$ emission framed by the circumstellar equatorial ring. Phenomenologically the image provides strong clues to the structure of the inner ejecta of the supernova. The CO and SiO distributions are spatially distinct: both have a toroidal or shell-like distribution around the center, but most of the CO emission presents a maximum extension larger

than SiO emission ($\pm$1700 km s^{-1} vs. $\pm$1300 km s^{-1}; or $\pm 1.53 \times 10^{17}$ cm vs. $\pm 1.17 \times 10^{17}$ cm, approximately).

The 3D distribution of CO $2-1$ and SiO $5-4$ is shown in Figures 6.2 and 6.3. Detailed examination reveals that the CO emission forms a torus-like shape perpendicular to the equatorial ring, clear evidence of asymmetry in the explosion. By contrast, SiO is clumpier and distributed in a broken shell rather than a torus. Within a region $\leq$ 1500 km s^{-1} (1.35×10^{17} cm) from the center of the explosion, we find that 25% of the clumps have peaks brighter than 1.9$\times$ and 1.6$\times$ the mean CO and SiO intensity, respectively. Translating the peak brightness of clumps into peak density of clumps requires modeling the non-LTE excitation of each clump, which we cannot do with only one emission line. However, if we use the average kinetic temperature and collider density derived for the entire nebula (Matsuura et al., 2017), then a peak brightness 3$\times$ brighter than average would translate into an SiO density 5$\times$ higher than average, for the typical clump size.

The brightest SiO emission is from a single blob located off-center below the equatorial plane (i.e., the side located closer to Earth). In both species, the emission joins into a more continuous torus or shell at about 50% of the peak of emission, and the central deficit of emission becomes fully enclosed at about 30% of the peak of emission (see Figure 6.3).

Figure 6.2: 3D view of cold molecular emission in SN 1987A. The CO $2-1$ (red) and SiO $5-4$ (green) emission is shown from selected view angles. The central region is devoid of significant line emission. The emission contours are at the 60% level of the peak of emission for both molecules. The black dotted line and black filled sphere indicate the line of sight and the position of the observer, respectively. The gray ring shows the location of the reverse shock at the inner edge of the equatorial ring (XZ plane). The black cross marks the geometric center. An animation of this figure is available in the online journal.

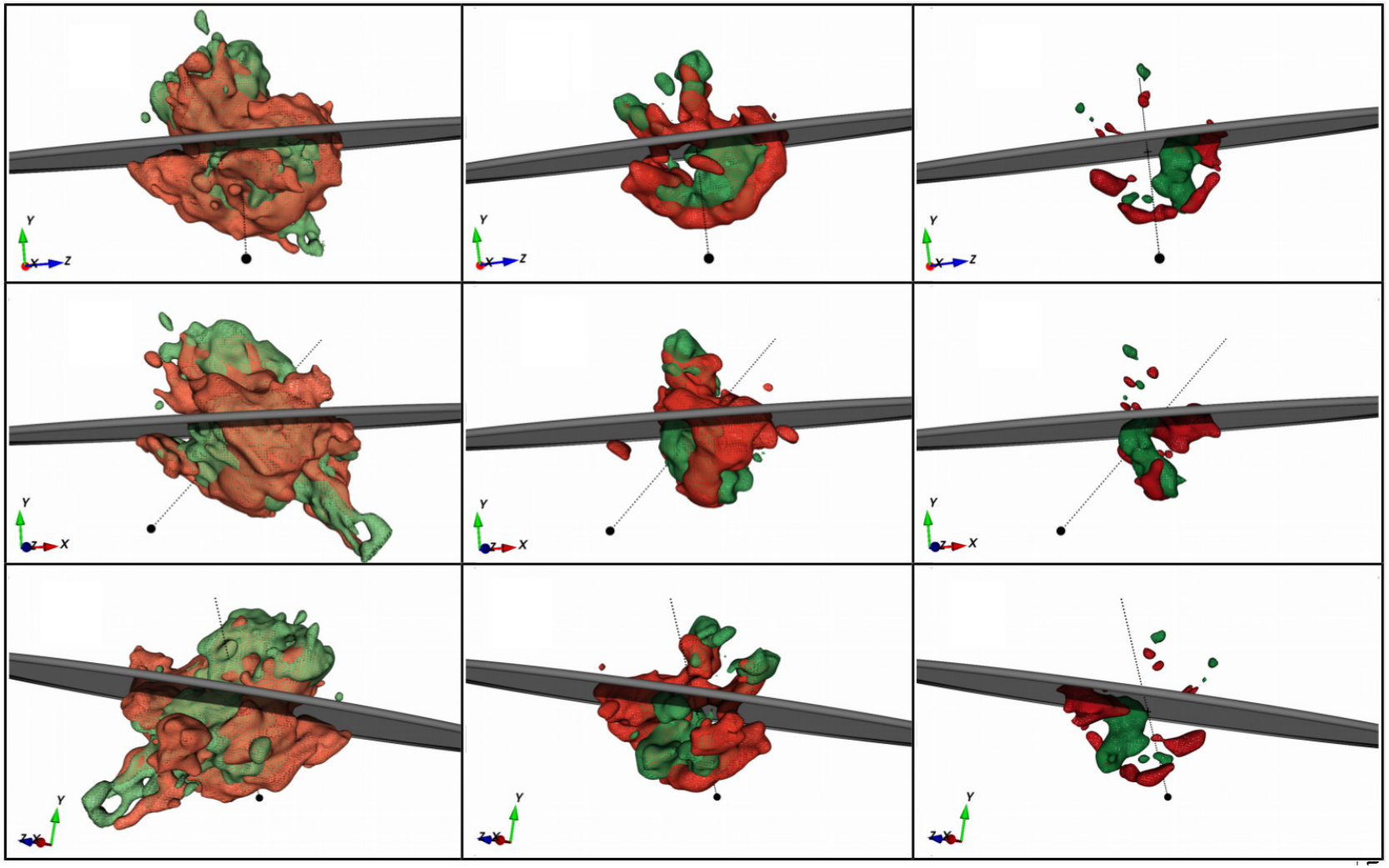

Figure 6.3: 3D distribution of emission of CO $2-1$ (red) and SiO $5-4$ (green) for selected view angles. From left to right the plots show the emission at 30%, 50%, and 70% of the peak of emission of each line.

The observed low emission at the central region agrees with predictions from numerical models according to which different mechanisms (e.g., ^{56}Ni-bubble effect, second outward shock, Ertl et al., 2016) would accelerate the innermost material outwards. The zones with the lowest emission ($< 20\%$ of peak of emission) have similar sizes as the brightest clumps ($> 70\%$ of peak of emission) and a similar filling fraction of $\sim 25\%$. The parts of the ejecta with the least SiO emission are preferentially found around the center ($r \leq 0''1$ or $r \leq 7.5 \times 10^{16}$ cm), whereas holes of emission in CO span a range of radii similar to the range spanned by the brightest CO clumps. We have examined the distribution of these zones of minimal emission and find that both CO and SiO holes are roughly perpendicular to the CO torus. One possibility could be that these regions are filled with material of different composition, like the heavy-element-dominated ^{56}Ni fingers predicted by some models.

The structure of the molecular emission is not aligned with the emission of 1.644 μm [Si I]+[Fe II], which is concentrated in two asymmetric lobes fairly close to the plane of the ring and is brightest at larger radii than both CO and SiO (Larsson et al., 2016). Differences could be due to chemistry, molecular dissociation by positrons, different excitation mechanisms (thermal versus non-thermal), or dust obscuration. Figures 6.2 and 6.3 also reveal the first direct evidence of non-spherical instabilities, as SiO extends to greater radial distances (velocities) than CO in some directions. Considering emission brighter than 30% of the peak of emission, SiO has a greater extent than CO in 25% of radial directions, and in a few directions, extends up to 500 km s^{-1} greater radial velocities.

6.4 Comparison with hydrodynamical models

We compare our data to 3D numerical models of neutrino-driven core-collapse supernovae obtained with the finite-volume Eulerian multifluid hydrodynamics code PROMETHEUS (Utrobin et al., 2015; Wongwathanarat et al., 2015) that employs an approximate, gray neutrino transport. All models considered are single-star models. To follow the simulations from $11-15$ milliseconds after core-bounce to about 150 days we also include a description of the ^{56}Ni heating. The additional heating increases the outward velocities of the innermost ^{12}C and ^{28}Si by about 20%, so while it is not likely the only cause of the observed central evacuation, this "nickel heating" effect does contribute.

The progenitor mass for SN 1987A is in the range of $14-20\,M_\odot$ (Arnett et al., 1989; McCray, 1993; Smartt, 2009). We study four different non-rotating, non-magnetic progenitors: two 15 $M_\odot$ red supergiants (RSGs), model W15 (Woosley & Weaver, 1995) and model L15 (Limongi et al., 2000), and two blue supergiants (BSGs) tailored to represent SN 1987A progenitors: a 20 $M_\odot$ model N20

(Shigeyama & Nomoto, 1990) and a 15 $M_\odot$ model B15 (Woosley et al., 1988). The BSG models have a shallower density profile at the H/He interface than the RSG models, and differ significantly in the C+O core mass (N20 $\sim$ 3.8 $M_\odot$ vs. B15 $\sim$ 1.7 $M_\odot$).

One-dimensional models of molecule formation in supernovae have been published (Lepp et al., 1990; Liu & Dalgarno, 1996; Sarangi & Cherchneff, 2013; Sluder et al., 2016) but there are no models that combine higher-dimensional hydrodynamic evolution of the ejecta with chemical processes. The emitted line radiation also depends on molecular excitation. This deep in the ejecta, it is reasonable to assume that excitation and heating are predominantly due to ^{44}Ti decay. CO and SiO emission may therefore reflect the ^{44}Ti abundance distribution in addition to the CO and SiO abundance distributions. We have not yet detected variations in the CO or SiO excitation temperature which would result from inhomogeneous excitation, but such variations may be detectable with future analysis of ALMA data.

Nevertheless, in order to focus on the size scales and spatial distributions, we compare the CO and SiO emission distributions directly to the square root of the product of the ^{12}C and ^{16}O, and of ^{28}Si and ^{16}O modeled atomic density distributions. We also analyzed ^{12}C and ^{28}Si individually, with and without density ceilings at which CO and SiO become optically thick. If the yields are high (a large fraction of the available atoms remains in gas-phase molecules), then the molecular densities will be high enough to make the observed CO and SiO lines optically thick.

We tested this in our structure comparisons by introducing an upper cutoff to the model volume density. For a rotational transition from level J at energy E_u to level $J-1$ at energy E_l, the Sobolev large velocity gradient optical depth is related to the molecular density n, rotational partition function Q and excitation temperature T_x. For a diatomic rotator, like CO or SiO, the energy levels are $E_J = BJ(J+1)$ where B is the rotational constant and $g_J = 2J+1$ is the statistical weight. As long as T_x is not too low compared to B, the partition function can be approximated by $Q \sim T/B$, with $B/k_B = 2.766$ K. Since the kinetic temperature is $T \sim 50$ K (Matsuura et al., 2017), the approximation is very reasonable. Assuming the same T_x for all levels,

$$\tau \approx \frac{\lambda^3 A_{ul} g_u t}{8\pi Q} \left(e^{-E_l/T_x} - e^{-E_u/T_x} \right) n \tag{6.1}$$

For the CO $2-1$ transition, the Einstein coefficient $A_{21} = 6.9 \times 10^{-7}$ s^{-1}. At $T \sim 50$ K, and at the time of the observation, $\tau_{\rm CO} \approx 2.7 \times 10^{-3}\ n_{\rm CO}$. Optical depth unity therefore corresponds to a CO density of $n_{\rm CO} \sim 374$ cm^{-3}. This is within a factor of order unity of the maximum model densities, so does not affect

our conclusions about relative structure size distributions. The same calculation for the SiO $5-4$ transition, with $A_{54} = 5.2 \times 10^{-4}$ s^{-1}, yields $\tau_{\rm SiO} \approx 4.2\ n_{\rm SiO}$. Thus, optical depth unity corresponds to a SiO density of $n_{\rm SiO} \sim 0.24$ cm^{-3}, a rather more severe threshold compared to model densities. From lower angular resolution ALMA observations, the total CO and SiO masses are a few $\times 10^{-2}$ $M_\odot$ and a few $\times 10^{-4}$ $M_\odot$, respectively, with uncertainties of a factor of several (Matsuura et al., 2017). These masses account for $< 20\%$ and $< 0.1\%$ of the expected C and Si yields (Woosley & Weaver, 1995). Models suggest that formation of silicate dust is very efficient in this environment, leaving only a small fraction of ^{28}Si currently in molecular SiO (Sarangi & Cherchneff, 2013). Thus, until more complete 3D models including dust formation exist, we compare the modeled ^{28}Si$\times^{16}$O distribution without a cutoff with observed SiO.

The results obtained for the clump sizes and distributions are robust to the different approaches. The main difference is that ^{28}Si$\times^{16}$O has a more pronounced central hole than ^{28}Si alone, more similar to the SiO data. Due to the fact that ^{16}O extends further out than ^{28}Si, their intersection has more of a hole. Instead, the differences between ^{12}C$\times^{16}$O and ^{12}C alone are less significant, as expected since these nucleosynthetic products start out at more similar radii before the instabilities take place. Figure 6.4 shows the phenomenological comparison of the data and the four models homologously scaled from 150 days to 29 years, and convolved to the observational resolution.

Figure 6.4: Top row: a single slice $\sim 4.5 \times 10^{15}$ cm thick through the center of the 3D distributions of observed CO $2-1$ and modeled $^{12}C\times^{16}O$ for W15, L15, N20 and B15 at 75% of peak CO emission or of peak $^{12}C\times^{16}O$ density. Bottom row: same as top row, but for observed SiO $5-4$ and the same models for $^{28}Si\times^{16}O$ at 65% of peak SiO emission or of peak $^{28}Si\times^{16}O$ density. The dynamics of the explosion of these models was not tailored to match the properties of SN 1987A. Thus, while clumpiness, radial extent, and length scales can be compared, an exact morphological match would be merely coincidental. The clump sizes and distribution of the models are visually similar from different viewing angles and do not depend on the particular orientation of the slice. In these plots, the CO and SiO data cubes have been rotated 43° so that the equatorial ring is horizontal.

Different quantitative metrics are sensitive to different aspects of a 3D hierarchical structure. Segmenting the cube into clumps using *cprops* (Rosolowsky & Leroy, 2006) and *clumpfind* (Williams et al., 1994) algorithms reveals the clump size distribution. On the other hand, the radially averaged 3D Fourier transform, and the distribution of distances between pairs of points above a given intensity threshold (thresholds between 50% and 90% of peak of emission were considered), reveal the range of clump separations and any large-scale structure such as the toroidal arrangement of CO. Figures 6.5 and 6.6 show the clump size and clump separation for data and models of CO and SiO, respectively. In order to help illustrate the metric, simple geometries are also shown in Figure 6.7.

The results that are most robust to different thresholds and segmentation parameters are the following: none of the models fit both emission lines in all structural metrics, but for CO, the RSG models W15 and L15 have $^{12}C\times^{16}O$ clump sizes comparable to the data. Instead, for SiO, the RSG models have a large range of $^{28}Si\times^{16}O$ clump sizes, on average, $\sim 35\%$ larger than the typical SiO clump sizes. For both lines, the clump sizes of BSG models N20 and B15 tend to be too small compared to the observations.

The clump separation of CO shows a clear peak at $\sim 0''.25$ consistent with a toroidal structure of that diameter, while the distribution of SiO shows a minor peak at $\sim 0''.30$. For both CO and SiO, the RSG models do not have such a clear peak, but instead they have a broader range of intermediate scales, reflecting the intermediate-sized structures visible in Figure 6.4. For SiO, both W15 and L15 models have a large-scale shell or torus comparable in extent to the data. The BSG models are more fragmented into small structures than the observations. Model N20 has small clumps with a wide range of clump-to-clump distances, and a larger shell structure than the data. For CO, the BSG model B15 does not have a range of intermediate distances but shows a strong peak at $\sim 0''.22$, more similar to the CO data.

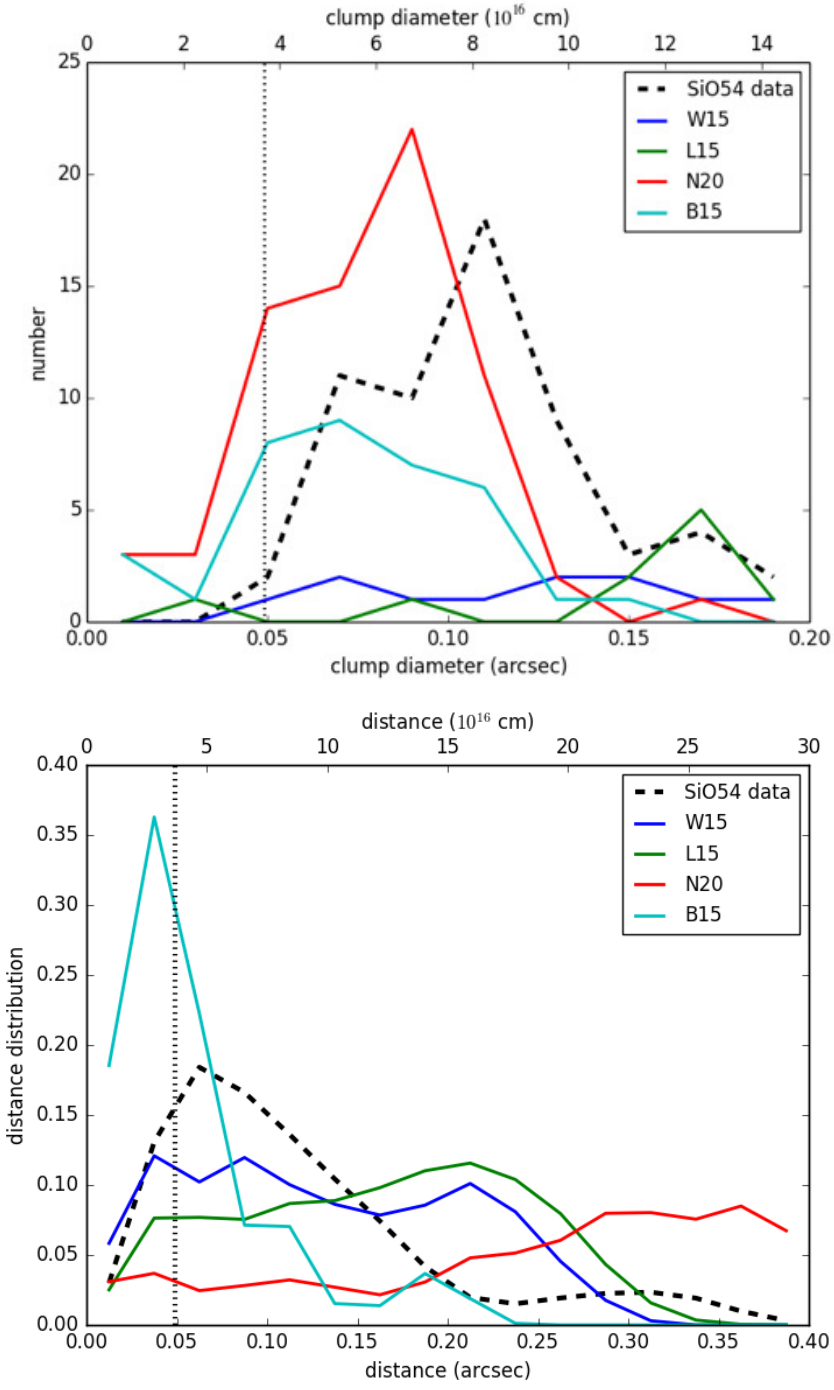

Figure 6.6: Top: distribution of clump sizes, in SiO emission and in the product of ^{28}Si$\times^{16}$O modeled density. Bottom: clump separation between points with bright emission, or high modeled atomic density. All points in the 3D cubes above 65% of peak SiO emission, or of peak ^{28}Si$\times^{16}$O density for the models, are included in the calculation. The SiO data show a minor peak at $\sim 0''.30$ consistent with a broken shell structure of that diameter. The vertical dotted line represents the beam size.

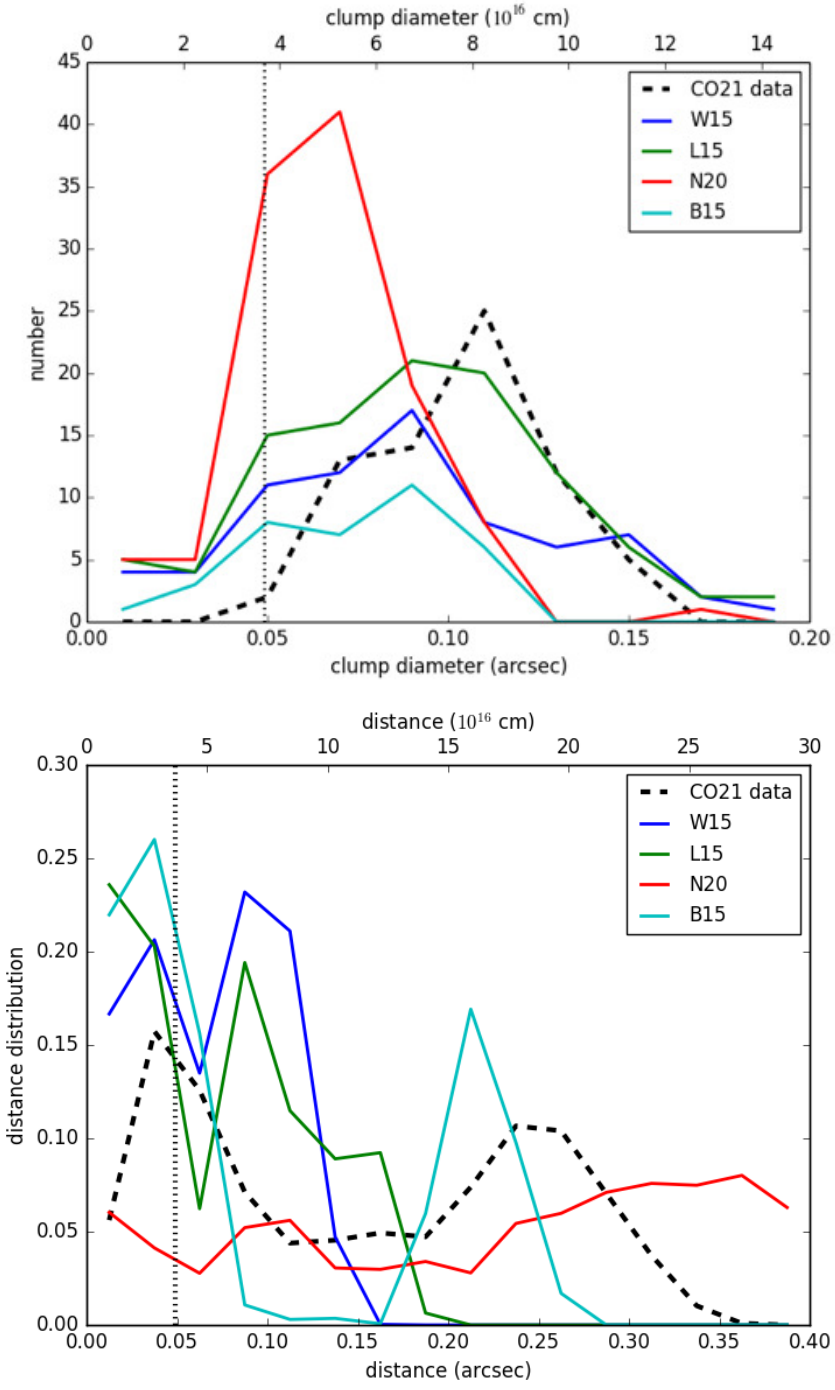

Figure 6.5: Top: distribution of clump sizes, in CO emission and in the product of $^{12}C \times ^{16}O$ modeled density. Bottom: clump separation between points with bright emission, or high modeled atomic density. All points in the 3D cubes above 75% of peak CO emission, or of peak $^{12}C \times ^{16}O$ density for the models, are included in the calculation. The CO data show a clear peak at $\sim 0''.25$ consistent with a toroidal structure of that diameter. The vertical dotted line represents the beam size.

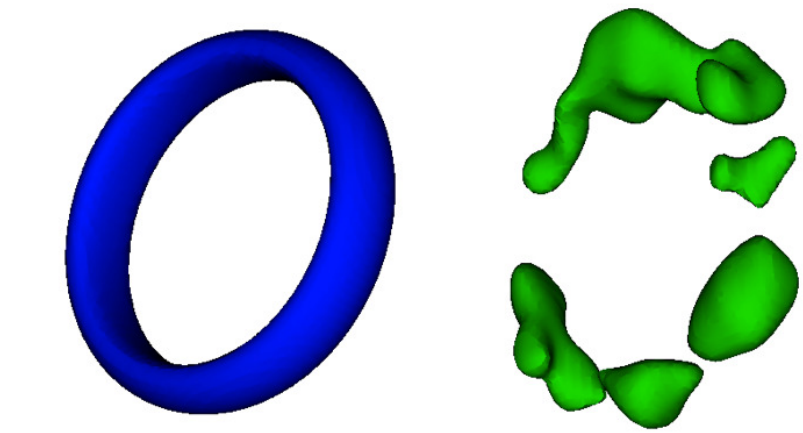

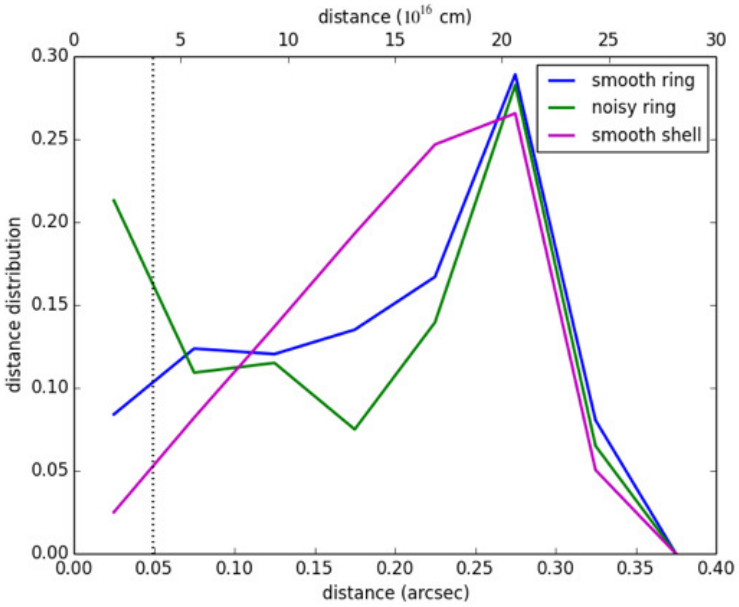

Figure 6.7: Top: two simple shapes, (a) a ring or torus, and (b) clumps arranged in a ring-like distribution similar to observed in CO. Bottom: clump separation of (a) shows a strong peak at the diameter of the ring, while the clump separation of (b) maintains that peak but in addition shows a peak at small scales tracing typical clump sizes and separations. A closed shell (not shown) shows a peak at the diameter of the shell, but a broader range of intermediate distances. The vertical dotted line represents the beam size.

6.5 Conclusions

We have used the extraordinary capabilities of ALMA to create unique 3D maps of CO and SiO molecular emission from the inner ejecta of SN 1987A with unprecedented spatial resolution. Our observations show the clumpy mixed structure predicted by models (e.g., Hammer et al., 2010) but not previously well-imaged, as well as a clear sign of asymmetry in the supernova explosion. We find that the molecular emission forms a torus-/shell-like shape perpendicular to the equatorial ring, and in some directions, the SiO extends further out than CO from the center of the remnant, a proof that non-spherical instabilities have taken place at the time of the explosion.

From the comparison of these data to hydrodynamical models we conclude that none of the models correctly reproduce neither the radial extent of both lines nor the range of clump sizes. The first discrepancy might be solved by adjusting the explosion energy of the model, but the second is directly related to the progenitor structure and the strongest asymmetries produced during shock revival, or to as of yet unmodeled chemical or excitation effects. However, considering that the models are not particularly tuned to reproduce SN 1987A, the agreement in some features as the overall shape of CO and SiO emission is surprisingly good.

The models compared here are non-rotating, and thus we cannot say how different the signatures of SASI would be. Comparing these data with a larger range of models, also including SASI mechanisms, will constrain explosion physics more precisely than has been possible heretofore using unresolved images and spectra, as different model parameters affect the size scales of clumpy structure in different ways: the explosion energy changes the overall extent, instability physics and the duration of the unstable phase affects the small-scale clump sizes. Progenitor structure and astrochemistry (fractional molecular yield compared to elemental abundance) also change the range of clump sizes and extent of their envelopes.

Chapter 7

Conclusions and future work

No llores porque ya se terminó...
sonríe porque sucedió.

Gabriel García Márquez

In this thesis, we have presented the results of our research in two distinct subjects: a high-precision astrometric analysis of the S5 polar cap sample and a study of the 3D distribution of the molecular emission in the SN 1987A ejecta. Both projects have in common that the observations were made at radio wavelengths by means of radio interferometric techniques. However, the distinct nature of each project made their analysis (e.g., data editing, calibration and imaging) very different. Whilst the global high-precision astrometry made use of VLBA observations (i.e., VLBI), the study of the SN 1987A ejecta made use of ALMA observations (i.e., connected interferometry). Thus, we had to use different approaches and software in each case.

In this chapter, we present the main results obtained and highlights future work which could complement and build on the findings presented in this thesis.

7.1 Summary of the results

7.1.1 High-precision astrometry

- **We have performed a high-precision wide-angle astrometric analysis of the complete S5 polar cap radio sample, and for the first time in VLBI, we have globally connected the phase-delays at a frequency as high as 43.1 GHz.** Since the delay corresponding to one 2π phase cycle at this frequency is so short (~ 23 ps), compared to the residual delay rates, integrated over the duty cycles of our observations, from our experience we conclude that the Q band might mark the observational limit for this astrometric technique. Thus, it is likely that a similar work cannot be performed at higher frequencies (e.g., 86 GHz) with the current instrumentation.

- **Our successful global astrometric analysis at Q band has enabled us to study the changes in the source core positions between different epochs and/or between different frequencies**. From the inter-epoch analysis, we have found that the differences in source separations among all the source pairs observed in common in the two epochs are compatible at 1σ level between both bands.

- **We find motions of $0.1-0.9$ mas among close-by sources between the two epochs, which imply drifts in the jet cores of approximately a few tens of μas yr^{-1}.** These results have implications for the standard AGN jet model (where the core locations are supposed to be stable in time).

- **We have performed a SFPR calibration, from 14.4 GHz to 43.1 GHz, to determine the core-shifts of the sources.** With this technique, we have found typical core-shifts of $0.05-0.2$ mas. Besides, from the inter-frequency analysis of year 2010, we find that the differences in source separations between U and Q bands are compatible at the 1σ level with those estimated with the SFPR technique.

- **We have developed an inter-frequency differential phase-delay analysis (IFDPD) to study the core-shift effect between the U and Q bands in a way independent of the SFPR technique.** With this new method, we have found degeneracy in some of the core-shift directions, perhaps due to strong coupling between the parameters associated to the atmosphere (mainly residual ionosphere) and the CCOs at Q band in the Monte Carlo analysis.

- **We have fitted the core emission of the sources at U and Q bands to Gaussian intensity distributions.** We have found that the position angles of the major Gaussian axes are similar between the two bands for most of the sources. This result indicates that a considerable fraction of the total sample shows rather straight jets. Besides, we have compared the core-shift directions to the core orientations at both bands and we have found that there is good agreement between the core orientations at U band and the core-shifts, for the sources with most accurate core-shift estimates. On the other hand, from the analysis of the axis ratio of the core Gaussians at each frequency, we conclude that at least a fraction of the Q band emission is likely to come from the concave jet region, where the jet width is not proportional to the distance from the jet base.

- **We have presented three different methods to study the core-shift effect and we conclude that, even though they do not agree in the estimate of the core-shift directions in some cases, they are all compatible in the absolute values of the core-shifts.** In some cases, the discrepant orientations are due to insufficient information for the corresponding method to be successfully applied. In other cases, the discrepancies reflect assumptions of the methods and could be explained by curvatures in the jets and/or departures from conical jets. Interestingly, the absolute values of the core-shifts determined with all methods presented in this thesis are of the same order as those predicted by the statistical study of Kovalev et al. (2008) using a simplified SSA jet model (e.g., Lobanov, 1998b), if extrapolated to the whole S5 polar cap sample at U and Q bands.

- **We have constructed robust spectral-index images of the sources.** The spectral-index distributions follow the well-known steepening of the spectrum at the jet extensions, from an either flat- or inverted-spectrum region associated to jet cores. There is one source, $0615+820$, that shows a remarkable double structure at 43.1 GHz. In this source, we have found that the true jet core does not correspond to the absolute brightness peak. Possible explanations for this could be either a strong jet bending at parsec scales from the AGN central engine (due to interaction with the ISM), a gravitational lens with mas scale, or a binary massive black hole.

7.1.2 Tomography of the SN 1987A ejecta

- **We have created unique 3D maps of CO and SiO emission from the inner ejecta of SN 1987A with unprecedented spatial resolution.** Our observations show the clumpy mixed structure predicted by models (e.g., Hammer et al., 2010) but not previously imaged, as well as a clear sign of asymmetry in the supernova explosion.

- **We have found that the CO/SiO emission forms a torus-/shell-like shape perpendicular to the equatorial ring, and in some directions, the SiO extends further out than CO from the center of the remnant**. This is an observational proof that non-spherical instabilities took place at the time of the explosion.

- **From the comparison of these results with state-of-the-art hydrodynamical models of supernova explosions, we conclude that none of the models correctly reproduce neither the radial extent of the emissions in of CO and SiO nor the range of clump sizes.** The first discrepancy might be solved by adjusting the explosion energy of the model, but the second is directly related to the progenitor structure and the strongest asymmetries produced during shock revival, or to as of yet unmodeled chemical or excitation effects. However, considering that the models are not particularly tuned to reproduce SN 1987A, the agreement in some features as the overall shape of CO and SiO emission is surprisingly good.

- **The models used for the comparison are non-rotating, and thus we cannot say how different the signatures of standing accretion shock instability (SASI) would be.** Comparing these results with a larger range of models, also including SASI mechanisms, would constrain explosion physics more precisely than has been possible heretofore using unresolved images and spectra, as different model parameters affect the size scales of clumpy structure in different ways: the explosion energy changes the overall extent, instability physics and the duration of the unstable phase affects the small-scale clump sizes. Progenitor structure and astrochemistry (fractional molecular yield compared to elemental abundance) also change the range of clump sizes and extent of their envelopes.

7.2 Future work

The global high-precision differential astrometry over large sky angles with VLBI belongs to a large astrometry campaign aimed to study the S5 polar cap sample. This campaign started about 20 years ago. The goals pursued over this period have been finally reached, and hence, the work presented in this thesis represents somehow the completion of the project. This means that no further research on this topic is planned in the near future. However, given the inconclusive results obtained for source $0615+820$, we are continuing the observation and study of this source, out of the scope of the original S5 astrometry project. Observations with the Global mm-VLBI Array (GMVA) have been already made. These observations will help determine the nature of this intriguing source.

With respect to the study of SN 1987A, there is way too much to do in the following years. We will continue studying the emission of the core of the inner ejecta both in higher transition lines than heretofore and in the same lines to see the time evolution. The international ALMA collaboration, in which I am involved, has submitted a follow-up proposal to observe the evolution of the ejecta as the X-rays from the reverse shock propagate into the inner ejecta. Over the 1000 day interval since our previous observations, ALMA can resolve the expansion of the ejecta at > 2000 km s^{-1}. Over this time interval the X-ray penetration of the ejecta will have increased significantly, and the radioactive ^{44}Ti heating decreased. Additionally, we shall also observe the ongoing destruction of the ring and seek evidence for a compact remnant. This proposal (Id: 2017.1.00789.S), led by Dr. Remy Indebetouw, has been A-ranked.[1] Thus, at the time of writing, we expect to get high resolution observations that enable us to study the time variation of the supernova remnant by comparing to the results presented in this thesis.

Furthermore, an analysis of the SiO line ratios with the cycle 3 ALMA data used in this thesis needs still to be done. The examination of the line ratios will tell us much about differential excitation of the nebula, which will be very interesting for a correct physical interpretation.

As part of the ALMA team, I am also involved in another proposal. This proposal (Id: 2017.1.00221.S), led by Dr. Mikako Matsuura and A-ranked, is aimed to study the macroscopic/microscopic mixing in the supernova ejecta by resolving the HCO+ emission. Another proposal led by Dr. Giovanna Zanardo, member of the ALMA collaboration, has been also A-ranked. This proposal is aimed to investigate the polarized emission in the supernova remnant.

[1] Grade A: Highest priority proposals that will be rolled over to the subsequent observing cycle if necessary to complete. Such proposals must be suitable for roll over considering the nature of the project and the availability of configurations.

SN 1987A is one of the rare objects in which real-time astronomy can be studied. Thus, the research on SN 1987A with ALMA will surely continue during the next years.

Bibliography

Ables, J. G. *Maximum Entropy Spectral Analysis*. 1974, A&AS, 15, 383

Alef, W., & Porcas, R. W. *VLBI fringe-fitting with antenna-based residual*. 1986, A&A, 168, 365

Antonucci, R. *Unified models for active galactic nuclei and quasars*. 1993, ARA&A, 31, 473

Arnett, W. D., Bahcall, J. N., Kirshner, R. P., & Woosley, S. E. *Supernova 1987A*. 1989, ARA&A, 27, 629

Asada, K., & Nakamura, M. *The Structure of the M87 Jet: A Transition from Parabolic to Conical Streamlines*. 2012, ApJ, 745, L28

Baade, W., & Minkowski, R. *Identification of the Radio Sources in Cassiopeia, Cygnus A, and Puppis A*. 1954, ApJ, 119, 206

Bartel, N., Herring, T. A., Ratner, M. I., Shapiro, I. I., & Corey, B. E. *VLBI limits on the proper motion of the 'core' of the superluminal quasar 3C345*. 1986, Nature, 319, 733

Bartel, N. 2003, *VLBI Astrometry*, Astronomy in Latin America, Second Meeting on Astrometry in Latin America and Third Brazilian Meeting on Fundamental Astronomy, v.1, p.35-42

Bartel, N. 2012, *VLBI astrometry. Probing astrophysics, celestial reference frames, and General Relativity*, Memorie della Societa Astronomica Italiana, v.83, p.911

Basko, M. *Nickel bubble instability and mixing in SN 1987A*. 1994, ApJ, 425, 264

Beasley, A. J., & Conway, J. E. *VLBI Phase-Referencing*. 1995, in ASP Conf. Ser. 82, Very Long Baseline Interferometry and the VLBA, ed. J. A. Zensus, P. J. Diamond, & P. J. Napier (San Francisco, CA: ASP), 327

Begelman, M. C., Blandford, R. D., & Rees, M. J. *Theory of extragalactic radio sources*. 1984, Rev. Modern Phys., 56, 255

Benz, W., & Thielemann, F.-K. *Convective instabilities in SN 1987A*. 1990, ApJ, 348, L17

Bethe, H., & Wilson, J.R. *Revival of a stalled supernova shock by neutrino heating*. 1985, ApJ, 295, 14

Bietenholz, M. F., Bartel, N., & Rupen, M. P. *The Location of the Core in M81*. 2004, ApJ, 615, 173

Blandford, R. D. & Königl, A. *Relativistic jets as compact radio sources*. 1979, ApJ, 232, 34

Blondin, J. M., Mezzacappa, A., & DeMarino, C. *Stability of Standing Accretion Shocks, with an Eye toward Core-Collapse Supernovae*. 2003, ApJ, 584, 971

Boggs, S. E., Harrison, F. A., Miyasaka, H., et al. *^{44}Ti gamma-ray emission lines from SN 1987A reveal an asymmetric explosion*. 2015, Science, 348, 670

Bouchet, P., Phillips, M. M., Suntzeff, N. B., et al. *The Bolometric Lightcurve of Supernova 1987A - Part Two - Results from Visible and Infrared Spectrophotometry*. 1991, A&A, 245, 490

Broderick, A. E., Loeb, A., & Reid, M. J. *Localizing Sagittarius A* and M87 on Microarcsecond Scales with Millimeter Very Long Baseline Interferometry*. 2011, ApJ, 735, 57

Burke, B. F. & Graham-Smith, F. *An Introduction to Radio Astronomy*. 2009, 3 ed., Cambridge University Press, UK

Burrows, A., Hayes, J., & Fryxell, B. A. *On the Nature of Core-Collapse Supernova Explosions*. 1995, ApJ, 450, 830

Burrows, D. N., Michael, E., Hwang, U., et al. *The X-Ray Remnant of SN 1987A*. 2000, ApJL, 543, L149

Burrows, A. *Colloquium: Perspectives on core-collapse supernova theory*. 2013, Rev. Mod. Phys., 85, 245

Charlot, P. *Radio-source structure in astrometric and geodetic very long baseline interferometry*. 1990, AJ, 99, 1309

Charlot, P., Boboltz, D. A., Fey, A. L., et al. *The Celestial Reference Frame at 24 and 43 GHz. II. Imaging*. 2010, AJ, 139, 1713

Chevalier, R. A. *Self-similar solutions for the interaction of stellar ejecta with an external medium*. 1982, ApJ, 258, 790

Cotton, W. D. *Fringe Fitting*. 1995, in Zensus, J. A., Diamond, P. J., & Napier, P. J. eds, Astronomical Society of the Pacific Conference Series Vol. 82, Very Long Baseline Interferometry and the VLBA. p. 189

Croke, S. M., & Gabuzda, D. C. *Aligning VLBI images of active galactic nuclei at different frequencies*. 2008, MNRAS, 386, 619

Crotts, A. P. S., & Heathcote, S. R. *SN 1987A's Circumstellar Envelope. II. Kinematics of the Three Rings and the Diffuse Nebula*. 2000, ApJ, 528, 426

Deller, A. T., Tingay, S. J., Bailes, M., & West, C. *DiFX: A Software Correlator for Very Long Baseline Interferometry Using Multiprocessor Computing Environments*. 2007, PASP, 119, 318

Dodson, R., Fomalont, E. B., Wiik, K., et al. *The VSOP 5 GHz Active Galactic Nucleus Survey. V. Imaging Results for the Remaining 140 Sources*. 2008, ApJS, 175, 314

Dodson, R., & Rioja, M. J. *Astrometric calibration of mm-VLBI using "Source/Frequency Phase Referenced" observations*. 2009, VLBA Science Memo 31

Dwek, E., Arendt, R. G., Bouchet, P., et al. *Infrared and X-Ray Evidence for Circumstellar Grain Destruction by the Blast Wave of Supernova 1987A*. 2008, ApJ, 676, 1029

Dwek, E., Arendt, R. G., Bouchet, P., et al. *Five Years of Mid-infrared Evolution of the Remnant of SN 1987A: The Encounter Between the Blast Wave and the Dusty Equatorial Ring*. 2010, ApJ, 722, 425

Ebisuzaki, T., Shigeyama, T., & Nomoto, K. *Rayleigh-Taylor instability and mixing in SN 1987A*. 1989, ApJ, 344, L65

Eckart, A., Witzel, A., Biermann, P., et al. *Investigation of a complete sample of flat spectrum radio sources from the S5 survey*. 1986, A&A, 168, 17

Ertl, T., Ugliano, M., Janka, H.-Th., Marek, A., & Arcones, A. *Erratum: "Progenitor-explosion Connection and Remnant Birth Masses for Neutrino-driven Supernovae of Iron-core Progenitors" (2012, ApJ, 757, 69)*. 2016, ApJ, 821, 69

Fey, A. L., Ma, C., Arias, E. F., et al. *The Second Extension of the International Celestial Reference Frame: ICRF-EXT.1*. 2004, AJ, 127, 3587

Fey, A. L., Gordon, D., Jacobs, C. S., et al. *The Second Realization of the International Celestial Reference Frame by Very Long Baseline Interferometry*. 2015, AJ, 150, 58

Frank, K. A., Zhekov, S. A., Park, S., et al. *Chandra Observes the End of an Era in SN 1987A*. 2016, ApJ, 829, 40

Fransson, C., Cassatella, A., Gilmozzi, R., et al. *Narrow ultraviolet emission lines from SN 1987A - Evidence for CNO processing in the progenitor*. 1989, ApJ, 336, 429

Fransson, C., & Kozma, C. *Radioactivities and nucleosynthesis in SN 1987A*. 2002, NewAR, 46, 487

Fransson, C., Gilmozzi, R., Groeningsson, P., et al. *Twenty Years of Supernova 1987A*. 2007, The Messenger, 127, 44

Fransson, C., Larsson, J., Spyromilio, J., et al. *Late Spectral Evolution of the Ejecta and Reverse Shock in SN 1987A*. 2013, ApJ, 768, 88

Fransson, C., Larsson, J., Migotto, K., et al. *The Destruction of the Circumstellar Ring of SN 1987A*. 2015, ApJ, 806, L19

Fromm, C. M., Ros, E., Perucho, M., et al. *Catching the radio flare in CTA 102. III. Core-shift and spectral analysis*. 2013, A&A, 557, A105

Fromm, C. M., Perucho, M., Ros, E., Savolainen, T., & Zensus, J. A. *On the location of the supermassive black hole in CTA 102*. 2015, A&A, 576, A43

Grebenev, S. A., Lutovinov, A. A., Tsygankov, S. S., & Winkler, C. *Hard-X-ray emission lines from the decay of ^{44}Ti in the remnant of supernova 1987A*. 2012, Nature, 490, 373

Guirado, J. C., Marcaide, J. M., Alberdi, A., et al. *Proper Motion of Components in 4C 39.25*. 1995, AJ, 110, 2586

Guirado, J. C., Marcaide, J. M., Pérez-Torres, M. A., & Ros, E. *VLBI difference astrometry at 43 GHz*. 2000, A&A, 353, L37

Guirado, J. C., Marcaide, J. M., Ros, E., Pérez-Torres, M. A., & Martí-Vidal, I. *Multi-wavelength differential astrometry of the S5 polar cap sample*. 2004, Proceedings of the 7th European VLBI Network Symposium

Haas, M. R., Colgan, S. W. J., Erickson, E. F., et al. *Velocity-resolved far-infrared spectra of forbidden Fe II - Evidence for mixing and clumping in SN 1987A*. 1990, ApJ, 360, 257

Hada, K., Doi, A., Kino, M., et al. *An origin of the radio jet in M87 at the location of the central black hole*. 2011, Nature, 477, 185

Hammer, N. J., Janka, H.-T., & Müller, E. *Three-dimensional Simulations of Mixing Instabilities in Supernova Explosions*. 2010, ApJ, 714, 1371

Hanuschik, R. W. & Thimm, G. J. *Spectroscopic fine-structure in Supernova 1987A*. 1990, A&A, 231, 77

Hashimoto, M., Nomoto, K., & Shigeyama, T. *Explosive nucleosynthesis in supernova 1987A*. 1989, A&A, 210, 5

Hasinger, G., Aschenbach, B., & Truemper, J. *The X-ray lightcurve of SN 1987A*. 1996, A&A, 312, L9

Herant, M., & Benz, W. *Hydrodynamical instabilities and mixing in SN 1987A - Two-dimensional simulations of the first 3 months*. 1991, ApJ, 370, L81

Herant, M., & Benz, W. *Postexplosion hydrodynamics of SN 1987A*. 1992, ApJ, 387, 294

Hirotani, K. *Kinetic Luminosity and Composition of Active Galactic Nuclei Jets*. 2005, ApJ, 619, 73

Högbom, J. A. *Aperture Synthesis with a Non-Regular Distribution of Interferometer Baselines*. 1974, A&AS, 15, 417

Hovatta, T., Lister, M. L., Aller, M. F., et al. *MOJAVE: Monitoring of Jets in Active Galactic Nuclei with VLBA Experiments. VIII. Faraday Rotation in Parsec-scale AGN Jets*. 2012, AJ, 144, 105

Indebetouw, R., Matsuura, M., Dwek, E., et al. *Dust Production and Particle Acceleration in Supernova 1987A Revealed with ALMA*. 2014, ApJ, 782, L2

Janka, H.-T. *Explosion Mechanisms of Core-Collapse Supernovae*. 2012, Ann. Rev. Nucl. Part. Sci., 62, 407

Janka, H.-T., Melson, T., & Summa, A. *Physics of Core-Collapse Supernovae in Three Dimensions: A Sneak Preview*. 2016, Ann. Rev. Nucl. Part. Sci, 66, 341

Janka, H.-T., Gabler, M., & Wongwathanarat, A. *SN 1987A, 30 years later*. 2017, Proceedings IAU Symposium No. 331

Jakobsen, P., Albrecht, R., Barbieri, C., et al. *First results from the Faint Object Camera - SN 1987A*. 1991, ApJ, 369, L63

Jerkstrand, A., Fransson, C., & Kozma, C. *The ^{44}Ti-powered spectrum of SN 1987A*. 2011, A&A, 530, A45

Jimenez-Monferrer, S., Marcaide, J. M., Guirado, J. C., & Martí-Vidal, I. *High-precision astrometry of the S5 polar-cap radio sources: Measurements of the frequency dependence of the VLBI cores*. 2007, Proceedings of Science, p.103

Kamenetzky, J., McCray, R., Indebetouw, R., et al. *Carbon Monoxide in the Cold Debris of Supernova 1987A*. 2013, ApJL, 773, L34

Kettenis, M., van Langevelde, H. J., Reynolds, C., & Cotton, B. *ParselTongue: AIPS Talking Python*. 2006, ASPC, 351, 497

Kjær, K. *Integral Field Spectroscopy Observations of SN 1987A*. 2007, Ph.D. Thesis, LMU München

Kjær, K., Leibundgut, B., Fransson, C., Jerkstrand, A., & Spyromilio, J. *The 3-D structure of SN 1987A's inner ejecta*. 2010, A&A, 517, A51

Königl, A. *Relativistic jets as X-ray and gamma-ray sources*. 1981, ApJ, 243, 700

Kovalev, Y. Y., Lobanov, A. P., Pushkarev, A. B., Zensus, J. A. *Opacity in compact extragalactic radio sources and its effect on astrophysical and astrometric studies*. 2008, A&A, 483, 759

Kovalev, Y. Y., Petrov, L., & Plavin, V. *VLBI-Gaia offsets favor parsec-scale jet direction in active galactic nuclei*. 2017, A&A, 598, L1

Kudryavtseva, N. A., Britzen, S., Witzel, A., et al. *A possible jet precession in the periodic quasar B0605-085*. 2011, A&A, 526, 51

Kühr, H., Witzel, A., Pauliny-Toth, I. I. K., et al. *A catalogue of extragalactic radio sources having flux densities greater than 1 Jy at 5 GHz*. 1981, A&AS, 45, 367

Kutkin, A. M., Sokolovsky, K. V., Lisakov, M. M., et al. *The core shift effect in the blazar 3C 454.3*. 2014, MNRAS, 437, 3396

Lakićević, M., van Loon, J. T., Stanke, T., et al. *Zooming in on Supernova 1987A at submillimetre wavelengths*. 2012, A&A, 541, L1

Lara, L., Alberdi, A., Marcaide, J. M., & Muxlow, T. W. B. *The quasar 3C395 revisited: new VLBI observations and numerical simulations*. 1994, A&A, 285, 393

Larsson, J., Fransson, C., Östlin, G., et al. *X-ray illumination of the ejecta of supernova 1987A*. 2011, Nature, 474, 484

Larsson, J., Fransson, C., Kjær, K., et al. *The Morphology of the Ejecta in Supernova 1987A: A Study over Time and Wavelength*. 2013, ApJ, 768, 89

Larsson, J., Fransson, C., Spyromilio, J., et al. *Three-dimensional Distribution of Ejecta in Supernova 1987A at 10,000 Days*. 2016, ApJ, 833, 147

Lawrence, A. *Classification of active galaxies and the prospect of a unified phenomenology*. 1987, PASP 99, 309

Lawrence, S. S., Sugerman, B. E., Bouchet, P., et al. *On the Emergence and Discovery of Hot Spots in SNR 1987A*. 2000, ApJL, 537, L123

Lepp, S., Dalgarno, A., & McCray, R. *Molecules in the ejecta of SN 1987A*. 1990, ApJ, 358, 262

Limongi, M., Straniero, O., & Chieffi, A. *Massive Stars in the Range 13-25 $M_{\odot}$: Evolution and Nucleosynthesis. II. The Solar Metallicity Models*. 2000, ApJS, 129, 625

Lindegren, L., Lammers, U., Hobbs, D., et al. *The astrometric core solution for the Gaia mission. Overview of models, algorithms, and software implementation*. 2012, A&A, 538, A78

Lindegren, L., Lammers, U., Bastian, U., et al. *Gaia Data Release 1. Astrometry: one billion positions, two million proper motions and parallaxes*. 2016, A&A, 595, A4

Liu, W., Dalgarno, A., & Lepp, S. *Carbon monoxide in SN 1987A*. 1992, ApJ, 396, 679

Liu, W., & Dalgarno, A. *Silicon monoxide in SN 1987A*. 1994, ApJ, 428, 769

Liu, W., & Dalgarno, A. *Formation and Destruction of Silicon Monoxide in SN 1987A*. 1996, ApJ, 471, 480

Lobanov, A. P. *Spectral distributions in compact radio sources. I. Imaging with VLBI data*. 1998a, A&AS, 132, 261

Lobanov, A. P. *Ultracompact jets in active galactic nuclei*. 1998b, A&A, 330, 79

Lobanov, A. P. & Roland, J. *A supermassive binary black hole in the quasar 3C 345*. 2005, A&A, 431, 831

Lobanov, A. P. *Compact jets as probes for sub-parsec scale regions in AGN*. 2007, Ap&SS, 311, 263

Lundqvist, P., & Fransson, C. *Circumstellar emission from SN 1987A*. 1991, ApJ, 380, 575

Manchester, R. N., Gaensler, B. M., Wheaton, V. C., et al. *Evolution of the Radio Remnant of SN 1987A: 1990-2001*. 2002, PASA, 19, 207

Maraschi, L., Ghisellini, G., & Celotti, A. *A jet model for the gamma-ray emitting blazar 3C 279*. 1992, ApJ, 397, L5

Marcaide, J. M. *VLBI Studies of the Extragalactic Radio Sources 1038+528 A.B*. 1982, Ph.D. thesis, MIT

Marcaide, J. M. & Shapiro, I. I. *High precision astrometry via very-long-baseline radio interferometry: Estimate of the angular separation between the quasars 1038+528A and B*. 1983, AJ, 88, 1133

Marcaide, J. M. & Shapiro, I. I. *VLBI study of 1038+528 A and B - Discovery of wavelength dependence of peak brightness location*. 1984, ApJ, 276, 56

Marcaide, J. M., Elosegui, P., & Shapiro, I. I. *On the relative proper motion of quasars 1038+528 A,B*. 1994, AJ, 108, 368

Marscher, A. P. *Relativistic jets and the continuum emission in QSOs*. 1980, ApJ, 235, 386

Marscher, A. P. *Synchro-Compton emission from superluminal sources*. 1987, in Superluminal Radio Sources, eds. J. A. Zensus, & T. J. Pearson, 280

Marscher, A. P., Jorstad, S. G., Gómez, J.-L., et al. *Observational evidence for the accretion-disk origin for a radio jet in an active galaxy*. 2002, Nature, 417, 625

Marscher, A. P. *Multiband Impressions of Active Galactic Nuclei*. 2005, in A. Lobanov and T. Venturi (eds.), Multiband Approach to AGN held in Sept. 2004, Bonn, Germany, vol. 76, p. 168

Marscher, A. P., Jorstad, S. G., D'Arcangelo, F. D., et al. *The inner jet of an active galactic nucleus as revealed by a radio-to-γ-ray outburst*. 2008, Nature, 452, 966

Martí-Vidal, I. *Expansión de SN 1993J y astrometría global de alta precisión*. 2008, Ph.D. Thesis, Univ. of Valencia

Martí-Vidal, I., Marcaide J. M., Guirado J. C., Pérez-Torres, M. A., & Ros, E. *Absolute kinematics of radio source components in the complete S5 polar cap sample III. First wide-field high-precision astrometry at 15.4 GHz*. 2008, A&A, 478, 267

Martí-Vidal, I., Marcaide, J. M., Alberdi, A., et al. *Detection of jet precession in the active nucleus of M 81*. 2011, A&A, 533, 111

Martí-Vidal, I., Muller, S., Combes, F., et al. *Probing the jet base of the blazar PKS 1830–211 from the chromatic variability of its lensed images. Serendipitous ALMA observations of a strong gamma-ray flare*. 2013, A&A, 558, A123

Martí-Vidal, I., Vlemmings, W. H. T., Muller, S., & Casey, S. *UVMULTIFIT: A versatile tool for fitting astronomical radio interferometric data*. 2014, A&A, 563, A136

Martí-Vidal, I., Muller, S., Vlemmings, W., et al. *A strong magnetic field in the jet base of a supermassive black hole*. 2015, Science, 348, 311

Martí-Vidal, I., Abellán, F. J., Marcaide, J. M., et al. *Absolute kinematics of radio-source components in the complete S5 polar cap sample IV. Proper motions of the radio cores over a decade and spectral properties*. 2016, A&A, 596, A27

Mattila, S., Lundqvist, P., Gröningsson, P., et al. *Abundances and Density Structure of the Inner Circumstellar Ring Around SN 1987A*. 2010, ApJ, 717, 1140

Matsuura, M., Dwek, E., Meixner, M., et al. *Herschel Detects a Massive Dust Reservoir in Supernova 1987A*. 2011, Science, 333, 1258

Matsuura, M., Dwek, E., Barlow, M. J., et al. *A Stubbornly Large Mass of Cold Dust in the Ejecta of Supernova 1987A*. 2015, ApJ, 800, 50

Matsuura, M., Indebetouw, R., Woosley, S., et al. *ALMA spectral survey of Supernova 1987A - molecular inventory, chemistry, dynamics and explosive nucleosynthesis*. 2017, MNRAS, 469, 3347

McCray, R. *Supernova 1987A revisited*. 1993, ARA&A, 31, 175

McCray, R. *Supernova 1987A at Age 20*. 2007, AIPC, 937, 3

McCray, R., & Fransson, C. *The Remnant of Supernova 1987A*. 2016, ARA&A, 54, 19

Middelberg, E., Roy, A. L., Walker, R. C., & Falcke, H. *VLBI observations of weak sources using fast frequency switching*. 2005, A&A, 433, 897

Mignard, F., Klioner, S., Lindegren, L., et al. *Gaia Data Release 1. Reference frame and optical properties of ICRF sources*. 2016, A&A, 595, A5

Molina, S. N., Agudo, I., Gomez, J. L., et al. *Evidence of internal rotation and a helical magnetic field in the jet of the quasar NRAO 150*. 2014, A&A, 566, A26

Moór, A., Frey, S., Lambert, S. B., Titov, O. A., & Bakos, J. *On the Connection of the Apparent Proper Motion and the VLBI Structure of Compact Radio Sources*. 2011, AJ, 141, 178

Morris, T. & Podsiadlowski, P. *The Triple-Ring Nebula Around SN 1987A: Fingerprint of a Binary Merger*. 2007, Science, 315, 1103

Morris, T. & Podsiadlowski, P. *A binary merger model for the formation of the Supernova 1987A triple-ring nebula*. 2009, MNRAS, 399, 515

Ng, C.-Y., Zanardo, G., Potter, T. M., et al. *Evolution of the Radio Remnant of Supernova 1987A: Morphological Changes from Day 7000*. 2013, ApJ, 777, 131

Nisenson, P., Papaliolios, C., Karovska, M., Noyes, R. *Detection of a very bright source close to the LMC supernova SN 1987A*. 1987, ApJL, 320, L15

O'Sullivan, S. P., & Gabuzda, D. C. *Magnetic Field Strength and Spectral Distribution of Six Active Galactic Nuclei Jets*. 2009, MNRAS, 400, 26

Pacholczyk, A. G. *Radio astrophysics. Nonthermal processes in galactic and extragalactic sources*. 1970, Series of Books in Astronomy and Astrophysics (San Francisco, California, USA: W. H. Freemann and Company)

Panagia, N., Gilmozzi, R., Macchetto, F., Adorf, H.-M., & Kirshner, R. P. *Properties of the SN 1987A circumstellar ring and the distance to the Large Magellanic Cloud*. 1991, ApJ, 380, L23

Pérez-Torres, M. A., Marcaide, J. M., Guirado, J. C., et al. *Towards global phase-delay VLBI astrometry: observations of QSO 1150+812 and BL 1803+784*. 2000, A&A, 360, 161

Pérez-Torres, M. A., Marcaide, J. M., Guirado, J. C., & Ros, E. *Absolute kinematics of radio source components in the complete S5 polar cap sample II. First and second epoch maps at 15 GHz*. 2004, A&A, 428, 847

Perucho, M., Lobanov, A. P.; Martí, J.-M., & Hardee, P. E. *The role of Kelvin-Helmholtz instability in the internal structure of relativistic outflows. The case of the jet in 3C 273*. 2006, A&A, 456, 493

Petrov, L., & Kovalev, Y. Y. *On significance of VLBI/Gaia position offsets*. 2017, MNRAS, 467, L71

Pinto, P. A., Woosley, S. E., & Ensman, L. M. *SN 1987A - Out on the tail*. 1988, ApJL, 331, 101

Porcas, R. W. *Radio astrometry with chromatic AGN core positions*. 2009, A&A, 505, 1

Pushkarev, A. B., Kovalev, Y. Y., Lister, M. L., & Savolainen, T. *Jet opening angles and gamma-ray brightness of AGN*. 2009, A&A, 507, L33

Rank, D. M., Pinto, P. A., Woosley, S. E., Bregman, J. D., & Witteborn, F. C. *Nickel, argon and cobalt in the infrared spectrum of SN1987A - The core becomes visible*. 1988, Nature, 331, 505

Reid, M. J. & Honma, M. *Microarcsecond Radio Astrometry*. 2014, ARA&A, 52, 339

Rioja, M. J., & Porcas, R. W. *Multi-Frequency VLBA+Effelsberg Observations of 1038+528 A/B*. 1998, in ASP Conf. Ser. 144, IAU Coll. 164, Radio Emission from Galactic and Extragalactic Compact Sources, ed. J. A. Zensus, G. B. Taylor, & J. M. Wrobel (San Francisco, CA: ASP), 95

Rioja, M., Dodson, R., Porcas, R. W., et al. *Revisited "Cluster-Cluster" VLBI with future multi-beam low frequency radio interferometers*. 2009. Proc. 8th Int. e-VLBI Workshop, Madrid, Spain, June 22-26, PoS(EXPReS09)014

Rioja, M. & Dodson, R. *High-precision Astrometric Millimeter Very Long Baseline Interferometry Using a New Method for Atmospheric Calibration*. 2011, AJ, 141, 114

Rioja, M. J., Dodson, R., Jung, T., et al. *Verification of the Astrometric Performance of the Korean VLBI Network, Using Comparative SFPR Studies with the VLBA at 14/7 mm*. 2014, AJ, 148, 84

Rioja, M. J., Dodson, R., Jung, T., & Sohn, B. W. *The Power of Simultaneous Multifrequency Observations for mm-VLBI: Astrometry up to 130 GHz with the KVN*. 2015, AJ, 150, 202

Roche, P. F., Aitken, D. K., & Smith, C. H. *Silicon monoxide in Supernova 1987A*. 1991, MNRAS, 252, 39P

Ros, E., Marcaide, J. M., Guirado, J. C., et al. *High precision difference astrometry applied to the triplet of S5 radio sources B1803+784/Q1928+738/B2007+777*. 1999, A&A, 348, 381

Ros, E., Marcaide, J. M., Guirado, J. C., & Pérez-Torres, M. A. *Absolute kinematics of radio source components in the complete S5 polar cap sample. I. First and second epoch maps at 8.4 GHz*. 2001, A&A, 376, 1090

Ros, E., & Lobanov, A. P. *Opacity in the Jet of 3C 309.1*. 2001, in Behrend D., Ruis A., eds, Proc. 15th Workshop Meeting on European VLBI for Geodesy and Astrometry. Inst. d'Estudis Espacials Catalunya, Barcelona, p. 208

Ros, E. *High Precision Differential Astrometry*. 2005, Future Directions in High Resolution Astronomy, 340, 482

Rosolowsky, E., & Leroy, A. *Bias-free Measurement of Giant Molecular Cloud Properties*. 2006, PASP, 118, 590

Sarangi, A., & Cherchneff, I. *The Chemically Controlled Synthesis of Dust in Type II-P Supernovae*. 2013, ApJ, 776, 107

Savolainen, T., Wiik, K., Valtaoja, E., et al. *An Extremely Curved Relativistic Jet in PKS 2136+141*. 2006, ApJ, 647, 172

Savolainen, T., Wiik, K., Valtaoja, E., & Tornikoski, M. *Magnetic Field Structure in the Parsec Scale Jet of 3C 273 from Multifrequency VLBA Observations*. 2008, Extragalactic Jets: Theory and Observation from Radio to Gamma Ray, PASP, 386, 451

Schuh, H., & Behrend, D. *VLBI: A fascinating technique for geodesy and astrometry.* 2012, J Geodyn 61, DOI 10.1016/j.jog.2012.07.007, 68-80

Schwab, F. R., & Cotton, W. D. *Global fringe search techniques for VLBI*. 1983, AJ, 88, 688

Shapiro, I. I., Wittels, J. J., Counselman, C. C., et al. *Submilliarcsecond astrometry via VLBI. I - Relative position of the radio sources 3C 345 and NRAO 512*. 1979, AJ, 84, 1459

Shigeyama, T., & Nomoto, K. *Theoretical light curve of SN 1987A and mixing of hydrogen and nickel in the ejecta*. 1990, ApJ, 360, 242

Sluder, A., Milosavljevic, M., & Montgomery, M. H. *Molecular nucleation theory of dust formation in core-collapse supernovae applied to SN 1987A*. 2016, arXiv:1612.09013

Smartt, S. J. *Progenitors of core-collapse supernovae*. 2009, ARA&A, 47, 63

Sokolovsky, K. V., Kovalev, Y. Y., Pushkarev, A. B., & Lobanov, A. P. *A VLBA survey of the core shift effect in AGN jets. I. Evidence of dominating synchrotron opacity*. 2011, A&A, 532, A38

Sonneborn, G., Fransson, C., Lundqvist, P., et al. *The Evolution of Ultraviolet Emission Lines From Circumstellar Material Surrounding SN 1987A*. 1997, ApJ, 477, 848

Sonneborn, G., Pun, C. S. J., Kimble, R. A., et al. *Spatially Resolved STIS Spectroscopy of SN 1987A: Evidence for Shock Interaction with Circumstellar Gas*. 1998, ApJL, 492, L139

Spyromilio, J., Meikle, W. P. S., Learner, R. C. M., & Allen, D. A. *Carbon monoxide in supernova 1987A*. 1988, Nature, 334, 327

Spyromilio, J., Meikle, W. P. S., & Allen, D. A. *Spectral line profiles of iron and nickel in supernova 1987A - Evidence for a fragmented nickel bubble*. 1990, MNRAS, 242, 669

Spyromilio, J., & Graham, J. R. *Supernova 1987 A - A cold, dusty and rusty supernova*. 1992, MNRAS, 255, 671

Spyromilio, J., Leibundgut, B., Fransson, C., et al. *Supernova 1987A at 30*. 2017, The Messenger, 167, 26

Thompson, A. R., Moran, J. M. & Swenson, G. W. *Interferometry and Synthesis in Radio Astronomy*. 2001, 2 ed., Wiley, New York

Titov, O., Lambert, S. B., & Gontier, A.-M. *VLBI measurement of the secular aberration drift*. 2011, A&A, 529, A91

Türler, M., Courvoisier, T. J.-L., & Paltani, S. *Modelling the submillimetre-to-radio flaring behaviour of 3C 273*. 1999, A&A, 349, 45

Tziamtzis, A., Lundqvist, P., Gröningsson, P., & Nasoudi-Shoar, S. *The outer rings of SN 1987A*. 2011, A&A, 527, A35

Urry, M. C. & Padovani, P. *Unified Schemes for Radio-Loud Active Galactic Nuclei*. 1995, PASP, 107, 803

Utrobin, V. P., Wongwathanarat, A., Janka, H.-Th., & Müller, E. *Supernova 1987A: neutrino-driven explosions in three dimensions and light curves*. 2015, A&A, 581, A40

Williams, J. P., de Geus, E. J., & Blitz, L. *Determining structure in molecular clouds*. 1994, ApJ, 428, 693

Wilson, J.R. *Supernovae and Post-Collapse Behavior*. 1985, in: J.M. Centrella, J.M. LeBlanc & R.L. Bowers (eds.), Numerical Astrophysics (Boston: Jones and Bartlett Publ.), p. 422

Wilson, T., Rohlfs, K., & Hüttemeister, S. *Tools of Radio Astronomy*. 2009, 5 ed., Springer, Berlin

Wongwathanarat, A., Müller, E., & Janka, H.-T. *Three-dimensional simulations of core-collapse supernovae: from shock revival to shock breakout*. 2015, A&A, 577, A48

Woosley, S. E., Pinto, P. A., & Ensman, L. *Supernova 1987A - Six weeks later*. 1988, ApJ, 324, 466

Woosley, S. E., Hartmann, D., Pinto, P. A. *Hard emission at late times from SN 1987A*. 1989, ApJ, 346, 395

Woosley, S. E., & Weaver, T. A. *The Evolution and Explosion of Massive Stars. II. Explosive Hydrodynamics and Nucleosynthesis*. 1995, ApJS, 101, 181

Zanardo, G., Staveley-Smith, L., Ball, L., et al. *Multifrequency Radio Measurements of Supernova 1987A Over 22 Years*. 2010, ApJ, 710, 1515

Zanardo, G., Staveley-Smith, L., Indebetouw, R., et al. *Spectral and Morphological Analysis of the Remnant of Supernova 1987A with ALMA and ATCA*. 2014, ApJ, 796, 82

Zanardo, G. *Radio evolution of the remnant of Supernova 1987A*. 2014, Ph.D. Thesis, ICRAR